

**Narrowband Ultraviolet B emission from gadolinium and praseodymium
co-activated calcium phosphate phosphors for phototherapy lamps.**

By

Puseletso Pricilla Mokoena

(B. Sc Hons)

A thesis submitted in fulfillment of the requirements for the degree

MAGISTER SCIENTIAE

in the

Faculty of Natural and Agricultural Sciences

Department of Physics

at the

University of the Free State

South Africa

Promoter: Prof. O.M. Ntwaeaborwa

Co-Promoter: Prof. H.C. Swart

January 2014

**“A dream doesn’t become reality through magic; it takes sweat,
determination and hard work”
- Colin Powell**

Acknowledgements

- I would firstly like to express my outermost gratitude to the Man who made this study possible, by giving me strength and wisdom to pursue even in most difficult times. I thank you God Almighty for carrying me through, I could not have made it on my own.
- I would also like to express my sincere gratitude to my promoter *Prof. O.M. Ntwaeaborwa*, for always encouraging, supporting and guiding me throughout the study. The study could not have been a success without him. Thank you a lot.
- Special thanks to my co-promoter *Prof. H.C. Swart*, for his support, guidance and immeasurable help and valuable inputs.
- I would like to express my sincere gratitude to both *Dr I.M. Nagpure* and *Dr M. Gohain* for introducing me to various synthesis methods.
- I thank *Prof. M.L. Chithambo* and his students at Rhodes University for welcoming me at his lab and introducing me to thermoluminescence (TL) technique.
- Many thanks to *Prof. J.H. Neethling* for assisting with High Resolution Transmission Electron Microscopy (HRTEM) measurements.
- I express my thanks to the technical staff (*Dr Liza Coetsee and Mrs Mart-Mari Duvenhage*) advices, support and guidance during surface characterization for nanomaterials.
- I would like to extend my big thanks to the technical staff of Centre of Microscopy (*Prof. P.W.J. Van Wyk and Ms H. Grobler*) for their guidance during Scanning Electron Microscopy (SEM) measurements.

- I thank *Dr R.E. Kroon and Dr V Kumar*, for helping out in analyzing some HRTEM and TL data.
- I express my deepest appreciation to my fellow researchers (*Mr M.J. Madito, Dr P.S. Mbule, Ms M.A. Moleme, Mr L.L. Noto, Dr S.K.K. Shaat, Ms M.A. Tshabalala, Mr K.G. Tshabalala, Mr M.Y.A. Yagoub, Mr A. Yousif*) for their constructive discussions and assistance in this research, and the entire staff in the Physics department.
- I am grateful for the financial support from South African National Research Foundation (NRF), South African Research Chairs Initiative and Department of Science and Technology, and the University of the Free State.
- My extended gratitude to my family, my father (*Mohloli Samuel Mokoena*), my mother (*Mohanuoa Maria Mokoena*), my younger brother (*Muso Joshua Mokoena*), for their support, understanding, prayers, encouragement and always being there for me when I needed them the most, and the rest of the family.

Abstract

Different phases of calcium phosphates co-doped with gadolinium and praseodymium were prepared by co-precipitation, urea combustion, citrate-gel combustion and microwave-assisted methods.

$\text{Ca}_5(\text{PO}_4)_3\text{OH}:\text{Gd}^{3+},\text{Pr}^{3+}$ phosphors were prepared by the co-precipitation and citrate-gel methods, and were characterized by X-ray diffraction (XRD), X-ray photoelectron spectroscopy (XPS), Scanning electron microscopy (SEM), High resolution transmission electron microscopy (HRTEM), Energy dispersive x-ray spectrometer (EDS) and photoluminescence (PL) spectroscopy. The XRD pattern was consistent with the hexagonal phase of $\text{Ca}_5(\text{PO}_4)_3\text{OH}$ referenced in JCPDS Card Number 73-0293. The XPS data indicated that Ca^{2+} occupied two different lattice sites referred to as Ca1 and Ca2. The P^{5+} is surrounded by O^{2-} ions in the tetrahedral arrangements. Each tetrahedron contains oxygen atoms designated as O1, O2, and O3. The particle morphology was analyzed using SEM and HRTEM. SEM shows that the powder was composed of an agglomeration of irregular particles. HRTEM revealed faceted edges forming a hexagonal shape. PL data exhibited a narrowband emission located at 313 nm, which is associated with the ${}^6\text{P}_{7/2} \rightarrow {}^8\text{S}_{7/2}$ transition of the Gd^{3+} ion. This emission is classified as ultraviolet B (UVB) and it is suitable for use in phototherapy lamps to treat various skin diseases. The PL intensity of the 313 nm emission was enhanced considerably by Pr^{3+} co-doping. The crystallographic structure of $\text{Ca}_5(\text{PO}_4)_3\text{OH}:\text{Gd}^{3+},\text{Pr}^{3+}$ and possible mechanism of energy transfer from Pr^{3+} to Gd^{3+} are discussed.

$\text{Ca}_5(\text{PO}_4)_3\text{OH}:\text{Gd}^{3+},\text{Pr}^{3+}$ phosphor exhibited a single thermoluminescence peak between 339-363 K. The peak shifted towards high temperature with an increase in dose. The shift shows that the trap system is more complicated than a single trap obeying first order kinetics. The calculated activation energy (E_A) was found to be 0.91 eV when the using initial rise method. The activation energy values were further calculated using the peak shape method. The calculated activation energies for ω , τ and δ , were 0.75, 1.03, and 0.42 eV respectively. There was a peak shifting to higher temperatures with an increase in heating rate which is attributed to recombination that is slowing down due to electron-phonon interactions. The peak intensity increased with an increase in heating rate from 0.6 to 2.0 $^\circ\text{C}\cdot\text{s}^{-1}$ and started to decrease from 3.0 to 5.0 $^\circ\text{C}\cdot\text{s}^{-1}$, the decrease maybe due to

thermal quenching as the peak shift to higher temperatures. The calculated activation energy by heating rate method was found to be 0.60 eV. This value is comparable to other calculated values of activation energies by various methods mentioned above.

$\text{Ca}_3(\text{PO}_4)_2:\text{Gd}^{3+},\text{Pr}^{3+}$ phosphors with different concentrations of Gd^{3+} and Pr^{3+} were successfully prepared by urea combustion process using metal nitrates as precursors and urea as fuel and also by the microwave assisted method. XRD exhibited a rhombohedral phase of $\text{Ca}_3(\text{PO}_4)_2$ referenced in JCPDS Card No. 70-2065. The PL excitation spectra of $\text{Ca}_3(\text{PO}_4)_2:\text{Gd}^{3+}$ and $\text{Ca}_3(\text{PO}_4)_2:\text{Pr}^{3+}$ exhibited peaks at 220-280 nm and 300-490 nm associated with the *f-f* transitions of Gd^{3+} and Pr^{3+} respectively. The UVB emission resulting from the ${}^6\text{P}_{7/2}\rightarrow{}^8\text{S}_{7/2}$ transition of Gd^{3+} was observed at 313 nm when the $\text{Ca}_3(\text{PO}_4)_2:\text{Gd}^{3+}$ phosphor was excited at a wavelength of 274 nm using a monochromatized xenon lamp. Upon Pr^{3+} co-doping, the excitation peaks due to Gd^{3+} and Pr^{3+} *f-f* transitions were suppressed and an intense broad excitation peak ascribed to the $4f\rightarrow 4f5d$ transitions of Pr^{3+} was observed at 227 nm. The peak intensity of the UVB emission at 313 nm was shown to improve considerably when the Gd^{3+} and Pr^{3+} co-doped systems were excited at the wavelength of 227 nm suggesting that the Pr^{3+} is a good sensitizer of the 313 nm narrow line UVB emission from Gd^{3+} .

Keywords

Calcium Phosphate, Biocompatible material, Phototherapy Lamps, UV Radiation, Energy Transfer

List of Acronyms

XRD	X-ray Diffraction
XPS	X-ray Photoelectron Spectroscopy
SEM	Scanning Electron Microscopy
HRTEM	High Resolution Transmission Electron Microscopy
EDS	Energy Dispersive x-ray Spectrometer
PL	Photoluminescence
TL	Thermoluminescence

UVR	Ultra-Violet Radiation
PLE	Photoluminescence Excitation
REE	Rare-Earth Elements
Gd ³⁺	Gadolinium
Pr ³⁺	Praseodymium

Table of Contents

Title and Affiliation	i
Quote	ii
Acknowledgements	iii
Abstract.....	v
Keywords	vi
List of Acronyms	vi
Chapter 1: Introduction	1
1.1 Overview	1
1.2 Statement of Problem.....	2
1.3 Research Aim.....	2
1.4 Research objectives.....	2
1.5 Thesis layout	3
References.....	4
Chapter 2: Literature Review	5
2.1 Introduction.....	5
2.2 Background of Phosphors	5
2.3 Calcium phosphates	6
2.4 Gadolinium	8
2.4.1. Applications of Gd^{3+}	9
2.4.2. Luminescent properties of Gd^{3+} ion	9
2.5 Praseodymium.....	10
2.5.1 Applications of Pr^{3+}	11
2.5.2 Luminescent properties	11
2.6 Luminescence	12
2.6.1 Photoluminescence.....	13
2.6.2 Thermoluminescence	14

2.7 Quenching of Luminescence.....	15
2.8 Energy Transfer process in Rare Earth Phosphors.....	15
2.9 Application of phosphors.....	17
2.9.1 Phototherapy Lamps	17
2.9.2 Applications of phosphor in the phototherapy lamp.....	20
References.....	22
Chapter 3: Research Techniques.....	25
3.1 Introduction.....	25
3.2 X-ray Diffraction.....	25
3.3 X-ray Photoelectron Spectroscopy.....	27
3.4 Electron Microscope	29
3.4.1 Scanning Electron Microscope	30
3.4.2 Transmission Electron Microscopy	32
3.5 Ultraviolet-visible spectrophotometer.....	34
3.6 Luminescence spectroscopy.....	37
3.6.1 Photoluminescence spectroscopy.....	37
3.6.2 Thermoluminescence spectroscopy	39
3.7 Time-of-Flight Secondary Ion Mass Spectrometry.....	40
References.....	43
Chapter 4: Synthesis Techniques	45
4.1 Introduction.....	45
4.2 Co-precipitation method	45
4.3 Combustion method.....	48
4.4 Microwave assisted synthesis method	52
References.....	55
Chapter 5: Luminescent properties of $\text{Ca}_5(\text{PO}_4)_3:\text{Gd}^{3+},\text{Pr}^{3+}$ phosphor powder prepared by Co-precipitation method	56
5.1 Introduction.....	56
5.2 Experimental	56

5.3 Results and Discussion	57
5.4 Conclusion	73
References.....	74
Chapter 6: Thermoluminescence properties of $\text{Ca}_5(\text{PO}_4)_3\text{OH}:\text{Gd}^{3+},\text{Pr}^{3+}$ phosphor prepared via co-precipitation method.....	76
6.1 Introduction.....	76
6.2 Kinetic Analysis.....	76
6.3 Experimental	78
6.4 Results and Discussion	78
6.4.1 Initial rise method	81
6.4.2 Peak shape method.....	81
6.4.3 Heating rate method.....	83
6.4.4 $T_m - T_{\text{stop}}$ method	85
6.5 Conclusion	88
References.....	89
Chapter 7: TOF SIMS analysis and enhanced UVB photoluminescence by energy transfer from Pr^{3+} to Gd^{3+} in $\text{Ca}_3(\text{PO}_4)_2:\text{Gd}^{3+},\text{Pr}^{3+}$ phosphor prepared by urea assisted combustion.....	90
7.1 Introduction.....	90
7.2 Experimental	91
7.3 Results and Discussion	92
7.4 Conclusion	104
References.....	105
Chapter 8: Luminescent properties of $\text{Ca}_5(\text{PO}_4)_3\text{OH}:\text{Gd}^{3+},\text{Pr}^{3+}$ phosphor powder prepared by citrate-gel combustion	107
8.1 Introduction.....	107
8.2 Experimental	107
8.3 Results and Discussion	108
8.4 Conclusion	112

References.....	113
Chapter 9: Luminescent properties, particle morphology and chemical composition of $\text{Ca}_3(\text{PO}_4)_2:\text{Gd}^{3+},\text{Pr}^{3+}$ powder phosphor prepared by microwave assisted synthesis method.....	114
9.1 Introduction.....	114
9.2 Experimental.....	114
9.3 Results and Discussion	115
9.4 Conclusion	121
References.....	122
Chapter 10: Summary and Conclusion.....	123
Future Work.....	125

List of figures

Figure 2.1 Crystalline structure of hydroxyapatite	7
Figure 2.2 β - $\text{Ca}_3(\text{PO}_4)_2$ unit cell plane	8
Figure 2.3 Energy level scheme in the range 0 – 80 000 cm^{-1} of Gd^{3+} ion.....	10
Figure 2.4 The energy level diagram of Pr^{3+} ion	12
Figure 2.5 Photoluminescence process	13
Figure 2.6 The probability of energy transfer by critical distance (R_c)	16
Figure 2.7 Absorption and fluorescence spectra of an ideal donor-acceptor pair	16
Figure 2.8 The energy transfer process at parallel energy level	17
Figure 2.9 Shows the ultraviolet portion of the electromagnetic spectrum.	18
Figure 2.10 (a) Shows the spectrum the erythema and Broadband UVB, (b) Narrowband 311 nm Source Spectra	19
Figure 2.11 Fluorescent lamp showing basic elements in the lamp.	20
Figure 2.12 Fluorescent lamp showing basic elements in the lamp and treated skin disorder.	21
Figure 3.1 Schematic of the reflection of x-rays by crystal planes.....	26
Figure 3.2 D8 Advanced AXS GmbH X-ray diffractometer.....	27
Figure 3.3 Schematic diagram of the XPS technique	28
Figure 3.4 PHI 5000 Versa Probe II Scanning XPS Microprobe	29
Figure 3.5 Schematic presentation of scanning electron microscopy	31
Figure 3.6 Shimadzu Super Scan SSX550 model SEM.	32
Figure 3.7 Schematic outline of TEM.....	33
Figure 3.8 JEOL JEM-ARM200F.....	34
Figure 3.9 Schematic of the UV-Visible spectrophotometer.....	35
Figure 3.10 Perkin Elmer Lambda 950 UV-VIS spectrometer.....	37
Figure 3.11 Outline of photoluminescence spectroscopy.	38
Figure 3.12 Varian Cary-Eclipse fluorescent spectroscopy.....	38
Figure 3.13 The outline of electron trapping.	39
Figure 3.14 Riso TL/OSL reader model DA-20	40
Figure 3.15 Schematic diagram of TOF-SIMS instrument.....	41
Figure 3.16 ION-TOF.SIMS 5.....	42
Figure 4.1 Flow-chart of co-precipitation method.....	46
Figure 4.2 Preparation method of $\text{Ca}_5(\text{PO}_4)_3\text{OH}:\text{Gd}^{3+},\text{Pr}^{3+}$ nanophosphor by co-precipitation method.....	47
Figure 4.3 Flow-chart of $\text{Ca}_3(\text{PO}_4)_2:\text{Gd}^{3+},\text{Pr}^{3+}$ prepared by urea combustion method.	49
Figure 4.4 Flow-chart of $\text{Ca}_5(\text{PO}_4)_3\text{OH}:\text{Gd}^{3+},\text{Pr}^{3+}$ citrate-gel combustion method.	50
Figure 4.5 snapshots of phosphor powders prepared by urea and citrate-gel combustion methods.	51
Figure 4.6 Flow-chart of $\text{Ca}_3(\text{PO}_4)_2:\text{Gd}^{3+},\text{Pr}^{3+}$ phosphor prepared by microwave-assisted method.....	53
Figure 4.7 snapshots of preparation of $\text{Ca}_3(\text{PO}_4)_2:\text{Gd}^{3+},\text{Pr}^{3+}$ by microwave-assisted method.	54
Figure 5.1 (a) XRD patterns of $\text{Ca}_5(\text{PO}_4)_3\text{OH}$ powder and matching JCPDS Card No. 73-0293, and (b) XRD pattern of $\text{Ca}_5(\text{PO}_4)_3\text{OH}:\text{Gd}^{3+},\text{Pr}^{3+}$ calcined at different temperatures.....	58

Figure 5.1 (c) FWHM of (211) plane versus different annealing temperatures and (d) Crystal structure of $\text{Ca}_5(\text{PO}_4)_3\text{OH}$.	59
Figure 5.2 XPS survey spectrum of $\text{Ca}_5(\text{PO}_4)_3\text{OH}:\text{Gd}^{3+},\text{Pr}^{3+}$ phosphor powder	62
Figure 5.3 (a-e) Deconvoluted Ca (2p), P (2p), O (1s), Gd (3d) and Pr (3d) peaks of $\text{Ca}_5(\text{PO}_4)_3\text{OH}:\text{Gd}^{3+},\text{Pr}^{3+}$ powder phosphor annealed at 900 °C in air.	64
Figure 5.4 (a) SEM images, (b) EDS spectrum, (c) HRTEM images, (d) lattice fringes and (e) selected area electron diffraction pattern of the HRTEM image of $\text{Ca}_5(\text{PO}_4)_3\text{OH}:\text{Gd}^{3+},\text{Pr}^{3+}$ phosphor powders.	66
Figure 5.5 (a-c) Positive TOF-SIMS spectra of $\text{Ca}_5(\text{PO}_4)_3\text{OH}:\text{Gd}^{3+},\text{Pr}^{3+}$ showing Ca^{2+} , Gd^{3+} , and Pr^{3+} peaks.	67
Figure 5.5 (d-e) Negative TOF-SIMS spectra of $\text{Ca}_5(\text{PO}_4)_3\text{OH}:\text{Gd}^{3+},\text{Pr}^{3+}$ showing P^{3-} and O^{2-} peaks.	67
Figure 5.6 (a) TOF-SIMS chemical images of $\text{Ca}_5(\text{PO}_4)_3\text{OH}:\text{Gd}^{3+},\text{Pr}^{3+}$ phosphor powder for an area of $100\ \mu\text{m} \times 100\ \mu\text{m}$ for positive ions.	68
Figure 5.6 (b) TOF-SIMS chemical images of $\text{Ca}_5(\text{PO}_4)_3\text{OH}:\text{Gd}^{3+},\text{Pr}^{3+}$ phosphor powder for an area of $100\ \mu\text{m} \times 100\ \mu\text{m}$ for negative ions.	68
Figure 5.7 (a) Optical absorption spectra of $\text{Ca}_5(\text{PO}_4)_3\text{OH}:\text{Gd}^{3+},\text{Pr}^{3+}$ phosphor powders.	69
Figure 5.7 (b) $(\alpha h\nu)^2$ vs photon energy ($h\nu$) plot of $\text{Ca}_5(\text{PO}_4)_3\text{OH}:\text{Gd}^{3+},\text{Pr}^{3+}$ phosphor powders.	70
Figure 5.8 PL excitation and emission spectra of (a) $\text{Ca}_5(\text{PO}_4)_3\text{OH}:\text{Gd}^{3+}$, (b) $\text{Ca}_5(\text{PO}_4)_3\text{OH}:\text{Pr}^{3+}$, and (c) $\text{Ca}_5(\text{PO}_4)_3\text{OH}:\text{Gd}^{3+},\text{Pr}^{3+}$ phosphor powders.	72
Figure 6.1 Thermoluminescence glow curve of $\text{Ca}_5(\text{PO}_4)_3\text{OH}:\text{Gd}^{3+},\text{Pr}^{3+}$ and background signal.	79
Figure 6.2 Thermoluminescence glow-curve of $\text{Ca}_5(\text{PO}_4)_3\text{OH}:\text{Gd}^{3+},\text{Pr}^{3+}$ phosphor at different beta irradiation from 6 – 186 Gy.	80
Figure 6.3 Deconvolution TL glow-curve showing the experimental data (black broken line) and the fitted (pink line) glow curve of $\text{Ca}_5(\text{PO}_4)_3\text{OH}:\text{Gd}^{3+},\text{Pr}^{3+}$ phosphor.	80
Figure 6.4 Activation energy versus dose spectrum of $\text{Ca}_5(\text{PO}_4)_3\text{OH}:\text{Gd}^{3+},\text{Pr}^{3+}$ phosphor.	81
Figure 6.5 Plot of the Peak shape method used for calculation of activation energy.	82
Figure 6.6 Thermoluminescence glow curve of $\text{Ca}_5(\text{PO}_4)_3\text{OH}:\text{Gd}^{3+},\text{Pr}^{3+}$ phosphor using variable heating rate method.	84
Figure 6.7 Shows a plot of $\ln(T_m^2/\beta)$ versus $1/T_m$.	84
Figure 6.8 $T_m - T_{\text{stop}}$ plot of $\text{Ca}_5(\text{PO}_4)_3\text{OH}:\text{Gd}^{3+},\text{Pr}^{3+}$ phosphor.	85
Figure 7.1 (a) XRD patterns $\text{Ca}_3(\text{PO}_4)_2:\text{Gd}^{3+},\text{Pr}^{3+}$ annealed at 1000 °C using various urea masses ranging from 0.5 – 10g.	93
Figure 7.1 (b) Line broadening of $\text{Ca}_3(\text{PO}_4)_2:\text{Gd}^{3+},\text{Pr}^{3+}$ at various urea masses.	93
Figure 7.2 The $\text{Ca}_3(\text{PO}_4)_2$ unit cell described with a polyhedral (ICSD-99358)	94
Figure 7.3 SEM images of (a) $\text{Ca}_3(\text{PO}_4)_2$, (b) $\text{Ca}_3(\text{PO}_4)_2:\text{Gd}^{3+}$ and (c) $\text{Ca}_3(\text{PO}_4)_2:\text{Gd}^{3+},\text{Pr}^{3+}$ phosphor powder obtained after annealing at 1000 °C in air.	95
Figure 7.4 (a) Positive TOF-SIMS spectra of $\text{Ca}_3(\text{PO}_4)_2:\text{Gd}^{3+},\text{Pr}^{3+}$ phosphor powder.	96
Figure 7.4 (b) negative TOF-SIMS spectra of $\text{Ca}_3(\text{PO}_4)_2:\text{Gd}^{3+},\text{Pr}^{3+}$ phosphor powder.	97
Figure 7.5 (a) TOF-SIMS chemical images of $\text{Ca}_3(\text{PO}_4)_2:\text{Gd}^{3+},\text{Pr}^{3+}$ phosphor powder for positive ion mode.	97

Figure 7.5 (b) TOF-SIMS chemical images of $\text{Ca}_3(\text{PO}_4)_2:\text{Gd}^{3+},\text{Pr}^{3+}$ phosphor powder for negative ion mode.	98
Figure 7.6 (a) Optical absorption spectra of $\text{Ca}_3(\text{PO}_4)_2:\text{Gd}^{3+},\text{Pr}^{3+}$	99
Figure 7.6 (b) $(\alpha h\nu)^2$ vs photon energy ($h\nu$) plot of $\text{Ca}_3(\text{PO}_4)_2:\text{Gd}^{3+},\text{Pr}^{3+}$	99
Figure 7.7 PL spectra of $\text{Ca}_3(\text{PO}_4)_2:\text{Gd}^{3+}$ (a) excitation ($\lambda_{\text{emi}} = 313$ nm) and (b) emission ($\lambda_{\text{exc}} = 274$ nm).....	100
Figure 7.8 PL spectra of $\text{Ca}_3(\text{PO}_4)_2:\text{Pr}^{3+}$ (a) excitation ($\lambda_{\text{emi}} = 603$ nm) and (b) emission ($\lambda_{\text{exc}} = 444$ nm).	101
Figure 7.9 PL(a) excitation and emission spectra of $\text{Ca}_3(\text{PO}_4)_2:\text{Gd}^{3+},\text{Pr}^{3+}$ powder phosphor, (b) comparison between PL excitation and emission spectra of Gd^{3+} single doped and $\text{Gd}^{3+}-\text{Pr}^{3+}$ co-doped $\text{Ca}_3(\text{PO}_4)_2$ powder phosphors (c) simplified energy transfer mechanism for $\text{Pr}^{3+}-\text{Gd}^{3+}$ system.	103
Figure 8.1 XRD patterns of $\text{Ca}_5(\text{PO}_4)_3\text{OH}$ annealed at 850°C in air furnace.	109
Figure 8.2 (a-b) SEM images and (c) EDS spectrum of $\text{Ca}_5(\text{PO}_4)_3\text{OH}:\text{Gd}^{3+},\text{Pr}^{3+}$ phosphor powder calcined at 850°C for 2 hours.	110
Figure 8.3 PL spectra of $\text{Ca}_5(\text{PO}_4)_3\text{OH}:\text{Gd}^{3+}$ phosphor annealed at 850°C in air.	111
Figure 8.4 PL spectra of $\text{Ca}_5(\text{PO}_4)_3\text{OH}:\text{Gd}^{3+},\text{Pr}^{3+}$ phosphor powders annealed at 850°C in air.	112
Figure 9.1 XRD patterns of $\text{Ca}_3(\text{PO}_4)_2$ annealed at 1000°C in air.	116
Figure 9.2 (a-b) High Resolution SEM images of $\text{Ca}_3(\text{PO}_4)_2:\text{Gd}^{3+},\text{Pr}^{3+}$ powder phosphor... ..	117
Figure 9.2 (c-d) shows the morphology of $\text{Ca}_3(\text{PO}_4)_2:\text{Gd}^{3+},\text{Pr}^{3+}$ powder measured by using objective lens called gentle beam.	117
Figure 9.2 (e-f) EDS spectra of $\text{Ca}_3(\text{PO}_4)_2:\text{Gd}^{3+},\text{Pr}^{3+}$ powder phosphors.....	118
Figure 9.3 PL spectra (i) excitation ($\lambda_{\text{emi}} = 313$ nm) and (ii) emission ($\lambda_{\text{exc}} = 274$ nm) of $\text{Ca}_3(\text{PO}_4)_2:\text{Gd}^{3+}$ powder phosphor.....	119
Figure 9.4 PL (a) (i) excitation and (ii) emission spectra of $\text{Ca}_3(\text{PO}_4)_2:\text{Gd}^{3+},\text{Pr}^{3+}$ powder phosphor (b) Comparison between emission intensity of $\text{Ca}_3(\text{PO}_4)_2:\text{Gd}^{3+}$ and $\text{Ca}_3(\text{PO}_4)_2:\text{Gd}^{3+},\text{Pr}^{3+}$ system.	120

Chapter 1: Introduction

1.1 Overview

Skin diseases have become most critical and life threatening, where more than 125 million people are diagnosed annually, and others die every year due to these diseases [1]. They can develop at any age. Researchers who studied medical records have found that people in their 40s who suffer from skin diseases are more than twice likely to suffer a heart attack [2]. There are different sources that can be used to treat these diseases such as direct sunlight and ultraviolet (UV) phototherapy lamps. Exposure to sunlight is a simple way, but prolonged exposure to sunlight can result in sunburn that can worsen the symptoms. As a result, phototherapy lamps have been developed, tested and proven in close cooperation with universities and clinics around the world to be the most effective and safer than exposure to sunlight for treatment of skin diseases such as psoriasis, vitiligo, eczema, atopic dermatitis, acne vulgaris and mycosis fungoides. The lamp uses the artificial ultraviolet radiation for treating the condition.

So far phosphates are of great interest in the field of biomedical treatment. They are known to be well stable than oxides and fluorides. They can also be used as hosts for rare earth ions to prepare phosphors used in different types of phototherapy lamps due to the fact that they are biocompatible and can therefore directly bond with living tissues [3]. For examples, gadolinium (Gd^{3+}) is used as a dopant on the phosphate system because it emits narrowband ultraviolet B (UVB) radiation needed to treat skin diseases. However, the problem is that the intensity of this emission is very low and this can affect the general performance and the life span of the UV phototherapy lamps. UVB emission of Gd^{3+} can be improved by co-doping with other rare earth ions such as praseodymium (Pr^{3+}), cerium (Ce^{3+}), terbium (Tb^{3+}), and europium (Eu^{3+}) that can absorb excitation in the high energy region of the electromagnetic spectrum and transfer it to Gd^{3+} by a down-conversion process.

1.2 Statement of Problem

Every year more than 2 million people die from various skin diseases due to lack of therapy or remedies that can be used for treatment of these diseases. The search for new approaches, enhancement of the existing methods and development of new remedies for treatment is extremely crucial. One way of addressing this problem is to improve the efficiency of luminescent materials or phosphors that are used in phototherapy lamps as sources of UV light. In nanoscale, phosphors have been reported to be more efficient than in micron scale due to reduced scattering of light by smaller particles. Therefore this study undertakes to prepare high efficiency nanoparticles phosphors or nanophosphors that can be used in phototherapy lamps. In addition the emission efficiency of the nanophosphors will be improved by co-doping with rare-earth ions that will serve as sensitizers. The UVB emission from Gd^{3+} at 311 nm will be improved by co-doping with different concentration of Pr^{3+} and the energy transfer from Pr^{3+} to Gd^{3+} will be evaluated. The improved UVB emission at 311 nm by energy transfer will in turn improve the efficiency and the life time of the phototherapy lamps.

1.3 Research Aim

The aim of the study is to investigate the luminescent properties of calcium phosphate co-doped with gadolinium and praseodymium for application in phototherapy lamps.

1.4 Research objectives

- To synthesize co-doped calcium phosphate with Gd^{3+} and Pr^{3+} using different synthesizing methods.
- To investigate luminescent properties of rare earth ions (Gd^{3+} and Pr^{3+}) activated calcium phosphate phosphor.
- Optimization of synthesis conditions and composition of nanophosphor to obtain the samples providing the highest luminescence intensity.

- To investigate the effects of annealing temperature on the luminescence intensity of the nanophosphors.
- To investigate the energy transfer from Pr^{3+} to Gd^{3+} in calcium phosphate.

1.5 Thesis layout

Chapter 2: Presents the literature review information on calcium phosphate powder phosphors, trivalent rare earth ions, and luminescence processes. Detailed information on the energy transfer mainly in rare earth activated phosphors.

Chapter 3: Presents a summary of experimental techniques that were used in this study.

Chapter 4: Gives a brief description of synthesis methods used during the study.

Chapter 5: This chapter presents luminescent properties of $\text{Ca}_5(\text{PO}_4)_3\text{OH}:\text{Gd}^{3+},\text{Pr}^{3+}$ phosphor prepared by co-precipitation method.

Chapter 6: This chapter presents the thermoluminescence properties of $\text{Ca}_5(\text{PO}_4)_3\text{OH}:\text{Gd}^{3+},\text{Pr}^{3+}$ phosphor prepared via co-precipitation method.

Chapter 7: This chapter presents the luminescent properties of $\text{Ca}_3(\text{PO}_4)_2:\text{Gd}^{3+},\text{Pr}^{3+}$ phosphor powder prepared by urea combustion.

Chapter 8: This chapter presents the luminescent properties of $\text{Ca}_5(\text{PO}_4)_3\text{OH}:\text{Gd}^{3+},\text{Pr}^{3+}$ phosphor powder prepared by citrate-gel combustion.

Chapter 9: The effect of Pr^{3+} sensitizer on luminescent properties of $\text{Ca}_3(\text{PO}_4)_2:\text{Gd}^{3+}$ powder phosphor prepared by microwave assisted synthesis method.

Chapter 10: A summary of the thesis, concluding remarks and suggestion for possible future studies are presented.

References

- [1] <http://www.psoriasis.org/page.aspx?pid=1336> [accessed December 2013]
- [2] <http://www.aad.org/media-resources/stats-and-facts> [accessed December 2013]
- [3] B. Pavan, D. Ceresoli, M.M.J. Tecklenburg, M. Fornari, *Solid State Nucl. Magn. Reson.*, 2012, **45-46**, 59-65

Chapter 2: Literature Review

2.1 Introduction

This chapter presents a brief background of phosphors, in particular calcium phosphate phosphors, luminescence processes, energy transfer, and application of phosphors.

2.2 Background of Phosphors

Phosphors are chemical materials that emit light when excited with high energy such as electrons or photons. They are composed of either one chemical compound referred to as a host, and one or more activators mostly rare earth ions or alkali earth metal ions, in amounts from parts per million to a few mole percent. Either the chemical compound or the combination of the host and activator can determine the luminescent properties of a phosphor. The first phosphor material to be prepared was barium sulfide or BaS [1]. Today, there are a variety of phosphors, with or without activators/dopants, ranging from sulfides to oxides. Examples of sulfide phosphors are zinc sulfide (ZnS), cadmium sulfide (CdS) and lead sulfide (PbS) while oxide phosphors are zinc oxide (ZnO), cadmium oxide (CdO) or calcium tungstate (CaWO₄). These phosphors can be doped with rare-earth ions such as europium (Eu³⁺), terbium (Tb³⁺), and cerium (Ce³⁺) or with alkali metal ions such as manganese (Mn²⁺) or chromium (Cr²⁺) to tune the colour of their emissions. Major drawback of sulfide phosphor was the need to use harmful substances at relatively high temperature to prepare them, they are also chemically unstable and they decomposes quickly in moist air yielding poisonous gases such as hydrogen sulfide (H₂S) and sulfur dioxide (SO₂). In searching for more chemically and thermally stable materials, today there are new types of phosphors based on aluminates (zinc alluminates or ZnAl₂O₄), silicates (magnesium silicate or MgSiO₃) and phosphates (calcium phosphates or Ca_x(PO₄)₂). In line with the primary objective of this study, i.e. to prepare light emitting materials (phosphors) that can be used in phototherapy

lamps, it was necessary to work with phosphors that are biocompatible and non-toxic. Therefore, we prepared and investigated calcium phosphates co-doped with gadolinium (Gd^{3+}) and praseodymium (Pr^{3+}). Phosphates are considered an excellent hosts for rare-earth dopant ions to prepare phosphors because of, among other things, excellent properties such as, chemical stability, non-toxicity, biocompatibility, osteoconductivity, bioactivity, non-immunogenicity and they are also noninflammatory [2, 3]. Furthermore, they can easily form direct chemical bonds with living tissues.

2.3 Calcium phosphates

Calcium phosphate is the name given to a family of minerals containing calcium ions (Ca^{2+}) together with orthophosphates (PO_4^{3-}), metaphosphates or pyrophosphate ($P_2O_7^{4-}$) and occasionally hydrogen or hydroxide ions. There are different kinds of calcium phosphates that have been prepared, namely monocalcium phosphate monohydrate (MCPM, $Ca(H_2PO_4)_2 \cdot H_2O$), dicalcium phosphate dehydrate (DCPD, $CaHPO_4 \cdot 2H_2O$), octacalcium phosphate (OCP, $Ca_8(HPO_4)_2(PO_4)_4 \cdot 5H_2O$), α -tricalcium phosphate (α -TCP, α - $Ca_3(PO_4)_2$), β -tricalcium phosphate (β -TCP, β - $Ca_3(PO_4)_2$), hydroxyapatite (HA, $Ca_{10}(PO_4)_6(OH)_2$), and fluorapatite (FA, $Ca_{10}(PO_4)_6F_2$) [4]. In this study we investigated hydroxyapatite and tricalcium phosphates.

Hydroxyapatite is a calcium phosphate mineral with the basic formula $Ca_5(PO_4)_3X$, where X represents the hydroxyl group. The unit cell of the hydroxyapatite has a hexagonal crystal structure denoted by $P6_3/m$. The unit cell parameters are $a = 9.43 \text{ \AA}$ and $c = 6.88 \text{ \AA}$, and its atomic ratio Ca/P is 1.67. Each unit cell has 6 equivalent phosphorus sites and 2 crystallographic sites of Ca referred to as Ca (1) and Ca (2). Due to chemical substitution within the apatite lattice, the Ca^{2+} sites can be occupied by a number of cations, namely Sr^{2+} , Mn^{2+} , Fe^{2+} , Y^{3+} , Na^+ and rare earth elements ($REE^{2+/3+}$) [5]. Ca (1) has 4 atoms per unit cell and Ca (2) has 6 atoms per unit cell [6]. Ca (2) sites are unoccupied while most of Ca (1) sites are filled. The structure is formed by tetrahedral arrangement of phosphate (PO_4^{3-}). The P^{5+} is surrounded by O^{2-} ions in the tetrahedral arrangements. Each tetrahedron contains oxygen atoms referred to as O1, O2, and O3 (NB: there are 2 O3 in a tetrahedron).

The oxygen atoms are connected to Ca (1) and Ca (2). The crystalline structure of hydroxyapatite is shown in figure 2.1.

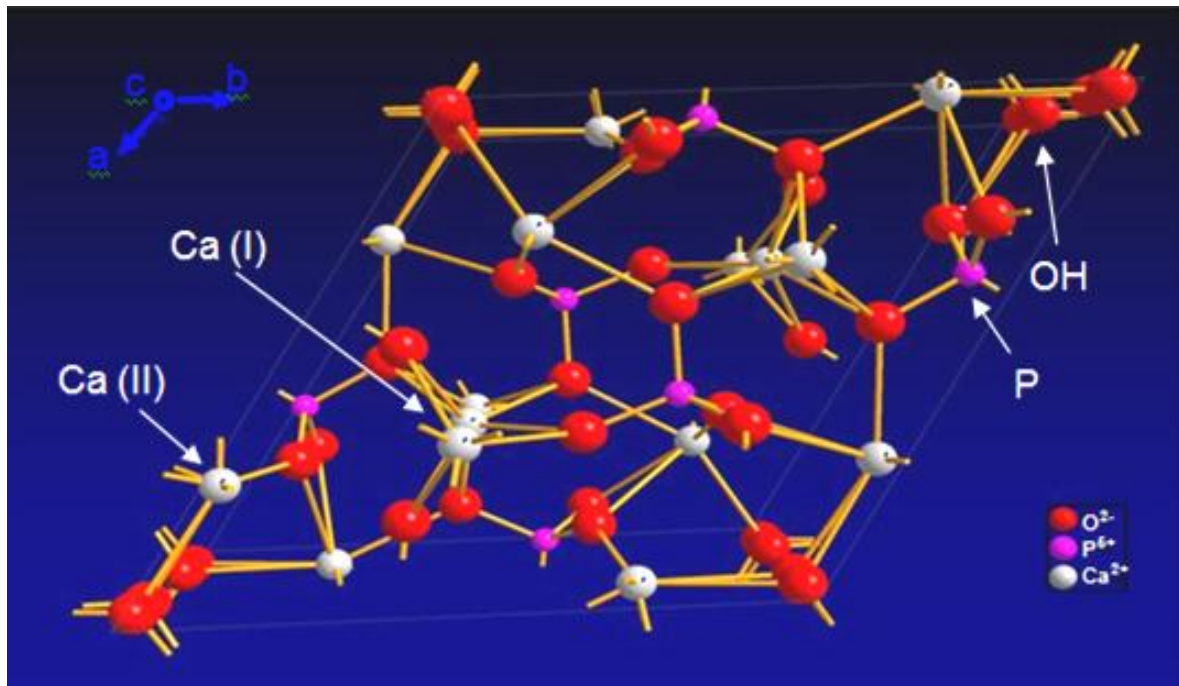


Figure 2.1 Crystalline structure of hydroxyapatite [7].

Tricalcium phosphate is a tertiary calcium phosphate also known as bone ash ($\text{Ca}_3(\text{PO}_4)_2$). It is known to be rich in calcium and phosphorus, and it can be easily assimilated and absorbed [8]. Tricalcium has three polymorphs referred to as $\beta\text{-Ca}_3(\text{PO}_4)_2$, $\alpha\text{-Ca}_3(\text{PO}_4)_2$ and $\alpha'\text{-Ca}_3(\text{PO}_4)_2$. $\beta\text{-Ca}_3(\text{PO}_4)_2$ is stable at room temperature and reconstructively transforms at 1125 °C into $\alpha\text{-Ca}_3(\text{PO}_4)_2$, which is metastably retained until room temperature during the cooling. For optical applications, $\beta\text{-Ca}_3(\text{PO}_4)_2$ is utilized in the powder form and polycrystalline materials. $\beta\text{-Ca}_3(\text{PO}_4)_2$ is reported to have the rhombohedral space group $R\bar{3}c$ with unit cell $a = b = 10.439 \text{ \AA}$, $c = 37.375 \text{ \AA}$, and $\alpha = \beta = 90^\circ$, $\gamma = 120^\circ$ (hexagonal settings). Shown in figure (2.2) is the unit cell of $\beta\text{-Ca}_3(\text{PO}_4)_2$. Tetrahedra represent the PO_4 groups, small blue balls represent Ca atoms, and big green balls labelled from 1 to 6 represent Ca's with half occupancy [9].

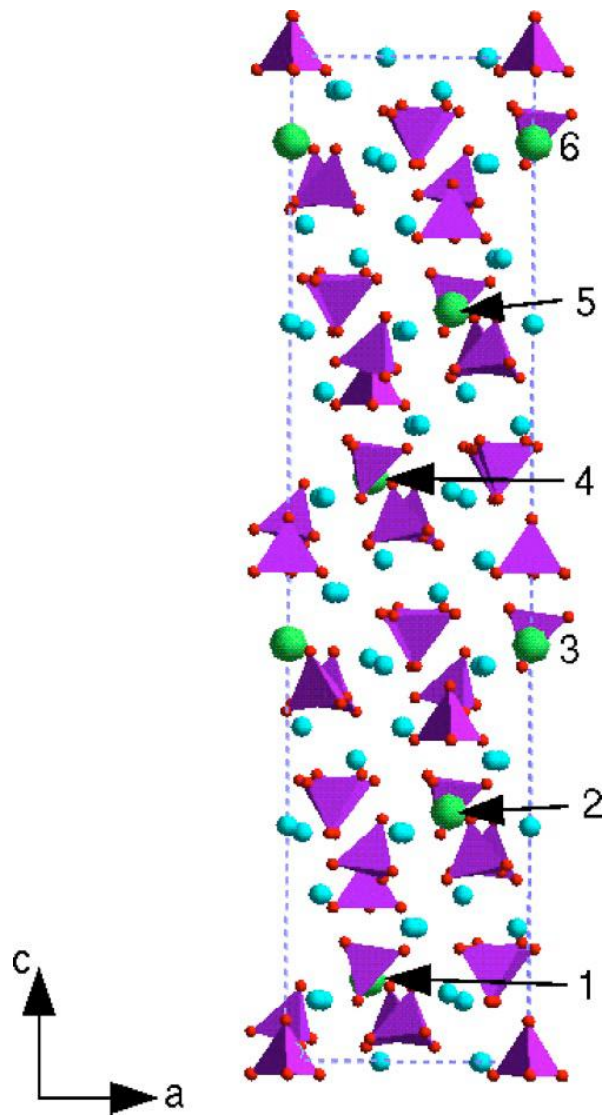


Figure 2.2 β - $\text{Ca}_3(\text{PO}_4)_2$ unit cell plane [9].

2.4 Gadolinium

Gadolinium (Gd^{3+}) is silver-white, malleable, ductile ferromagnetic trivalent element of the rare earth group. It is electropositive and dissolves slowly in cold water and quickly in warm water and dilute mineral acids. It occurs in nature in its salts and especially as the oxide gadolinia. It absorbs neutrons more effectively than any other known substance. This property is caused by two isotopes that are present only to a limited extent in natural gadolinium and it is used for shielding in neutron radiography and in nuclear reactors [10-11]. It is hexagonal, with closely-packed α -form at room temperature, but it transforms into

β - form which has body-centered cubic structure when heated to temperature above 1235 °C. It is ferromagnetic at temperature below 20 °C, and is strongly paramagnetic above this temperature. It is also known as a strong reducing agent, which reduces oxides of several metals into their elements.

2.4.1. Applications of Gd³⁺

Gd³⁺ is used as a secondary, emergency shut-down measure in some nuclear reactors and also in nuclear marine propulsion systems as a burnable poison. It is used as a magnetic resonance imaging to enhance images in medical magnetic resonance imaging (MRI) and magnetic angiography procedures. It makes certain tissues, abnormalities or diseases process more clearly visible on a MRI scans [11]. It is also used as a dopant to prepare phosphors that can be used in lighting applications including color television sets and phosphor lamps.

2.4.2. Luminescent properties of Gd³⁺ ion

Gd³⁺ has good luminescent properties and stable physical or chemical characteristics as a member of the rare earth ions. It has the following electron configuration [Xe]4f⁷ 5d¹ 6s². Gd³⁺ ion is isoelectronic; its 4f⁷5d¹ state lies at much higher energy, as a consequence, the luminescence of Gd³⁺ ion consists of sharp line ⁶P → ⁸S transitions, mainly at 313 nm. Due to its high energetic position, this emission can only be observed in lattices with optical absorption at high energy [12]. The trivalent Gd³⁺ ion has seven unpaired electrons in the unfilled 4f shell, which is shielded by the completely filled 5s and 5p shells [13]. Figure 2.3 illustrates the energy level diagram of Gd³⁺ ion with different transition levels corresponding to different emission lines.

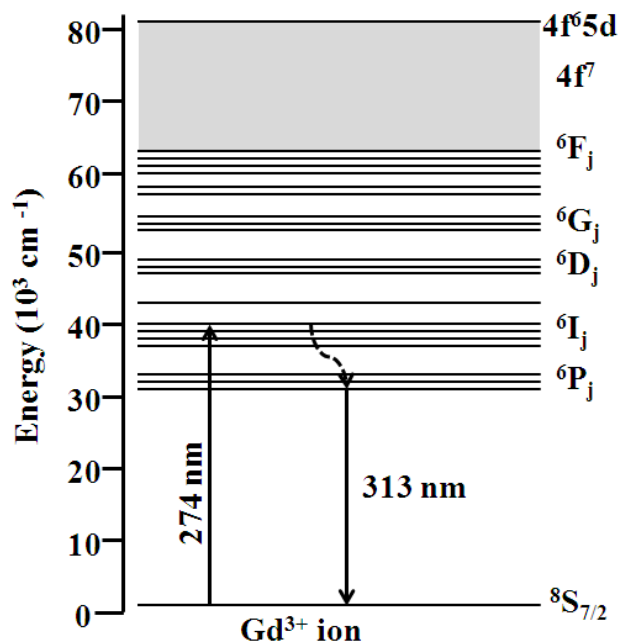


Figure 2.3 Energy level scheme in the range 0 – 80 000 cm⁻¹ of Gd³⁺ ion [14].

2.5 Praseodymium

Praseodymium (Pr³⁺) is a soft, silvery, malleable, ductile rare-earth element that develops characteristic green tarnish in air. It occurs naturally with other rare earths in monazite and is used to color glass and ceramics yellow, as a core material for carbon arcs, and in metallic alloys [15]. It is too reactive and when prepared, it slowly develops a green oxide coating. It reacts slowly with cold water and quite quickly with hot water to form praseodymium hydroxide. It also reacts with oxygen in air to form praseodymium oxide. To protect it from reacting with moisture and/or air, it is stored under mineral oil or covered with plastic wrap. Praseodymium occurs naturally as a trivalent Pr (III) rare-earth ion. It is more resistant to corrosion in air than other rare-earth ions such as europium, lanthanum, cerium, or neodymium and it is also paramagnetic at any temperature above 1 K. It occurs in oxidation states +2, +3, and +4, because it is a strong oxidant thus in aqueous solution, only the +3 oxidation state is encountered.

2.5.1 Applications of Pr³⁺

Pr³⁺ is present in the rare earth mixture whose fluorides form the core of carbon arc lights which are used in the motion picture industry for studio lighting and projector lights. It also has the ability to give glass a nice yellow color. This glass filters out the infrared radiation, so that it is used in the goggles which protect the eyes of welders. Silicate crystals doped with praseodymium ions have been used to slow a light pulse down to a few hundred meters per second. Praseodymium compounds gives and enamels a yellow color [16]. Like Gd³⁺, Pr³⁺ can also be used as a dopant to prepare phosphors that can be used in lighting applications. In this study, Pr³⁺ was used as sensitizer. In other words it acted to harvest and transfers the primary excitation energy to Gd³⁺. The energy transfer process will be discussed in detail at the end of this chapter.

2.5.2 Luminescent properties

Pr³⁺ is one of the rare earth ions that have been widely used as an activator for different host materials to prepare phosphors. It has the [Xe] 6s²4f³ electron configuration. It is known to exhibit very interesting prospects as an activator ion for luminescence and laser action, because its energy levels contains metastable multiplet states [17] that offer the possibility of efficient emissions such as red, green, blue, and ultraviolet (from the 4f5d state) at different transition levels. The emission of Pr³⁺ strongly depends on the structure of the host lattice, the concentration of the activator, and the excitation conditions. The emission of the electromagnetic radiation comes when the excited electrons are de-excited from higher energy level to lower lying energy level. Figure 2.4 shows the energy level diagram of Pr³⁺ with energy scale up to 60 000 cm⁻¹, which consists of large number of energy levels. The broken arrow present the non-radiative process of the phosphor, meaning that only heat is given off not light.

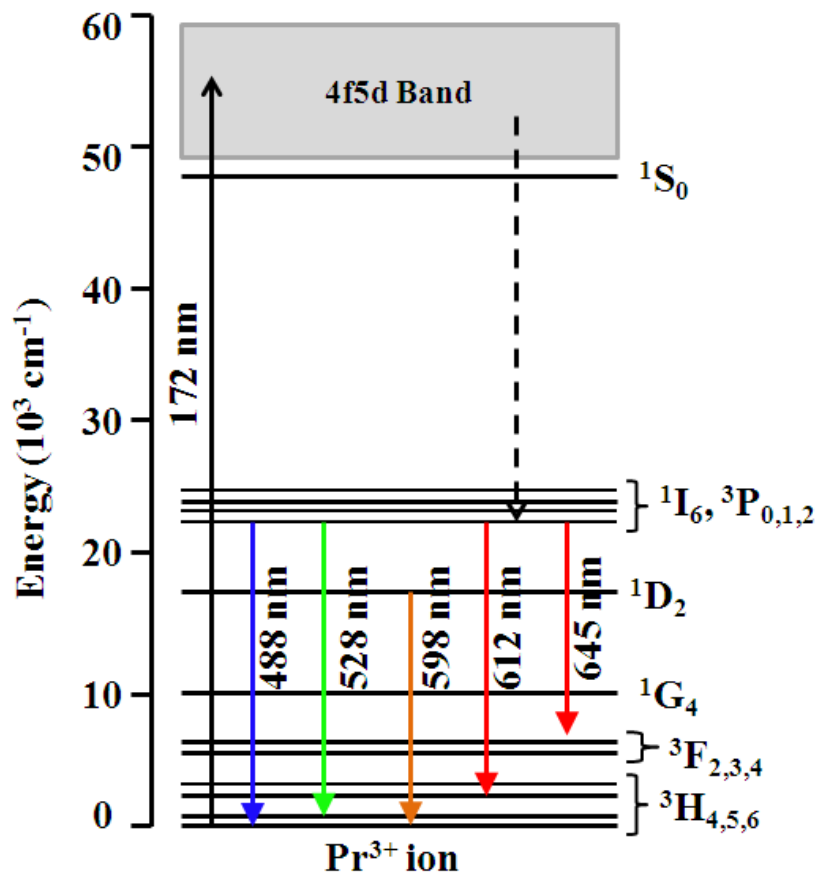


Figure 2.4 The energy level diagram of Pr³⁺ ion [18].

2.6 Luminescence

Luminescence is the process of emission of light from phosphor materials, when excited by certain external energy, and then the excitation energy is given off as light [19]. It is divided into two types, namely fluorescence and phosphorescence. Fluorescence is emission of light by material whilst is still subjected to the excitation source, and the luminescence stops immediately after the excitation source has been removed. Phosphorescence is the emission of light from material exposed to radiation and persisting as an afterglow after the exciting radiation has been removed. The emitted light can last for about 10⁸ seconds after the excitation has been removed. There are different types of luminescence such as cathodoluminescence, electroluminescence, photoluminescence, thermoluminescence, etc. Our study is mainly focused on the photoluminescence and thermoluminescence for fundamental understanding, and only these two processes will be discussed in more details.

2.6.1 Photoluminescence

Photoluminescence is a process in which a substance absorbs photons and then re-radiates photons [20]. It can be further described as an excitation to a higher energy state and then a return to lower energy state accompanied by the emission of a photon. The period between absorption and emission is typically extremely short, in order of 10 nanoseconds. Figure 2.5 (a) below shows the luminescence process occurring in the host material, when the emission is due to band-band transitions within the material. The energy (or photons) is excited from the valance band to conduction band and is then given off in a form of light from high energy level to the valance band (see figure 2.5 (a)). Incorporation of dopants in the host material may cause change in host transition if the luminescence is emitted by dopants. The emission can be from different transition levels of dopants as shown in figure 2.5 (b). The optical emission associated with photoluminescence is generally into two types: intrinsic and extrinsic.

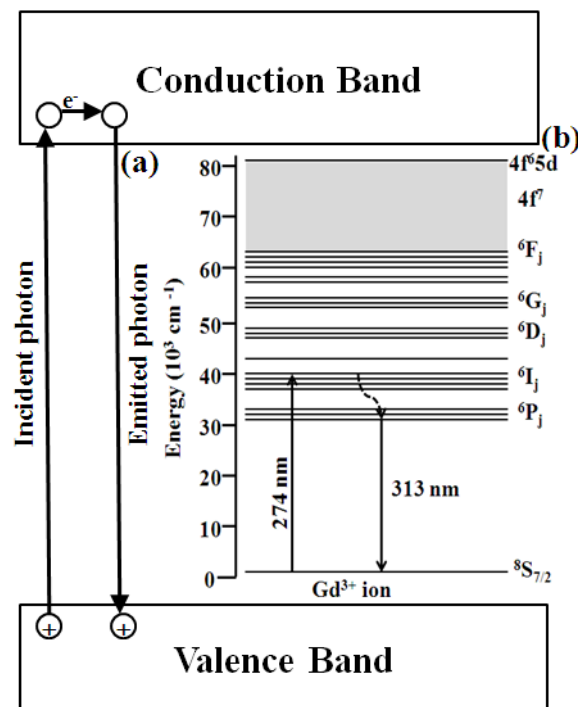


Figure 2.5 Photoluminescence process.

2.6.1.1 Intrinsic photoluminescence

The intrinsic luminescence is native to host materials and involves band-to-band recombination of electron-hole pairs. It is also associated with lattice defects (anion vacancies) within the minerals. This type of luminescence is referred to as a defect center. Band-to-band emission results from the recombination of an electron in the conduction band with a hole in the valence band. This can only be observed in pure crystals at relatively high temperature [21]. There are several factors that may influence intrinsic photoluminescence such as: non-stoichiometry which is a state of material (semiconductor) not having exactly the correct elemental proportion, and structural imperfection owing to poor ordering, radiation damage, or shock damage [22].

2.6.1.2 Extrinsic photoluminescence

Extrinsic photoluminescence is divided into two categories, namely localized and delocalized luminescence. In localized luminescence the excitation and emission processes are confined in a localized luminescence center, the host lattice does not contribute to luminescence process [21]. Delocalized luminescence, the excited electrons and holes of the host lattice participate in the luminescence process.

2.6.2 Thermoluminescence

Thermoluminescence is a process of irradiating a material with electrons which are transferred to the traps and later given off as luminescence when heated. High energy radiation creates excited states in crystalline materials. These states are trapped for extended periods of time by localized defects in the lattice interrupting the normal intermolecular or inter-atomic interactions in the crystal lattice. Heating the material enables the trapped states to interact with phonon and rapidly decay into lower-energy states, causing the emission of photons in the process. Once the material is heated to excite the light emission the material cannot be made to emit thermoluminescence again by simply cooling the specimen and

reheating. In order to re-exhibit the luminescence the material must be exposed to radiation, whereupon raising the temperature will once again produce light emission [23].

2.7 Quenching of Luminescence

Quenching of luminescence is process which decreases the luminescent intensity of a substance. Luminescence quenching can be caused by variety of process, such as addition of impurities to the phosphor, when the concentration of the luminescent substance is increased, when the luminescent substance is heated, or when the substance is exposed to infrared radiation or an electric field. The luminescence quenching experienced in these studies is due to increased concentration and heating of the luminescence substances.

2.8 Energy Transfer process in Rare Earth Phosphors

Energy transfer is the process where the excitation energy of a certain ion migrates to another ion. One of the ions can be that of the host lattice or a co-activator in the lattice. The mechanism of energy transfer involves a donor (D) in an excited electronic state to transfer its excitation energy to a nearby acceptor (A) in a non-radiative fashion. In phosphors, energy transfer between two centres requires interaction between the centres. The two centres can be identical (e.g. two identical ions in a host lattice) or non-identical (e.g. two different ions in a host lattice) [24]. Energy transfer manifests in decreasing or quenching of the donor fluorescence and a reduction of excited state lifetime accompanied by an increase in acceptor fluorescence intensity.

There are few criteria that must be satisfied in order for energy transfer to occur. These are (i) the donor and acceptor must be in the close proximity to one another, typically from 1 to 10 nm. That is the probability from D to A (critical distance (R_c)) should be higher than separation (R) distance, ($R < R_c$) as demonstrated in figure 2.6. Radiation emission from D is most probable when $R > R_c$.

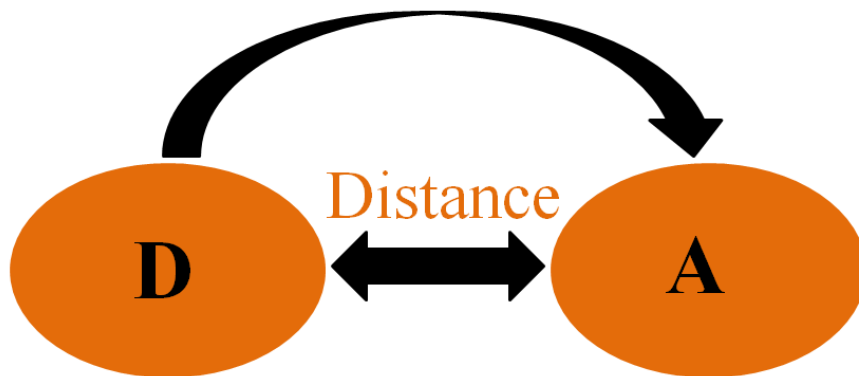


Figure 2.6 The probability of energy transfer by critical distance (R_c)

(ii) The rate of energy transfer is known to be proportional to the spectral overlap between the donor emission and the acceptor absorption. The transfer rate from a broad band donor to a broad band acceptor is faster than that from a broad band donor to a narrow line acceptor due to anticipated larger spectral overlap in band-to-band processes. Figure 2.7 shows the discussed spectral overlap of the fluorescence from the donor and absorption of the acceptor.

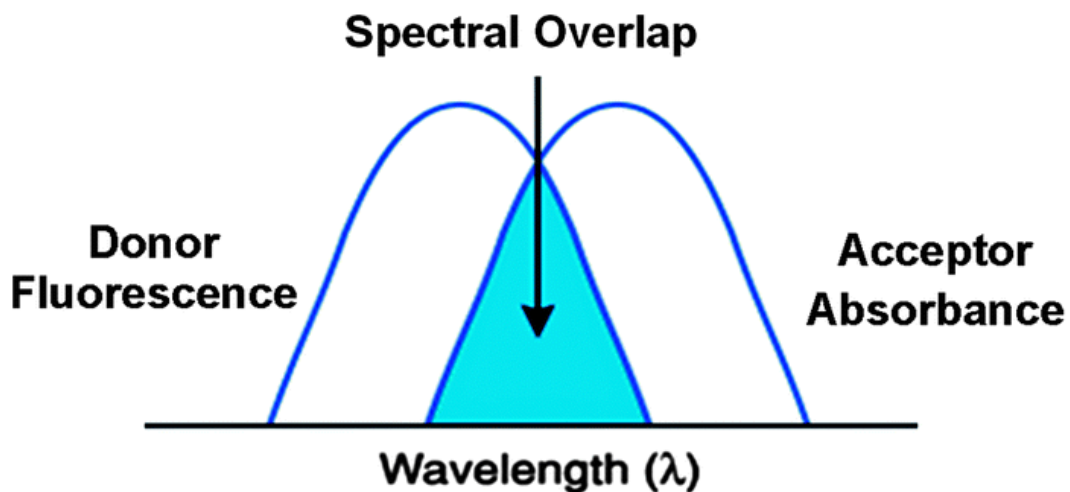


Figure 2.7 Absorption and fluorescence spectra of an ideal donor-acceptor pair [25].

(iii) The transition of the donor and acceptor must be approximately parallel to each other for the energy transfer to occur, meaning that the energy transfer can occur if the ground and excited states of the sensitizer (D) and the activator (A) are equal or are in resonance condition as shown by figure 2.8. S_0 signifies the ground state and S_n represents an excited state. The transfer may be either a quantum mechanical exchange or an electric or multipolar interaction [24].

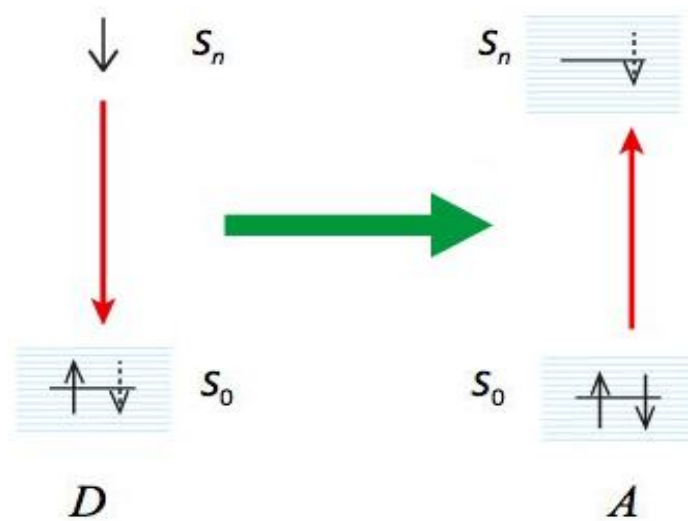


Figure 2.8 The energy transfer process at parallel energy level [26].

2.9 Application of phosphors

Applications of phosphors includes most of the optical sensors in biomedical fields, lasers, optoelectronic devices, luminous paint with long persistent phosphorescence, phosphors for energy harvesting, phosphors for solid lighting including OLEDs, and phosphor flat panel displays [27-33]. The phosphors prepared in this study were investigated for use in the phototherapy lamp to treat different kinds of skin diseases.

2.9.1 Phototherapy Lamps

Phototherapy lamp is the lamp that is used for treatment of disorder, especially on skin by exposure to light, including ultraviolet and infrared radiation. It uses artificial ultraviolet-blue radiation delivered by fluorescent lamps to cure skin diseases. Phototherapy lamp with a wavelength of 311 nm is specifically designed for treatment of vitiligo, psoriasis, eczema, and a range of dermatological conditions. The lamp has direct interaction of light of certain frequencies with tissue to cause a change in immune response [34]. There are two types of phototherapy lamps: the conventional phototherapy light which has been used for over 40 years and fibreoptic phototherapy device which has been available for nearly 15 years. The

conventional device use one or more tungsten halogen bulb, a metal halides gas discharge tube, long or compact fluorescent lamp, or mostly recently, light emitting diodes (LEDs). The fibreoptic phototherapy device uses a standard light source, usually a quartz halogen bulb. The light from the bulb may be passed through a filter before being channeled down a fibreoptic bundle into a pad of woven optic fibres. The lamp is placed next to the skin for the treatment. Fluorescent tubes have advantages of being inexpensive but their light intensity, irradiance reduces with time and its lifetime range from 1000 to 2000 hours.

Phototherapy device uses ultraviolet radiation (UVR) for treatment of skin disorders. UVR is part of electromagnetic spectrum that reaches the earth from the sun. It has wavelength shorter than visible light, making it invisible to human eye. UVR is divided into three categories: ultraviolet A (UVA, 400-320 nm), ultraviolet B (UVB, 320-280 nm), and ultraviolet C (UVC, 280-200nm). These categories are shown in figure 2.9 below.

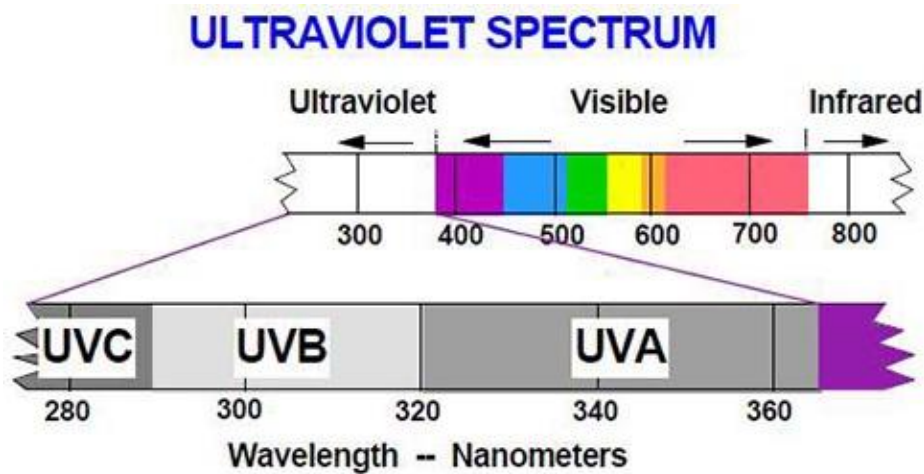


Figure 2.9 Shows the ultraviolet portion of the electromagnetic spectrum [35].

Most of UVC is absorbed by the ozone layer and does not reach the earth. UVC is also hazardous for human skin and is generally used in germicidal applications such as killing bacteria in drinking water. UVA and UVB are used in treating various skin diseases. The specific UVR used in the phototherapy lamp is UVB. UVB radiation is subdivided into broadband and narrowband emissions located respectively at the wavelengths of 290 – 320 nm and 313 nm respectively.

Figure 2.10 (a) shows the UVB broadband and spectrum of erythema. Erythema is dominated at the lower wavelength of less than 305 nm of the UVB range [36]. UVB broadband produces large amount of light in the erythemogenic range causing burning of the skin. Erythema is a risk factor for skin disease, so the lamp should be less carcinogenic for the same therapeutic results. Figure 2.10 (b) shows the narrowband UVB at a single wavelength of 311 nm. Narrowband UVB is much safer and effective to use because it emit a light over a very short range of wavelength directed in the therapeutic range, and it can be delivered before erythema occurs. Disadvantage of UVB narrowband is that a longer treatment time is required, or equipment with more bulbs to achieve the same dosage threshold.

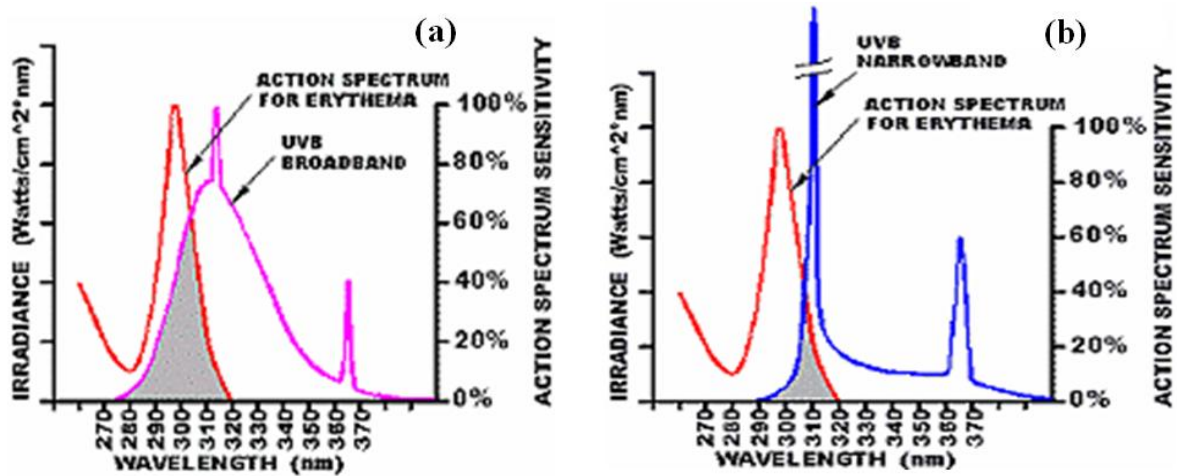


Figure 2.10 (a) Shows the spectrum the erythema and Broadband UVB, (b) Narrowband 311 nm Source Spectra [36].

Broadband UVB emit light in a broad range over the UVB spectrum, including both the therapeutic wavelengths specific to the treatment of skin diseases and the shorter wavelength responsible for sunburning (erythema). Sunburning has a negative therapeutic benefit, increases the risk of skin cancer, causes patient discomfort, and limits the amount of therapeutic UVB that can be taken. Gd^{3+} ion was chosen to be a good candidate as an activator, because of its properties to give luminescence at 311 nm, and Pr^{3+} ion is incorporated to enhance the emission of Gd^{3+} in the UV range.

2.9.2 Applications of phosphor in the phototherapy lamp.

The lamp contains the basic element: bulb, base, electrodes, phosphors, gases, and mercury. The base hold lamp firmly in the lamp holders or sockets and providing the electrical connections for the lamp/ballast circuit. Electrodes are coiled with tungsten wires. Electrons from electrodes bombard mercury atoms producing ultraviolet rays. The lamp contains a small bit of mercury and gases (Xenon, Krypton and Argon), kept under very low pressure. Phosphors are coated powders on the inside of the bulb; it converts the ultraviolet radiation to visible light.

When the lamp is turn on, the current flows through the electrical circuit to the electrodes. The voltage across the electrodes will cause the electrons to migrate through the gas from one end of the tube to the other end. The energy changes some of the mercury in the tube from liquid to a gas. As electrons and charged atoms move through the tube, some of them collide with the gaseous mercury atoms. The collisions excite the atoms, bumping electrons up to higher energy levels. When the electrons return to their original energy level, they release light photons [37]. Figure 2.11 shows the basic elements in the lamp. Figure 2.12 shows the image of skin disorder before and after treatment.

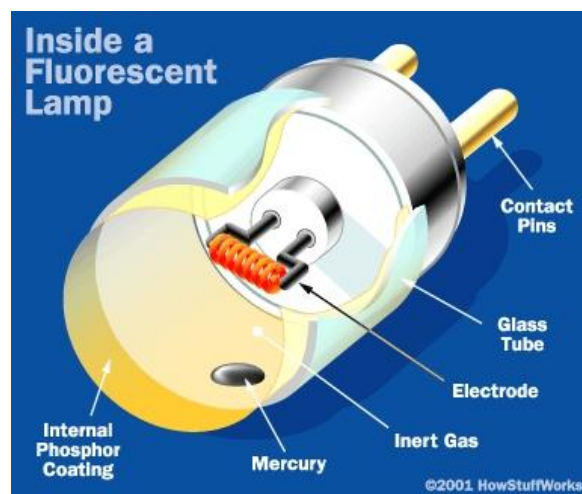


Figure 2.11 Fluorescent lamp showing basic elements in the lamp [37].



Figure 2.12 Fluorescent lamp showing basic elements in the lamp and treated skin disorder [38].

References

- [1] D. Poelman, A. Parmentier, K. Korthout, K. Van den Eeckhout, N. Avci, I. Cimieri, J. Botterman, P.F. Smet, In *EL 2010, Abstracts*, 28–29. Society for Information Display (SID) (2010).
- [2] I.M. Hung, W.J. Shih, M.H. Hon, M.C. Wang, *Int. J. Mol. Sci.*, 2012, **13**, 13569-13586
- [3] B. Mirhadi, B. Mehdikhani, N. Askari, *Process. Appl. Ceram.*, 2011, **5**, 193-198
- [4] F. Chen, Y. Zhu, J. Wu, P. Huang, D. Cui, *Nano Biomed. Eng.*, 2012, **4**, 41-49
- [5] U. Kempe, J. Götze, *Mineral. Mag.*, 2002, **66**, 151-172
- [6] <http://rmrc.wisc.edu/wp-content/uploads/2012/10/Proj31FinalRpt.pdf> [accessed November 2013]
- [7] [http://cdn.intechopen.com/pdfs/17643/InTech/Hydroxyapatite/based/materials/synthes is/and/characterization.pdf](http://cdn.intechopen.com/pdfs/17643/InTech/Hydroxyapatite/based/materials/synthes%20is/and/characterization.pdf) [accessed November 2013]
- [8] S.B. Sulaiman, T.K. Keong, C.H. Cheng, A.B. Saim, R.B.H Idrus, *Indian J. Med. Res.*, 2013, **137**, 1093-1101.
- [9] X. Yin, M.J. Stott, *Phy. Rev. B*, 2003, **68**, 205205-8
- [10] <http://www.infoplease.com/encyclopedia/science/gadolinium.html> [accessed November 2013]
- [11] <http://en.wikipedia.org/wiki/Gadolinium> [accessed November 2013]
- [12] S.C. Gedam, *Res. J. Physical Sci.*, 2013, **1**, 6-10
- [13] J.M. Zavada, N. Nepal, J.Y. Lin, H.X. Jiang, E. Brown, U. Hömmerich, J. Hite, G.T. Thaler, C.R. Abernathy, S.J. Pearton, R. Gwilliam R, *Appl. Phys. Lett.*, 2006, **89**, 152107-3
- [14] Z. Yang, J.H. Lin, M.Z. Su, Y. Tao, W.J. Wang, *J. Alloy Compd.* 2000, **308**, 94-97
- [15] <http://www.thefreedictionary.com/praseodymium> [accessed November 2013]
- [16] <http://en.wikipedia.org/wiki/Praseodymium> [accessed November 2013]
- [17] F.S. Kao, T.M. Chen, *J. Solid. State Chem.*, 2000, **155**, 441-446
- [18] Y. Chen, J. Wang, C. Liu, J. Tang, X. Kuang, M. Wu, Q. Su, *Opt. Express*, 2013, **21**, 3161-9

- [19] http://shodhganga.inflibnet.ac.in/bitstream/10603/6157/8/08_chapter%201.pdf
[accessed December 2013]
- [20] <http://en.wikipedia.org/wiki/Photoluminescence> [December 2013]
- [21] D.R. Vij, *Luminescence of Solids*, Plenum Press, New York (1998), 95-102.
- [22] B.M. Mothudi, H.C.Swart, O.M. Ntwaeaborwa, Ph. D dissertation, University of the Free State, South Africa, 2009
- [23] S.W.S. McKeever, *Thermoluminescence of Solids*, Cambridge (1985) 1-20
- [24] O.M. Ntwaeaborwa, H.C. Swart, R.E. Kroon, J.R. Botha, J.M. Ngaruiya, P.H. Holloway, *Photoluminescence Research Progress*, New York (2008) 287-306
- [25] N. Kumar, V Bhalla, M. Kumar, *Analyst*, 2014, **139**, 543-558
- [26] <http://biologicalphysics.iop.org/cws/article/lectures/53480> [accessed November 2013]
- [27] B.A. Holm, E.J. Bergey, D. Tapas, D.J. Rpdman, R. Kapoor, L. Levy, C.S. Friend, P.N. Prasad, *Mole. Cryst. Liq. Cryst.* 2002, **374 (1)**, 589-598
- [28] <http://news.sciencemag.org/2004/07/quantum-dots-light-tumors> [accessed November 2013]
- [29] <http://scitechdaily.com/biologists-develop-bioelectric-signals-that-can-detect-early/cancer/> [accessed November 2013]
- [30] P.S. Mbule, O.M. Ntwaeaborwa, H.C. Swart, M. Sc dissertation, University of the Free State, South Africa, 2009
- [31] <http://www.compadre.org/informal/features/featuressummary.cfm?FID=1386>
[accessed November 2013]
- [32] <http://www.myvisiontest.com/newsarchive.php?id=1279> [accessed November 2013]
- [33] <http://taixun.en.alibaba.com/product/834946366/218448343/handle/barcode/scanner/laser/barcode/scanner/with/high/quality.html> [accessed November 2013]

- [34] P.D. Beslare, S.V. Moharil, C.P. Joshi, S.K. Omanwar, *AIP Conf. Proc.* 2011, **1391**, 194-196
- [35] <http://davidduke.com/how-do-you-know-if-you-are-getting-enough-vitamin-d>
[accessed December 2013]
- [36] http://www.solarcsystems.com/us_narrowband_uv.html [accessed November 2013]
- [37] <http://www.physics.hku.hk/~phys1055/lectures/chap03.html> [accessed November 2013]
- [38] <http://portuguese.alibaba.com/product-gs/psoriasis-phototherapy-lamps-psoriasis-vitiligo-eczema-atopic-dermatitis-373526406.html> [accessed November 2013]

Chapter 3: Research Techniques

3.1 Introduction

This chapter gives a brief description of the theory of different research techniques used in this study to characterize phosphor materials. The techniques include x-ray diffraction (XRD), x-ray photoelectron spectroscopy (XPS), scanning electron microscopy (SEM), high resolution transmission electron microscopy (HRTEM), UV-Vis spectrophotometry, photoluminescence (PL) spectroscopy, thermoluminescence (TL) spectroscopy and time-of-flight secondary ion mass spectrometry (TOF-SIMS).

3.2 X-ray Diffraction

XRD is an efficient analytical technique used for identification of structural properties of crystalline materials. It is also used for identification of phases, determination of crystallite size, lattice constants, and degree of crystallinity in a mixture of amorphous and crystalline materials. X-ray diffractometer consists of three basic elements: an X-ray tube, a sample holder, and an X-ray detector [1]. The X-rays are generated in a cathode ray tube by heating a filament to produce electrons, which are then accelerated towards a target by applying a voltage. When the electrons have sufficient energy to dislodge inner shell electrons of the target material, characteristic X-ray spectra are produced. The interaction of incident rays with the sample produces constructive interference when the conditions satisfy Bragg's Law:

$$n\lambda = 2d\sin\theta \quad (3.1)$$

where λ is the wavelength of the incident light rays, d is the distance between lattice planes, θ is the angle of incidence with lattice plane. This law relates the wavelength of electromagnetic radiation to the diffraction angle and lattice spacing in a crystalline sample as shown in figure 3.1. The figure shows the x-rays waves incident on the parallel planes of atoms in the crystal, with each plane reflecting a very small fraction in the radiation. The

diffracted beams are formed when the reflections from the parallel planes of atoms interfere constructively [2].

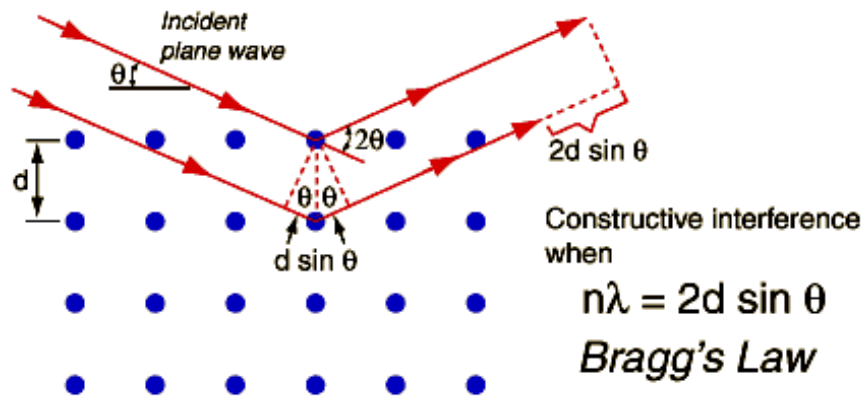


Figure 3.1 Schematic of the reflection of x-rays by crystal planes [3].

By scanning the sample through a range of 2θ angles when the detector is rotated at double angular velocity, all possible diffraction directions of the lattice should be attained due to the random orientation of the powdered material. The recorded spectra consists of several components, the most common being K_α and K_β . The specific wavelengths are characteristics of the target material such as copper (Cu), iron (Fe), molybdenum (Mo), and chromium (Cr). Copper is the most common target material for single-crystal and powder diffraction, with CuK_α radiation = 1.5418\AA [1]. The X-rays are collimated and directed onto the sample. As the sample and detector are rotated, the intensity of the reflected X-rays is recorded. The crystalline phases are determined from the diffraction patterns. The width of the diffraction lines correlates with the sizes of crystallites. As the crystallite sizes decrease, the line width is broadened due to loss of range order relative to the bulk. The average crystallite size, D , can be estimated from the broadened peaks by using Debye-Scherrer equation:

$$D = \frac{0.9\lambda}{\beta \cos \theta} \quad (3.2)$$

where β is the full width at half maximum of a diffraction line located at an angle θ and while λ is the X-ray Diffraction wavelength.

The D8 Advanced AXS GmbH X-ray diffractometer used in this study is shown in the figure 3.2. The XRD patterns were recorded in the 2θ range of 10° - 80° at a scan speed of $0.02^\circ \text{ s}^{-1}$,

accelerating voltage of 40 kV and current of 40 mA. A continuous scan mode with coupled 2θ scan type was used.



Figure 3.2 D8 Advanced AXS GmbH X-ray diffractometer [4].

3.3 X-ray Photoelectron Spectroscopy

XPS is a quantitative spectroscopic technique that measures the elemental composition, empirical formula, chemical state and electronic state of the elements that exist within a material [5]. It is routinely used to measure organic and inorganic compounds, metal alloys, semiconductors, polymers, elements, catalysts, glasses, ceramics, paints, papers, inks, woods, bio-materials and many others [5]. The sample is irradiated with low-energy (~ 1.5 KeV) X-rays while simultaneously measuring the kinetic energy and number of electrons that escape

from the top 1 to 10 nm of the material being analyzed. Figure 3.3 shows the schematic diagram of XPS technique. X-ray excitation ejects electrons from the core level of the atoms, which will be accelerated to the detected via the cylindrical mirror analyzer as shown in the figure.

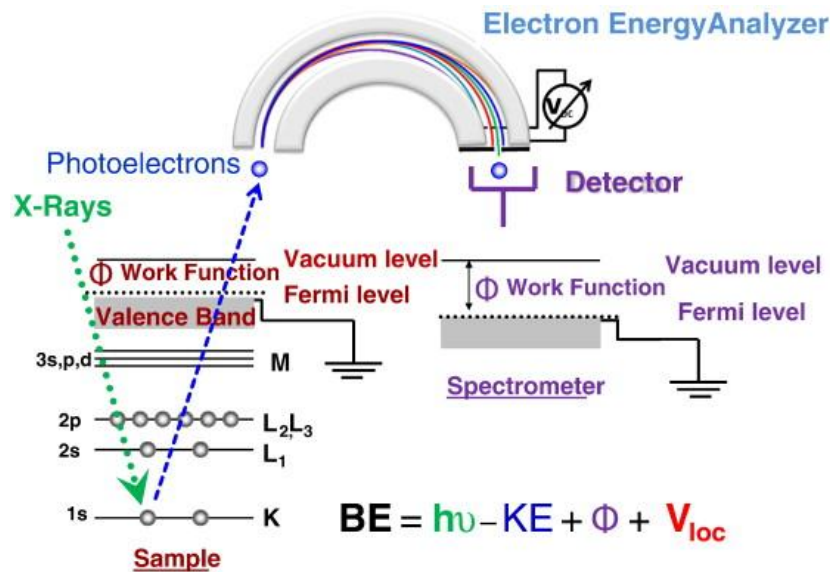


Figure 3.3 Schematic diagram of the XPS technique [6].

The energy spectrum of the emitted photoelectron is determined by means of a high-resolution electron spectrometer. The kinetic energy (K.E.) of the emitted photoelectron is related to the x-ray energy of an atomic binding energy (B.E.) by Einstein's equation for photoelectric effect:

$$B.E. = h\nu - K.E. - \phi_{spec} , \quad (3.3)$$

where $h\nu$ is the energy of the primary x-ray photons, K.E. is the kinetic energy of the electron measured by the instrument and ϕ_{spec} is the work function of the spectrometer [6]. Each element produces a characteristic set of XPS peaks at characteristic binding energy values that directly identify each element that exists on the surface of the material being analyzed. These characteristics peaks correspond to the electron configuration of the electron within the atoms, e.g., 1s, 2s, 2p, 3s, 3p, 3d etc. The number of detected electrons in each of the characteristic peak is directly related to the amount of element within the irradiated area. The sample analysis is conducted in an ultra-high vacuum (UHV) chamber, because electron

counting detectors in XPS instruments are few meters away from the material irradiated with X-rays.

XPS surveys are done with 100 μm , 25 W, and 15 kV monochromatic beam. Depth profiling are done with 2 kV, 2 μA , and 1 \times 1 mm raster – Ar ion gun, with a sputter rate of about 170 $\text{\AA}/\text{min}$. SXI images done with 10 μm , 1.25 W and 15 kV x-ray beam. Figure 3.4 shows the Versa Probe II Scanning XPS Microprobe used during the measurements.



Figure 3.4 PHI 5000 Versa Probe II Scanning XPS Microprobe [7].

3.4 Electron Microscope

Electron microscope is a type of microscope that uses an electron beam to create an image of the specimen. It is capable of attaining much higher magnifications than the conventional light microscope and it has a greater resolving power than the light microscope. This allows for the detection of smaller objects in finer details because electrons have wavelengths about 100 000 times shorter than visible light photons. The electron microscope uses electrostatic and electromagnetic lenses to control the electron beam and focus it to form an image. They are used to investigate particle morphology and the structure of a wide range of biological and inorganic specimens including microorganisms, cells, large molecules, metals and crystals [8]. Modern electron microscopes produce electron micrographs, using specialized digital cameras or frame grabbers to capture the image. There are two general types of electron

microscope: Scanning Electron Microscope (SEM) and Transmission Electron Microscope (TEM).

3.4.1 Scanning Electron Microscope

SEM is a type of electron microscope that produces images of a sample by scanning it with a focused beam of electrons [9]. The microscope operates at a high vacuum. The SEM generates a beam of incident electrons in a column above the sample chamber. The electrons are produced by a thermal emission source, such as a heated tungsten filament, or by a field emission cathode [10]. The electrons are focused into a small beam by a series of electromagnetic lenses in the SEM column. Scanning coils direct and position the focused beam onto the sample surface. The electron beam is scanned in a raster pattern over the surface for imaging. The emitted electrons are detected for each position in the scanned area by an electron detector. Figure 3.5 shows the basic construction of a SEM. Electrons from the electron gun located at the top of the column flow into the metal plate as acting as the anode by applying a positive voltage. From the anode they pass through the lens to the specimen stage. When the beam hits the sample, electrons are ejected from the sample. The secondary electron detector or backscattered electron detector are used to detect the electrons emitted from the specimen. The output of the secondary electron detector is transferred to display unit. The specimen is observed at high magnification.

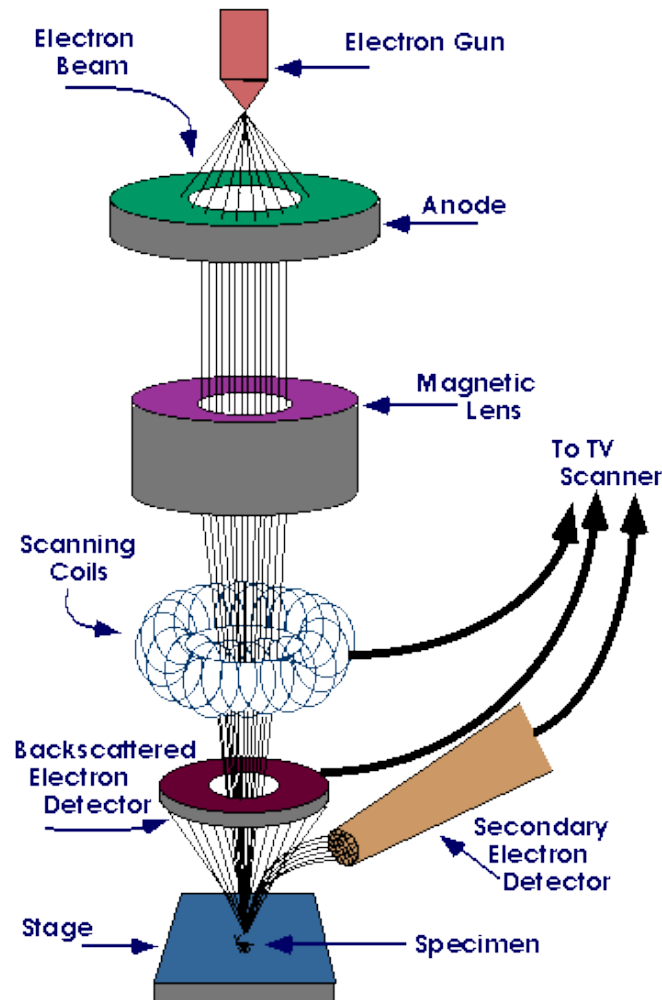


Figure 3.5 Schematic presentation of scanning electron microscopy [11].

High energy electrons that are rejected by an elastic collision of an incident electron are referred to as backscattered electrons. Backscattered provide high resolution imaging of the elemental composition, and surface topography. Elastic interaction between the sample and the incident electron beam produce backscattered electrons. Emitted low energy electrons resulting from inelastic scattering are secondary electrons [10]. Secondary electron provides high resolution imaging of fine surface morphology. Inelastic electron scattering is caused by the interaction between the sample's electron and the incident electrons that result in the emission of low-energy electrons from near the sample's surface. The intensity of the emitted electron signal is displayed on a cathode ray tube (CRT). By synchronizing the CRT scan to that of the scan of the incident beam, the CRT display represents the morphology of the sample surface area scanned by the beam. If the screen is 500 mm across and the scanned

area on the specimen is 5 mm across, the magnification is $\times 100$. To go to a higher magnification, a relatively small area must be scanned, for example, the scanned area is 0.5 mm across, the magnification is $\times 1000$, and so on [12]. Magnification is controlled by the current supplied to the scanning coils, or voltage supplied to the deflector plates, and not by the power of the objective lens. Figure 3.6 shows Superscan SSX-550 SEM-EDX technique used during the measurements.

For SEM unit, the specimen are scanned in the magnification ranging from $\times 20 \sim 300\,000$, with the accelerating voltage of 0.5 to 30 kV, 10 v step.



Figure 3.6 Shimadzu Super Scan SSX550 model SEM.

3.4.2 Transmission Electron Microscopy

TEM is a microscopy technique in which a beam of electrons is transmitted through a very thin sample and interacting with the sample as it passes through. Images are formed from the interaction of the electrons transmitted through the sample. The images are magnified and focused onto imaging devices or detected by sensor such as CCD camera. High resolution TEM has the capability to directly image atoms in crystalline samples at resolutions close to 0.1 nm, smaller than interatomic distance. An electron beam can also be focused to a diameter smaller than ~ 0.3 nm, allowing quantitative analysis from a single nanocrystal. This

type of analysis is important for characterizing materials at a length scale from atoms to hundreds of nanometers. It is used to measure the particle size, shape, crystallinity and interparticle interactions. Figure (3.7) below shows the schematic outline of TEM. It consists of four parts namely: electron source, electromagnetic lenses, sample holder and imaging system. The TEM used in this study was JEOL ARM200F transmission electron microscope at the national centre for microscopy at Nelson Mandela Metropolitan University. The ARM200F HRTEM is shown in figure 3.8.

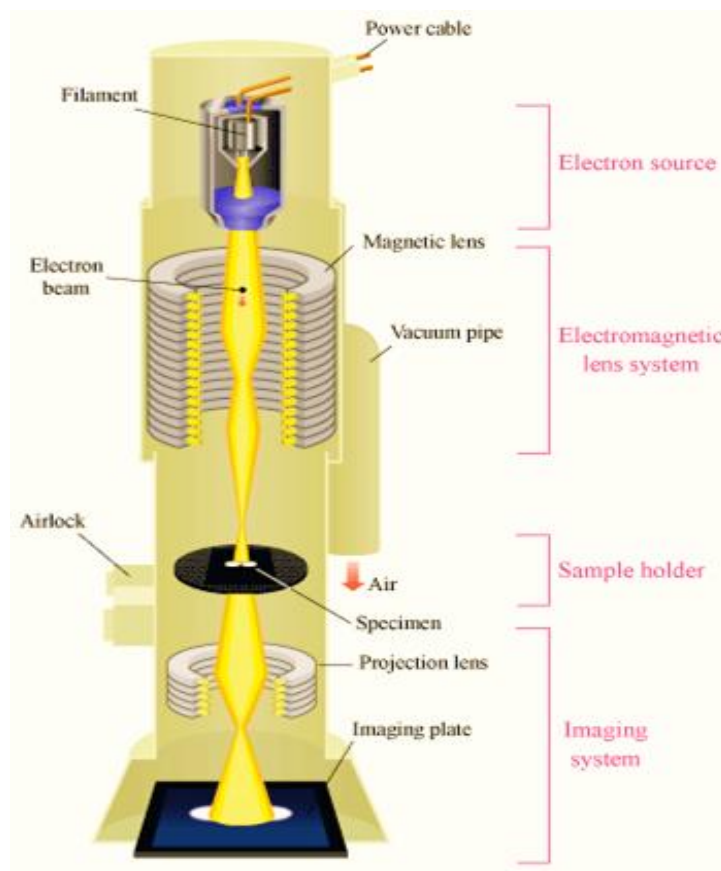


Figure 3.7 Schematic outline of TEM [13].

Electron beam produced in electron source passes through multiple electromagnetic lenses. It further passes through the solenoids (are tubes with coil wrapped around electron beam), down the column to the specimen, makes a contact with the screen where electrons are converted to light and form an image. The image can be manipulated by adjusting the voltage of the gun to accelerate or decrease the speed of electrons as well as changing the electromagnetic wavelength via solenoids. The coil focus image onto a screen or

photographic plate. Figure 3.8 shows high-resolution transmission electron microscope ARM 200F.



Figure 3.8 JEOL JEM-ARM200F[14].

3.5 Ultraviolet-visible spectrophotometer

UV-Vis spectrophotometry is a technique that involves absorption and/or reflectance of light (radiation) in the ultraviolet-visible spectral region. It measures the intensity (I) of light passing through a sample, and compares it to the original intensity (I_0) of light before it passes through the sample. The ratio I/I_0 is called the transmittance, and is expressed as a

percentage (%T). The absorbance (A) is related to the transmittance by the following equation:

$$A = -\log\left(\frac{\%T}{100}\right) \quad (3.4)$$

In the case of reflectance measurements, the spectrophotometer measures the intensity of light reflected from a sample (I) and compares it to the intensity of light reflected from a reference material (I_0). The ratio I/I_0 is the reflectance, and is expressed as a percentage (%R). Typically, the spectrophotometer consists of two light sources, deuterium (D2) and tungsten (W) lamps which covers ultraviolet (190-400 nm) and visible (300-2500 nm) spectral regions, respectively. Figure 3.9 shows the schematic representation of UV-Vis spectrophotometer.

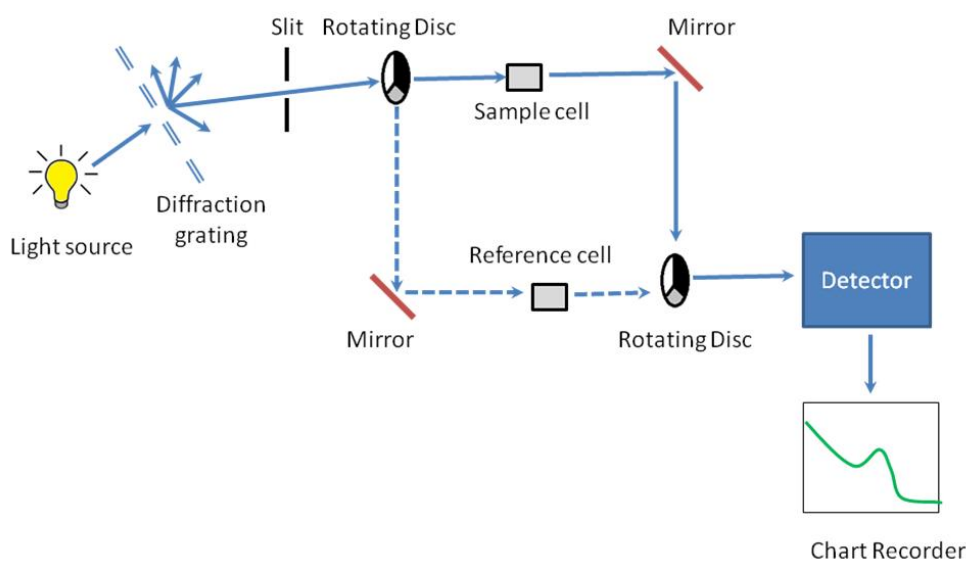


Figure 3.9 Schematic of the UV-Visible spectrophotometer [15].

The light beam passes through the diffraction grating and the slits. The radiation is separated according to its frequency wavelength by a diffraction grating followed by a narrow slit. The slit ensures that the radiation is of a very narrow waveband that is monochromatic. Detection of the radiation passing through the sample or reference cell can be achieved by either a photomultiplier or a photodiode. Single photodiode detectors and photomultiplier tubes are used with scanning monochromator, which filter the light so that only the light of a single

wavelength reaches the detector at one time. The scanning monochromator moves the diffraction grating to step-through each wavelength so that its intensity may be measured as a function of wavelength. The absorption data from the UV-Vis spectrophotometer can be used to determine the band gap energy (E_g) of the material. The band gap energy is determined by using Tauc's relation. Band gap indicates the difference in energy between the top of the valence band filled with electrons and the bottom of the conduction band devoid of electrons [16]. The following relational expression proposed by Tauc, Davis, and Mott is used.

$$h\nu\alpha = A (h\nu - E_g)^{\frac{1}{n}} \quad (3.5)$$

where h : Planck's constant, ν : frequency of vibration, α : absorption coefficient, A : proportional constant, and E_g band gap energy. The value of the exponent n denotes the nature of the sample transition.

For direct allowed transition $n = -$

For direct forbidden transition $n = -$

For indirect allowed transition $n = 2$

For indirect forbidden transition $n = 3$

Since the materials analyzed in this study has a direct transition, $n = -$ was used. When

$\alpha = 0$, this means that

$$E_g = h\nu \quad (3.6)$$

E_g is estimated by extrapolating a tangent line through the plot of α^{-n} against $h\nu$. The analysis was performed within a scan range of 800-200 nm, with a data interval of 1.00 nm at scan speed of 266.75 nm/min. Figure 3.10 below shows the Perkin Elmer Lambda 950 UV-VIS spectrometer used during the absorption measurements.



Figure 3.10 Perkin Elmer Lambda 950 UV-VIS spectrometer.

3.6 Luminescence spectroscopy

Luminescence is emission of optical radiation in the ultraviolet, visible or infrared region of the electromagnetic spectrum and spectroscopy is the study of interaction between radiation and matter. Luminescence occurs in a variety of matter and under many different circumstances. Thus in atoms, polymer, inorganic, organic and organo metallic molecules, organic and inorganic crystals, and amorphous substances all emit luminescence under appropriate conditions [17]. The types of luminescence spectroscopes used in these studies are photoluminescence (PL) and thermoluminescence (TL).

3.6.1 Photoluminescence spectroscopy

PL spectroscopy is a technique used to analyze the luminescence of a material and dynamic processes occurring within a material [18]. Light is directed onto a sample, where it is absorbed and imparts excess energy into the material in a process is called photo-excitation. One way this excess energy can be dissipated by the sample is through the emission of light or luminescence [19]. The excitation source (Xenon lamp) supplies excitation energy to the sample, emitted luminescence is dispersed in a spectral device, a detector converts the optical signal into electric signal that is then processed by electronic devices and finally by a control

computer. The output of the emission spectrum is the plot of luminescence intensity versus emission wavelength. Figure 3.10 shows an outline of the process taking place in the Cary Eclipse spectrophotometer used in this study during the photoluminescence measurements. The technique consists of light source (xenon lamp) which produces photons. The photons pass through the monochromator that only select the certain wavelength to pass through to the sample cell. Luminescence given off is detected by and processed by the electric device. A photograph of the Varian Cary Eclipse Spectrometer is shown in figure 3.12.

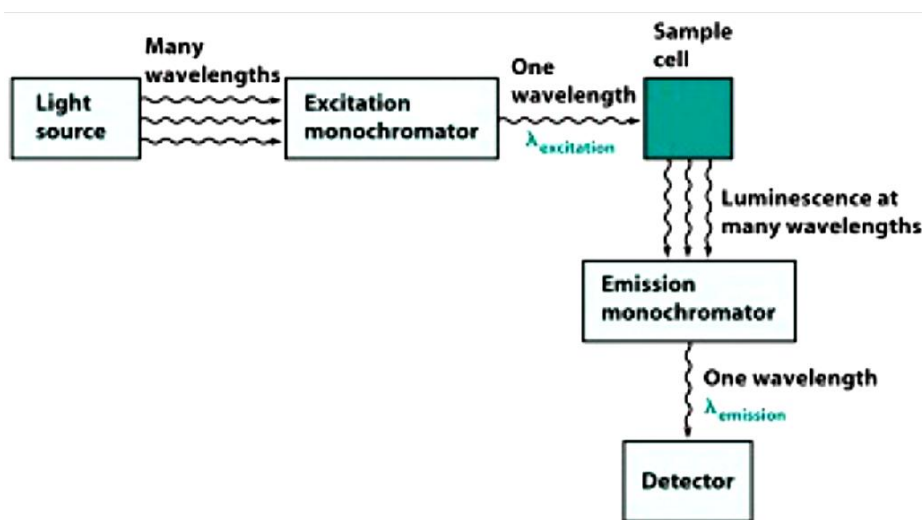


Figure 3.11 Outline presentation of photoluminescence spectroscopy [20].



Figure 3.12 Varian Cary-Eclipse fluorescent spectroscopy.

3.6.2 Thermoluminescence spectroscopy

Thermoluminescence is the phenomenon of emission of light from a solid which has been previously exposed to ionizing radiation (α - rays, β - rays, γ - rays, UV rays and X-rays) under conditions of increasing temperature. The energy stored in the form of the trapped electrons, is released by raising the temperature of the material, and released energy is converted to luminescence [21]. In order for thermoluminescence to occur the material is firstly exposed to radiation. The radiation is a source of energy, whereas the heating is used to help release the absorbed energy. When a solid is irradiated, electrons and holes are created, and electron or holes can be trapped at defect sites. During the heating, these trapped electrons/holes get enough energy to escape from the trap to the conduction band (or valence band). They can be re-trapped again or may recombine with trapped holes/electrons. The site of recombination is called recombination center. If the recombination is radiative, then the center is called luminescence center. The electron trapping process is shown in figure 3.13.

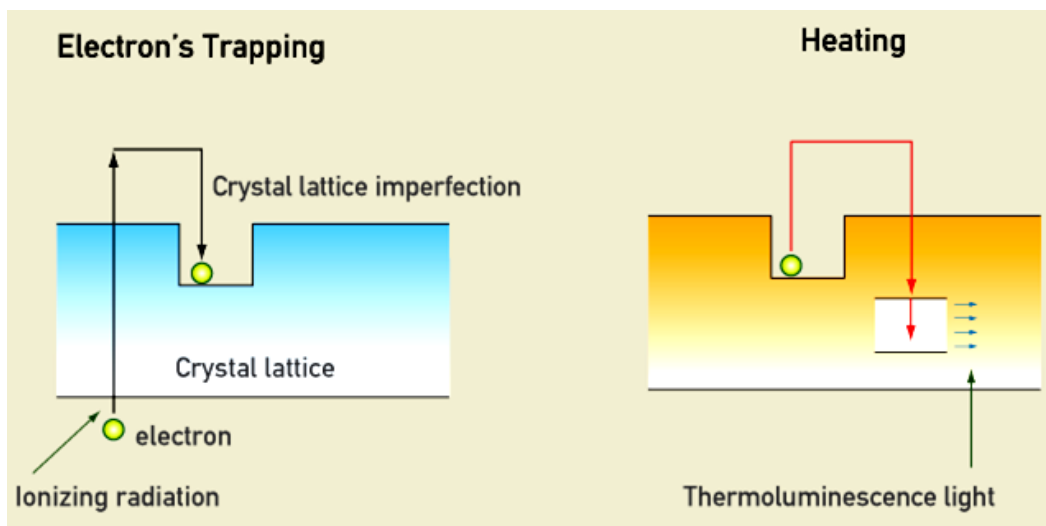


Figure 3.13 The outline of electron trapping [22].

A plot of intensity of emitted light versus the temperature is known as a TL glow curve. The plot may exhibit one or many peaks depending on the number of electrons/holes traps with different trap depths, present in the lattice. The TL glow curve gives information about the luminescent centers present in the material.

Figure 3.14 show the Riso TL/OSL reader model DA-20 used during the measurements. The technique was operated using β irradiation source, at heating rate of 5.00 °C/s with temperature ranging from 100 to 500 °C.



Figure 3.14 Riso TL/OSL reader model DA-20 [23].

3.7 Time-of-Flight Secondary Ion Mass Spectrometry

TOF-SIMS is an analytical technique capable of identifying chemical composition of a sample by measuring its molecular weight. It is also used as a surface-sensitive analytical method that uses a pulsed ion beam to remove molecules from the very outermost surface of the sample. Particles removed from the atomic monolayer on the surface are then accelerated into a flight tube and their masses are determined by measuring the exact time at which they reach the detector. This spectrometer is identified by using pulsed primary ion beam. The ions are formed from continuous beam by a pulsing unit and can be compressed in time by electro-dynamic fields.

When a high energy ion beam collides with a solid surface, energy is transferred from the primary particle to the atoms of the material to be analyzed. The pulsed beam is focused to a small spot to analyze a small area of interest and can be rastered to determine the lateral distribution of elements and molecules (this is known as imaging SIMS). Some of the primary ions can be back scattered but most of them transfer their kinetic energy to the lattice

through a collision sequence and are implemented into the target according to their energy, mass, and impact angle. The ions travel through a tube to arrive at ion detection and counting system. They all depart from the sample at the same time with the same accelerating voltage, but the lighter ions arrive at the detection system before the heavier ones. Surface spectroscopy, surface imaging and depth profiling can be carried out by TOF-SIMS. Figure 3.15 shows the schematic presentation of TOF-SIMS.

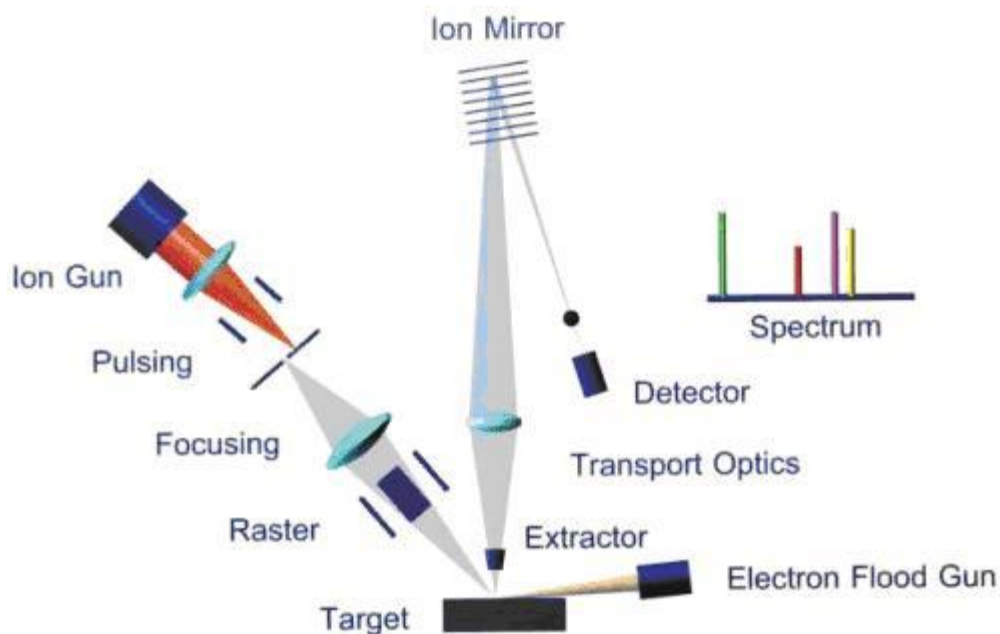


Figure 3.15 Schematic diagram of TOF-SIMS instrument [24].

A reflection-based high resolution TOF-SIMS instrument equipped with a primary ion source and a low-energy pulsed electron source (20 eV) for charge compensation was used to analyze the chemical composition and distribution of dopant ions in our materials. The surface imaging was performed with a Bi⁺ 0.3 pA primary beam, and was rastered over an area of 100 × 100 μm on the sample surface. The instrument used is shown in figure 3.16 below.



Figure 3.16 ION-TOF.SIMS 5.

References

- [1] http://serc.carleton.edu/research_education/geochemsheets/techniques/XRD.html [accessed July 2013]
- [2] http://webs.mn.catholic.edu.au/physics/emery/hsc_ideas_implementation.htm [accessed November 2013]
- [3] <http://hyperphysics.phy-astr.gsu.edu/hbase/quantum/bragg.html> [accessed November 2013]
- [4] <http://www.labexpert.co.th/xrd.html>[accessed November 2013]
- [5] http://en.wikipedia.org/wiki/X-ray_photoelectron_spectroscopy [accessed February 2013]
- [6] H. Sezen, S. Suzer, *Thin Solid Films*, **534** (2013), 1-11
- [7] <http://www.phis.com/surface-analysis-products/versaprobe/overview.html> [accessed December 2013]
- [8] https://en.wikipedia.org/wiki/Electron_microscope [July 2013]
- [9] http://en.wikipedia.org/wiki/Scanning_electron_microscope [accessed July 2013]
- [10] <http://mee-inc.com/sem.html> [accessed July 2013]
- [11] <http://www.purdue.edu/rem/rs/sem.htm> [December 2012]
- [12] <http://www.understanding-cement.com/sem-introduction.html> [accessed July 2013]
- [13] http://www.hk-phy.org/atomic_world/tem/tem02_e.html [accessed October 2013]
- [14] <http://le-csss.asu.edu/ARM200F> [accessed December 2013]
- [15] <http://cnx.org/content/m34601/latest/> [accessed October 2013]
- [16] <http://imtuoradea.ro/bioethanol/UV.VIS.theory.pdf> [December 2013]
- [17] <http://www2.shimadzu.com/applications/UV/VIS/A428E.pdf> [October 2013]

- [18] G. Blasse, B.C. Grabmair, *Luminescent materials*, Springer-Verlag, (1994)
- [19] G.D. Gilliland, *Mate. Sci. Eng*, 1997, **R18**, 99-400
- [20] R. Ye, R.A. Barron, *Photoluminescence Spectroscopy and its Applications*, Connexions Web site. [Http://cnx.org/content/m38357/1.2/](http://cnx.org/content/m38357/1.2/), Jun 6, 2011.
- [21] K. Van den Eeckhout, A.J.J. Bos, D. Poelman, P. Smet, *Physics Review B*, 2013, **87**, 045126-1-11
- [22] <http://www.webexhibits.org/pigments/intro/dating.html> [October 2013]
- [23] http://www.nutech.dtu.dk/english/About-DTU-Nutech/Radiation_physics/Products/TL_OSL_reader [accessed December 2013]
- [24] http://serc.carleton.edu/research_education/geochemsheets/techniques/ToF-SIMS.html [accessed December 2013]

Chapter 4: Synthesis Techniques

4.1 Introduction

In this chapter a brief description of the experimental techniques used to synthesize phosphate phosphors is presented. These techniques are co-precipitation, urea and citric-gel combustion, and microwave-assisted method.

4.2 Co-precipitation method

Co-precipitation method is a synthesis technique that yields precipitation of desired compound by reaction type of acid+base→salt [1]. This method is ideally used to produce fine, chemically homogenous, and pure or single phase powders. It requires control of the concentration of the solution, pH, temperature and stirring speed in order to obtain the final product with required properties. This procedure is attractive because of its capacity to yield products at low temperatures in the range of only 80-120 °C.

Advantages

- Homogenous mixing of reactants.
- Simple direct process for the synthesis of fine metal oxide powders, which are highly reactive in low temperature sintering.

Disadvantages

- This process is not suitable for the preparation of high pure and accurate stoichiometric phase.
- It is not having universal experimental condition for synthesis of various types of metal oxide.
- This method does not work well, if the reactants have very different solubility as well as different precipitate rate.

The schematic diagram and the snapshots of the procedure followed for the preparation of $\text{Ca}_5(\text{PO}_4)_3\text{OH}:\text{Gd}^{3+},\text{Pr}^{3+}$ by co-precipitation method are presented in figure 4.1 and figure 4.2 respectively. Steps 1 – 6 include (1) Mixing and stirring of precursors, (2) Adding precursors together and stirring for 12 hours, (3) washing by using distilled water and ethanol, and separating by centrifugation, (4) Drying in an oven at 80 °C for 24 hours, (5) grinding, and (6) Calcining at different temperatures.

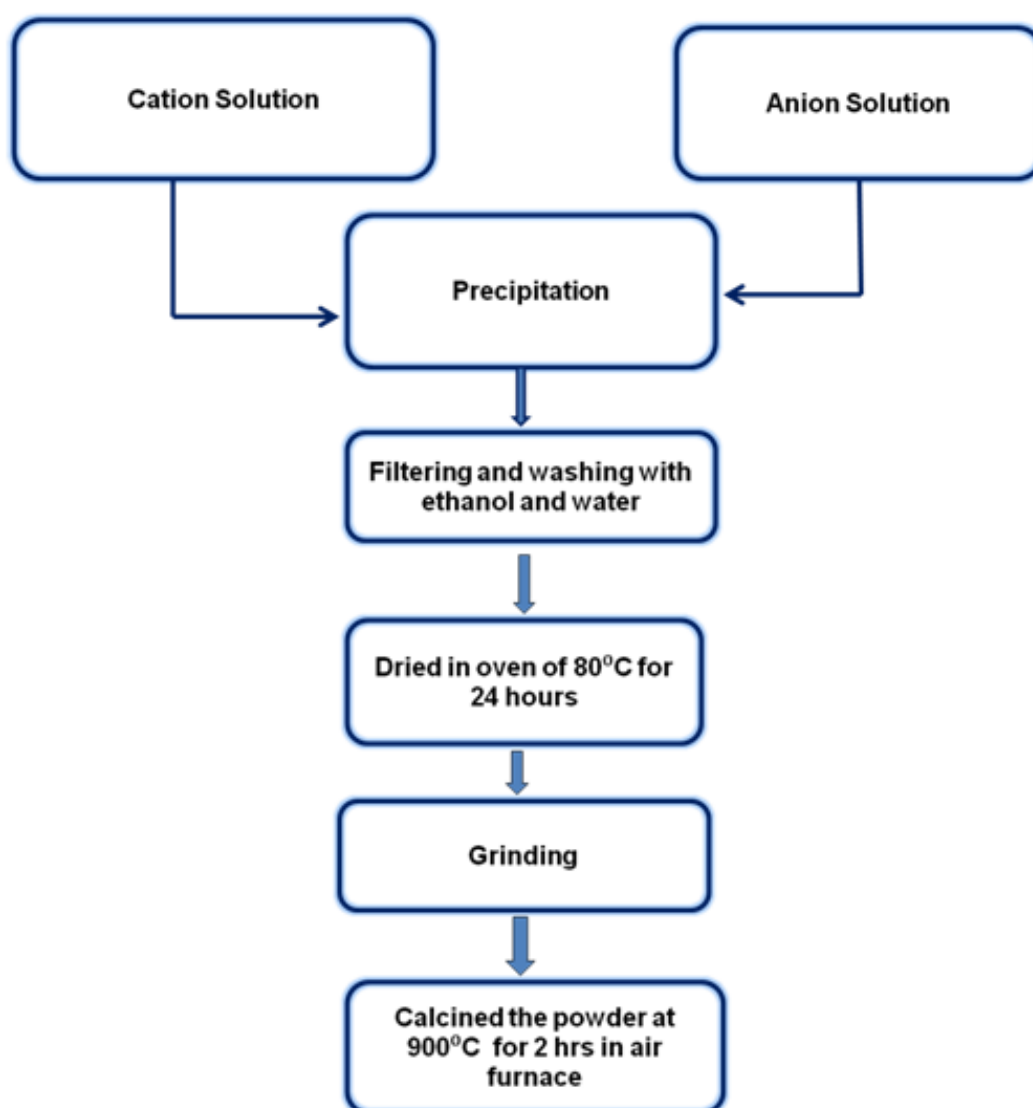


Figure 4.1 Flow-chart of co-precipitation method.

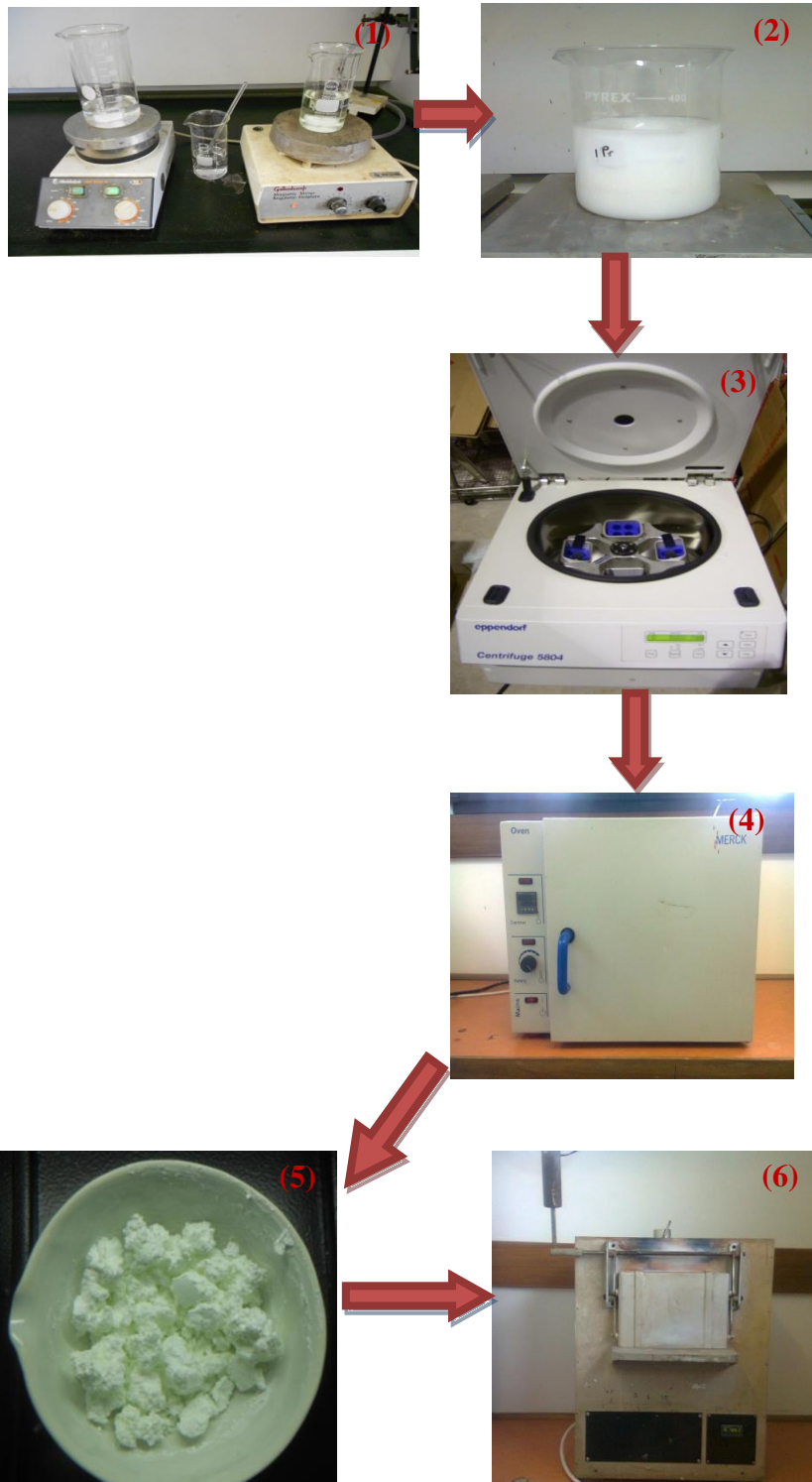


Figure 4.2 Preparation method of $\text{Ca}_5(\text{PO}_4)_3\text{OH}:\text{Gd}^{3+}, \text{Pr}^{3+}$ nanophosphor by co-precipitation method.

4.3 Combustion method

Combustion is a complex sequence of chemical reactions between a fuel and an oxidant accompanied by the production of heat or both heat and light in the form of either a glow or flame. For combustion to occur, fuel and oxidizer are required as reactants, i.e., the substances present before the reaction can take place. When the mixture of fuel and oxidizer is ignited, combustion takes place. During the combustion process, large volume of gases will evolve which prevent the agglomeration and lead to the formation of fine powders with nano structures [4]. Release of heat during the combustion reaction depends on the fuel-oxidant stoichiometry in the precursor composition [5]. For the combustion synthesis of oxides, metal nitrates are used as oxidizer, and fuels used are hydrazine-based compounds, citric acid, or urea.

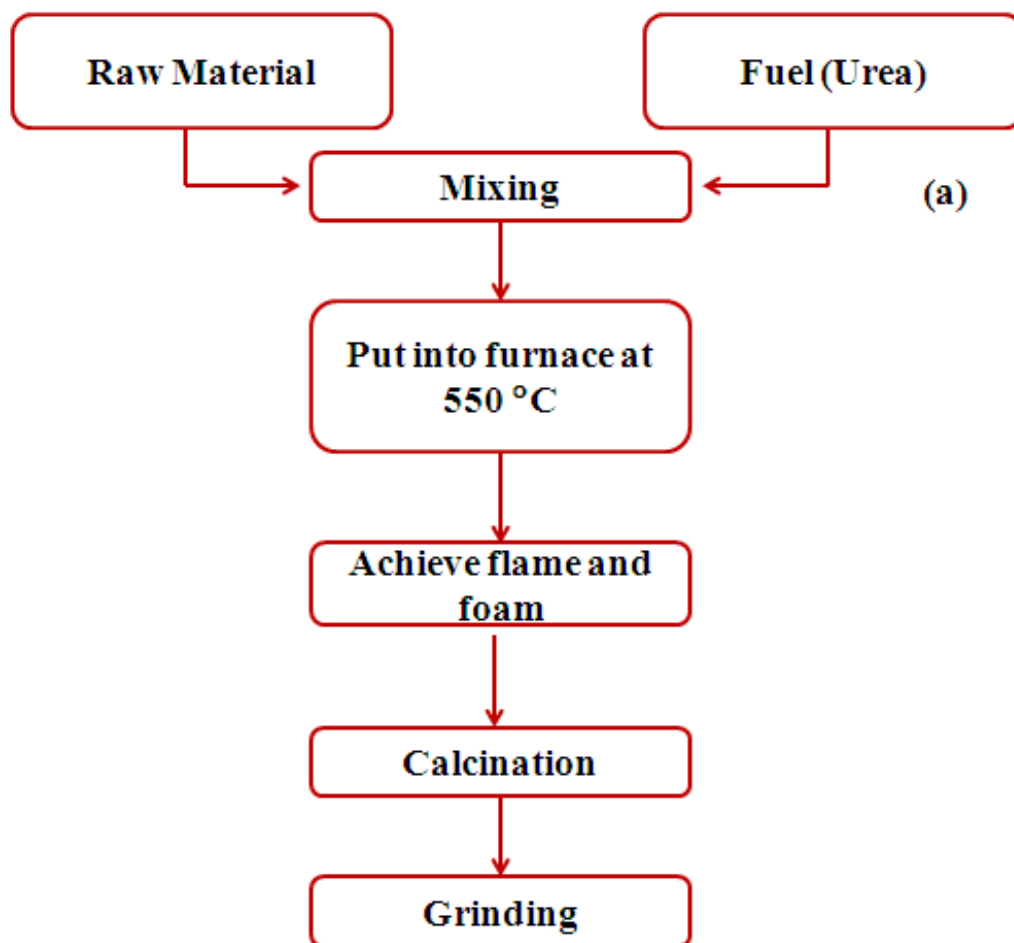
Advantages

- Low cost and low temperature processing when compared to traditional solid state reaction.
- Better control of stoichiometry.
- Crystalline size of the final oxide products produced by this method is invariably in the nanometer range.
- Exothermic reaction makes product almost instantaneously
- Possibility of multicomponent oxides with single phase and high surface area.
- Large number of gas evolved during combustion results in a porous product in which the agglomerates formed are so weak that they can be easily crushed and ground into a fine powder.

Disadvantages

- Contamination due to carbonaceous residue, particle agglomeration, poor control on particle morphology.
- Understanding of combustion behavior is needed to perform the controlled combustion in order to get final products with desired properties.
- Possibility of violent combustion reaction, which needs special production.

The flow chart for the preparation of calcium phosphate by urea and citric-gel combustion is presented in figure 4.2, figure 4.3 respectively and the snapshots in figure 4.5. Steps 1 – 3 include (1) Mixing and stirring of precursors, (2) The solution was fired in the furnace, combustion ashes were cooled to room temperature, (3) grounded gently using a pestle and mortar resulting in a fine powder (4) Calcining at different temperatures.



4.3 Flow-chart of $\text{Ca}_3(\text{PO}_4)_2:\text{Gd}^{3+},\text{Pr}^{3+}$ prepared by urea combustion method.

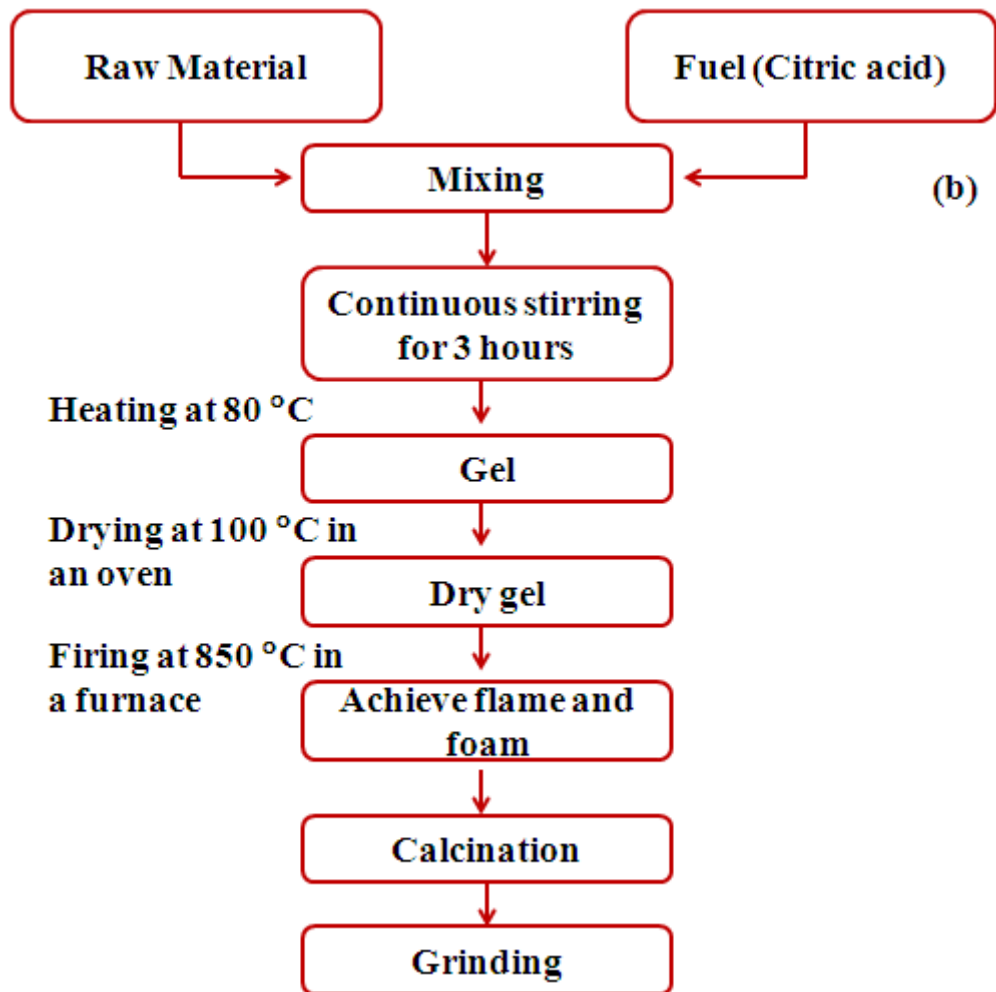


Figure 4.4 Flow-chart of $\text{Ca}_5(\text{PO}_4)_3\text{OH}:\text{Gd}^{3+},\text{Pr}^{3+}$ citrate-gel combustion method.



Figure 4.5 snapshots of phosphor powders prepared by urea and citrate-gel combustion methods.

4.4 Microwave assisted synthesis method

Microwave synthesis is the science of applying microwave radiation to chemical reactions. Microwave act as a high frequency electric fields and will generally heat any material containing mobile electric charges, such as polar molecules in a solvent or conducting ions in a solid. The technique offers simple, clean, fast, efficient, and economic synthesis of a large number of organic molecules. Samples are heated quickly and uniformly, because microwave energy is immediately absorbed by the samples. Recently, microwave synthesis has been extensively used for carrying out chemicals reactions and has become a useful non-conventional energy source for performing organic synthesis [6]. The temperature of the samples are monitored with an optical pyrometer and controlled by adjusting the input power. During the process, the samples are rotating horizontally. The samples are heated up to 150 °C for 1 hour and cooled down to room temperature. The basic principle in the microwave assisted synthesis is the interaction of charged particle of the material with electromagnetic wavelength of particular frequency. The phenomena of producing heat by electromagnetic irradiation are either by collision or conduction, some time by both. Microwave enhancement of chemicals only takes place during applications of the microwave energy. Microwave irradiation is not only applicable to the solvent phase chemistry, but also to the solid-state organic synthesis. Figure 4.6 shows the schematic procedure followed during the preparation of phosphor material by microwave assisted method.

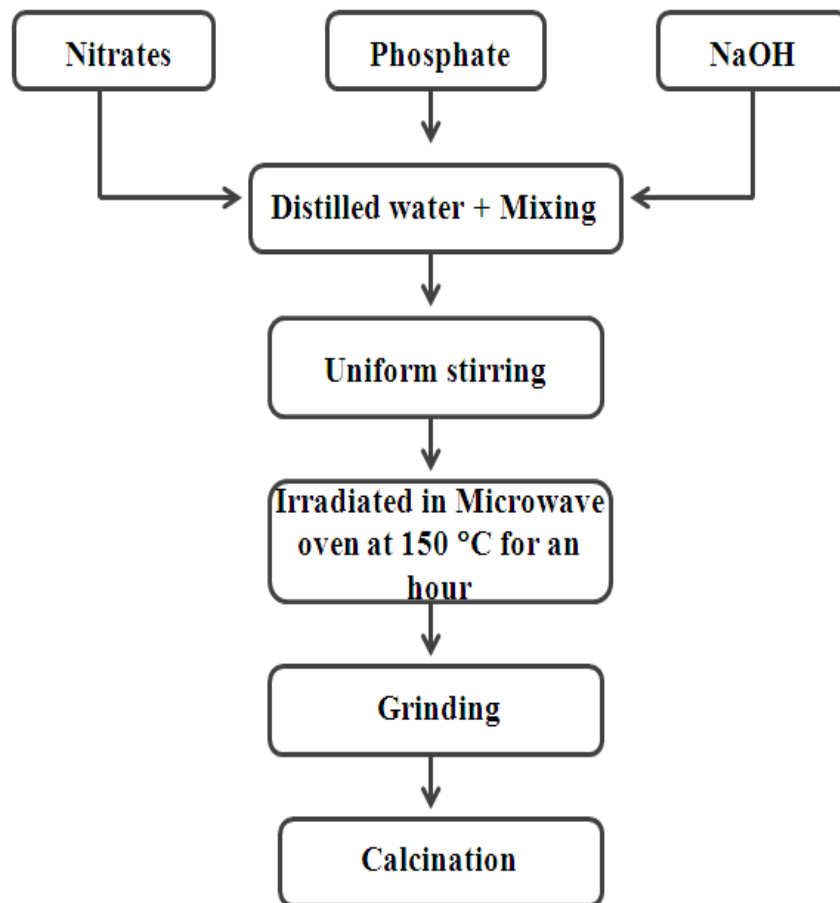
Advantages of Microwave-assisted Method

- Highly accelerated rate of the reaction,
- Reaction temperature can be monitored and controlled,
- High energy efficiency
- Improved yield
- Less side-products
- Wider usable range of temperature
- High purity of products

- Synthesis of new material [1].

Disadvantages Microwave-assisted Method

- Heat force control is difficult
- Water evaporation
- Closed container is dangerous because it could burst



4.6 Flow-chart of $\text{Ca}_3(\text{PO}_4)_2:\text{Gd}^{3+},\text{Pr}^{3+}$ phosphor prepared by microwave-assisted method

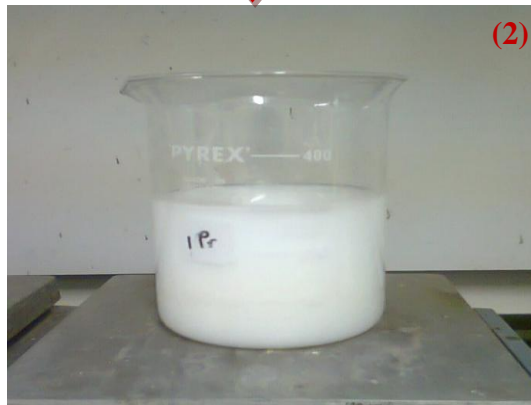


Figure 4.7 snapshots of preparation of $\text{Ca}_3(\text{PO}_4)_2:\text{Gd}^{3+},\text{Pr}^{3+}$ by microwave-assisted method.

References

- [1] K.N. Shinde, S.J. Dhoble, H.C. Swart, K. Park, 2012, *Phosphate Phosphors for Solid-State Lighting*, New York, Springer.
- [2] D.M. Liu, T. Troczynski, W.J. Tseng, *Biomaterials*, 2001, **22**, 1721–1730.
- [3] G.C. Koumoulidis, A.P. Katsoulidis, A.K. Ladavos, P.J. Pomonis, C.C. Trapalis, A.T. Sdoukos, T.C. Vaimukis, *J. Colloid. Interface Sci.*, 2003, **259**, 253–260.
- [4] http://shodhganga.inflibnet.ac.in/bitstream/10603/5252/9/09_chapter%202.pdf [accessed October 2013]
- [5] J. Schafer, W. Sigmund, S. Roy, F. Aldinger, *J. Mater. Res.*, 1997, **12**, 2518-2521.
- [6] A.S. Madhvi, J. Smita, K.R. Desai, *Arch. Appl. Sci. Res.*, 2012, **4**, 645-661.

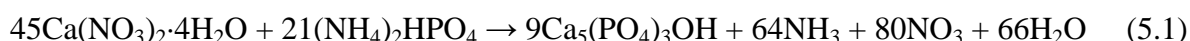
Chapter 5: Luminescent properties of $\text{Ca}_5(\text{PO}_4)_3\text{OH}:\text{Gd}^{3+},\text{Pr}^{3+}$ phosphor powder prepared by Co-precipitation method

5.1 Introduction

Halophosphates are apatite mineral structure that can be represented by a general formula $\text{Ca}_5(\text{PO}_4)_3\text{X}$ ($\text{X} = \text{F}, \text{Cl}$ or OH). In modern age research, these minerals are doped with either rare-earth or alkali earth ions to prepare phosphor materials that can be used different types of light emitting devices. In this study, hydroxyapatite or $(\text{Ca}_5(\text{PO}_4)_3\text{OH})$ was co-doped with gadolinium (Gd^{3+}) and praseodymium (Pr^{3+}) to prepare a nanocrystalline phosphor that emits in the UVB region, and the phosphor was investigated for application in phototherapy lamp. The phosphor display strong ultraviolet absorption and a subsequent narrow line emission at 313 nm due to the $f-f$ transitions of Gd^{3+} . This emission was improved by Pr^{3+} co-doping. This chapter reports on the preparation, structure, morphology, chemical composition, electronic states, ionic distribution and photoluminescence properties of $\text{Ca}_5(\text{PO}_4)_3\text{OH}:\text{Gd}^{3+},\text{Pr}^{3+}$.

5.2 Experimental

Calcium nitrate tetrahydrate, diammonium hydrogen phosphate, sodium hydroxide gadolinium nitrate pentahydrate and praseodymium nitrate hexahydrate were used as starting materials. The materials were mixed stoichiometrically according to the following reaction equation:



In a typical preparation, 100 ml of 0.4M $(\text{NH}_4)_2\text{HPO}_4$ (pH = 6.5), 100 ml of 0.1M (NaOH) (pH = 13.5), and 100 ml of 0.6M $(\text{Ca}(\text{NO}_3)_2 \cdot 4\text{H}_2\text{O})$, 2M $\text{Pr}(\text{NO}_3)_3 \cdot 6\text{H}_2\text{O}$ and 10M $\text{Gd}(\text{NO}_3)_3 \cdot 6\text{H}_2\text{O}$ (pH = 7.3) solutions were prepared separately, and were later combined and

stirred vigorously at room temperature. The pH of the system was maintained at 6.5. After adding 0.1M NaOH the pH increased to 10.8 and the stirring was continued for 12 hours until a white precipitate was formed. The precipitate was separated by centrifugation and was dried at 80 °C for 24 hours. The dried powder was ground by using a mortar and pestle and was calcined at 900 °C for 2 hours. $\text{Ca}_5(\text{PO}_4)_3\text{OH}:\text{Gd}^{3+},\text{Pr}^{3+}$ powders with different concentrations of Gd^{3+} and Pr^{3+} were prepared. The concentrations of Gd^{3+} and Pr^{3+} in the single doped systems were varied from 1-11 mol% and 0.5–5 mol% respectively while in the co-doped systems different ratios of Gd^{3+} to Pr^{3+} were used.

The structure and crystallinity of the phosphors were analysed using XRD. The morphology of the materials was analysed using SEM and HRTEM. The chemical composition was examined using EDS and XPS. The XPS was also used to analyse the electronic state of the powder. Photoluminescent data were recorded at room temperature using Cary Eclipse fluorescence with monochromatized xenon lamp used as an excitation source at excitation wavelength ranging from 200-600 nm.

5.3 Results and Discussion

Figure 5.1 (a) shows the XRD pattern of the un-doped $\text{Ca}_5(\text{PO}_4)_3\text{OH}$ powder annealed at 900 °C in air. The pattern is consistent with the hexagonal structure of $\text{Ca}_5(\text{PO}_4)_3\text{OH}$ referenced in JCPDS Card Number 73-0293. Figure 5.1 (b) shows the XRD pattern of the un-doped $\text{Ca}_5(\text{PO}_4)_3\text{OH}$ powder for as-prepared (unannealed) and annealed at different temperatures (600 – 1000 °C in air). The diffraction patterns became sharper and more pronounced with increasing annealing temperature indicating improvement in crystallinity of the phosphor powder. The crystal size was estimated by using Scherrer equation. The strongest peaks that were used to calculate crystallite size were ($2\theta = 25.95^\circ, 31.89^\circ, 46.77^\circ, \text{ and } 49.55^\circ$). The crystallite size estimated was in the range of ~22 - 65 nm from as-prepared to 1000 °C. Figure 5.1 (c) shows the plot of the FWHM vs annealing temperature of $\text{Ca}_5(\text{PO}_4)_3\text{OH}:\text{Gd}^{3+},\text{Pr}^{3+}$ phosphor powder calcined from 600 °C to 1000 °C. The FWHM peak at (211) plane was decreasing with an increase in annealing temperature and this further confirms the improvement in crystallinity of the powder. Generally, hydroxyapatite compounds have hexagonal structures with a space group $\text{P6}_3/\text{m}$ and unit cell parameters of a

= 9.43 Å and $c = 6.88$ Å. The unit cell contains a complete representation of the hydroxylapatite crystal. The structure consists of Ca^{2+} , PO_4^{3-} , and OH^- groups closely packed together as shown in figure 5.1 (d). There are two Ca sites present in the unit cell, namely Ca1 and Ca2 [1]. Ca1 with C_3 symmetry is surrounded by nine oxygen atoms while Ca2 with C_s symmetry is coordinated to six oxygen atoms and one OH^- group [2]. The P^{5+} is surrounded by O^{2-} ions in the tetrahedral arrangements. Each tetrahedron contains oxygen atoms referred to as O1, O2, and O3. XRD crystallography data of $\text{Ca}_5(\text{PO}_4)_3(\text{OH})\text{:Gd}^{3+},\text{Pr}^{3+}$ lattices calculated using equation 5.2 are listed in Table 5.1. The experimental values of d-spacing were calculated by using the following equation:

$$d_{hkl} = [-(h^2 + hk + k^2) + -]^{-1/2} \quad (5.2)$$

The d-spacings values compare reasonably well with theoretical values as shown in table 5.2.

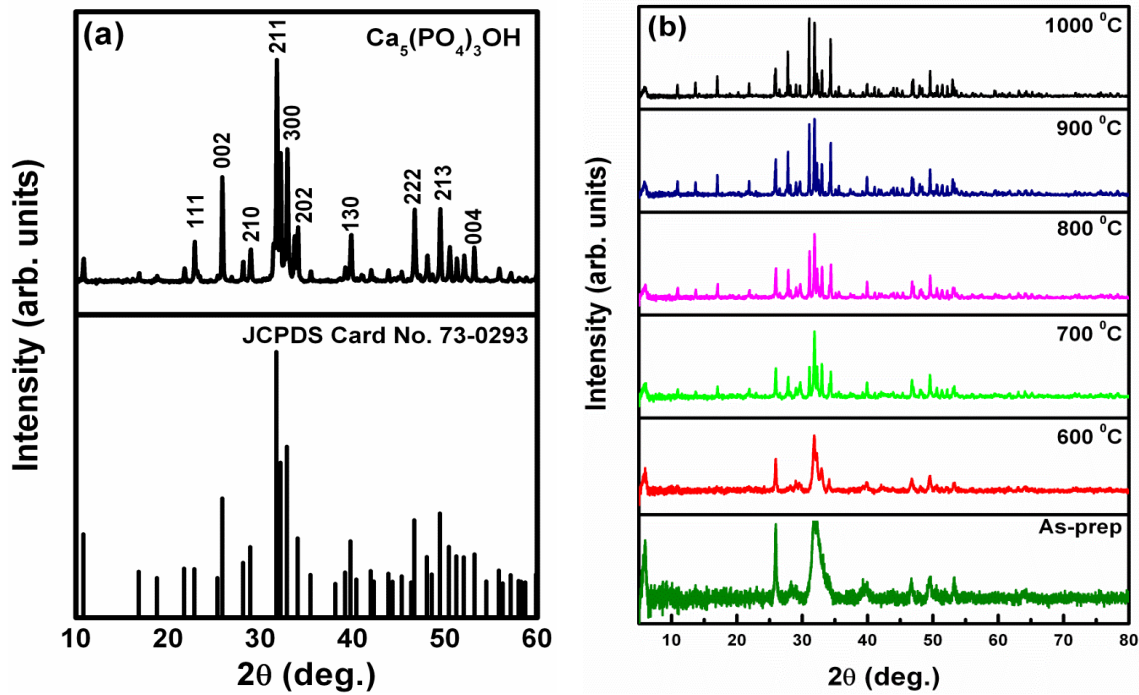


Figure 5.1 (a) XRD patterns of $\text{Ca}_5(\text{PO}_4)_3\text{OH}$ powder and matching JCPDS Card No. 73-0293, and (b) XRD pattern of $\text{Ca}_5(\text{PO}_4)_3\text{OH}\text{:Gd}^{3+},\text{Pr}^{3+}$ calcined at different temperatures.

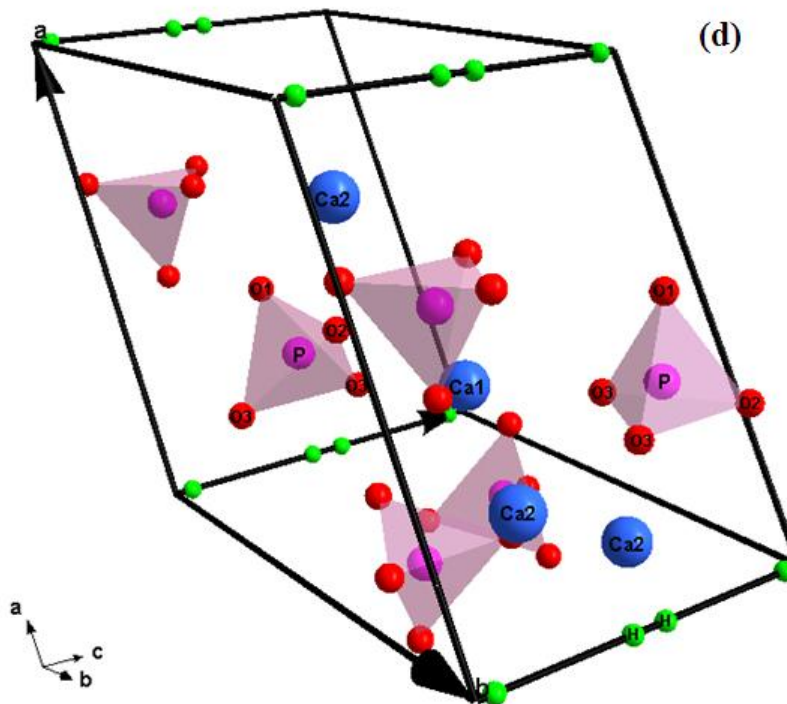
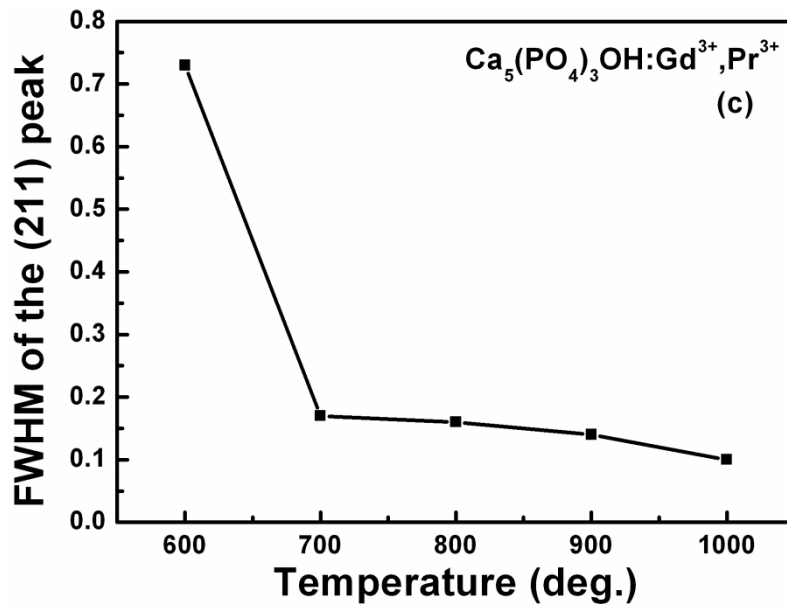


Figure 5.1 (c) FWHM of (211) plane versus different annealing temperatures and (d) Crystal structure of Ca₅(PO₄)₃OH.

Table 5.1 Crystallographic data of $\text{Ca}_5(\text{PO}_4)_3\text{OH}$ lattice

Phase	PentaCalcium hydroxide triphosphate (hydroxyapatite)
Empirical formula	$\text{Ca}_5(\text{PO}_4)_3\text{OH}$
Structure	Hexagonal
Space group	$P6_3/m(176)$
Formal weight	502.31g/mol
Lattice parameter	
a (Å)	9.432
c (Å)	6.861

Table 5.2 h k l planes and d-spacing

h	k	L	Calculated d-spacing(Å)	Theoretical d-spacing(Å)
1	1	0	4.71	4.71
1	0	1	4.41	5.26
2	0	0	4.08	4.08
1	1	1	3.88	3.89
0	0	2	3.43	3.44
1	0	2	3.16	3.17
2	1	0	3.08	3.08
2	1	1	2.81	2.81
1	1	2	2.77	2.77
3	0	0	2.72	2.72
2	0	2	2.62	2.63
2	2	1	2.22	2.30
2	0	3	1.99	1.99
2	3	1	1.80	1.80

Figure 5.2 Shows the XPS survey spectrum (0-1400 eV) of $\text{Ca}_5(\text{PO}_4)_3\text{OH}:\text{Gd}^{3+}, \text{Pr}^{3+}$ phosphor powder. The survey spectrum confirmed presence of calcium, oxygen, phosphorus, gadolinium and a very low signal of praseodymium at different binding energies. The other element such as carbon and sodium were also observed and presence of these elements may be due to precursors used during the preparation process.

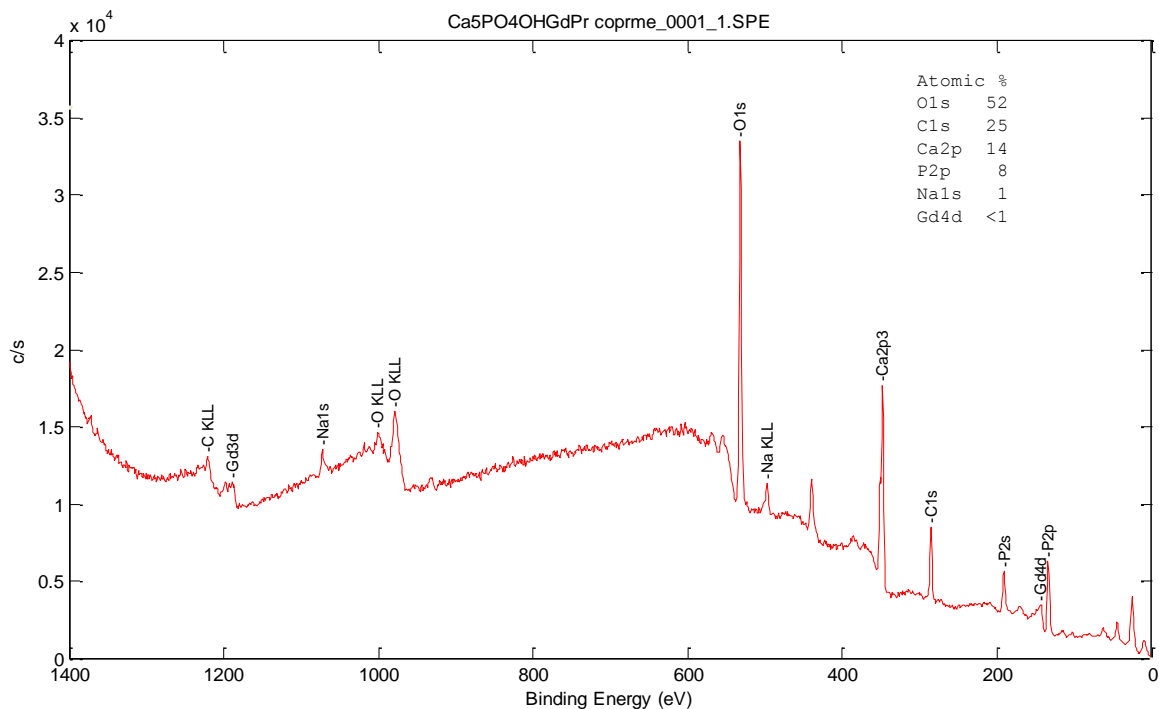


Figure 5.2 XPS survey spectrum of $\text{Ca}_5(\text{PO}_4)_3\text{OH}:\text{Gd}^{3+},\text{Pr}^{3+}$ phosphor powder

Figure 5.3 (a-e) show respectively the fitted Ca 2p, P 2p, O 1s, Gd 3p and Pr 3d high resolution XPS peaks of the $\text{Ca}_5(\text{PO}_4)_3\text{OH}:\text{Gd}^{3+},\text{Pr}^{3+}$ system annealed at 900 °C in air. The Ca 2p spectrum in figure 2(a) consists of two peaks ascribed to the crystal field split components of the $2p_{1/2}$ and $2p_{3/2}$ energy states. These peaks have been deconvoluted into four peaks due to Ca occupying two sites in the hexagonal $\text{Ca}_5(\text{PO}_4)_3\text{OH}$ host. All the peaks at binding energies of 346, 347, 349 and 350 eV are assigned to Ca bonded to O in the O-Ca-O system due to two different environments of Ca with different coordination. Figure 5.3 (b) shows the P 2p XPS peak deconvoluted into two peaks at 133 (P $2p_{3/2}$) and 134 (P $2p_{1/2}$) eV which are due to the crystal field splitting of the P 2p energy state. These peaks are assigned to P tetrahedrally coordinated to O atoms [3, 4]. As shown in figure 5.3 (c), the high resolution O 1s peak was deconvoluted into four peaks sites labelled I1, I2, I3 and I4 corresponding to 530, 531, 533 and 529 eV respectively. These peaks correspond to the O 1s electron binding energies in the various oxygen-containing layers in the sample structure [5]. Oxygen sites labelled I2 and I3 are assigned to P - O (oxygen singly bonded to phosphorus) and O (I1) is assigned to P = O (oxygen doubly bonded to phosphorus). The less intense peak (I4) at 529 eV is assigned to O - H bond. The high resolution spectrum of the Gd 3d

XPS peak is shown in figure 5.3 (d). The figure shows peaks of Gd at $3d_{5/2}$ ($m = 1187$ eV, $s = 1196$ eV and $t = 1198$ eV) and $3d_{3/2}$ ($m' = 1218$ eV, $s' = 1223$ eV and $t' = 1230$ eV) energy states respectively. The peaks are assigned to the 3d-4f transition and the separation between the peaks is due to the spin-orbit splitting of the $3d_{5/2}$ and $3d_{3/2}$ level. The reason for the multiplet feature in each of the peaks is the spin-orbit moment coupling of $3d$ and $4f$ states [6]. The Gd 3d peaks and their satellite structures are in agreement with the multiplet calculation. The data exhibit main and satellite structures as in other trivalent Gd compounds. The positions and the full width at half maximum (FWHM) of the peaks appear to have almost the same values for all rare – earth compounds [7]. Figure 5.3 (e) shows the Pr $3d_{5/2}$ and $3d_{3/2}$ peaks of $\text{Ca}_5(\text{PO}_4)_3\text{OH}:\text{Gd}^{3+}, \text{Pr}^{3+}$ powder phosphor [8]. The complex structure of $3d_{3/2}$ might be due to $4f$ -induced multiplet. The data exhibit $3d_{5/2}$ ($m = 929$ eV and $s = 933$ eV) and $3d_{3/2}$ ($m' = 950$ eV and $s' = 954$ eV) structures. The extra peaks ($t = 934$ and $t' = 958$ eV) at higher binding energies for trivalent Pr compound are due to $3d4f^3$ final state multiplet structure [9, 10].

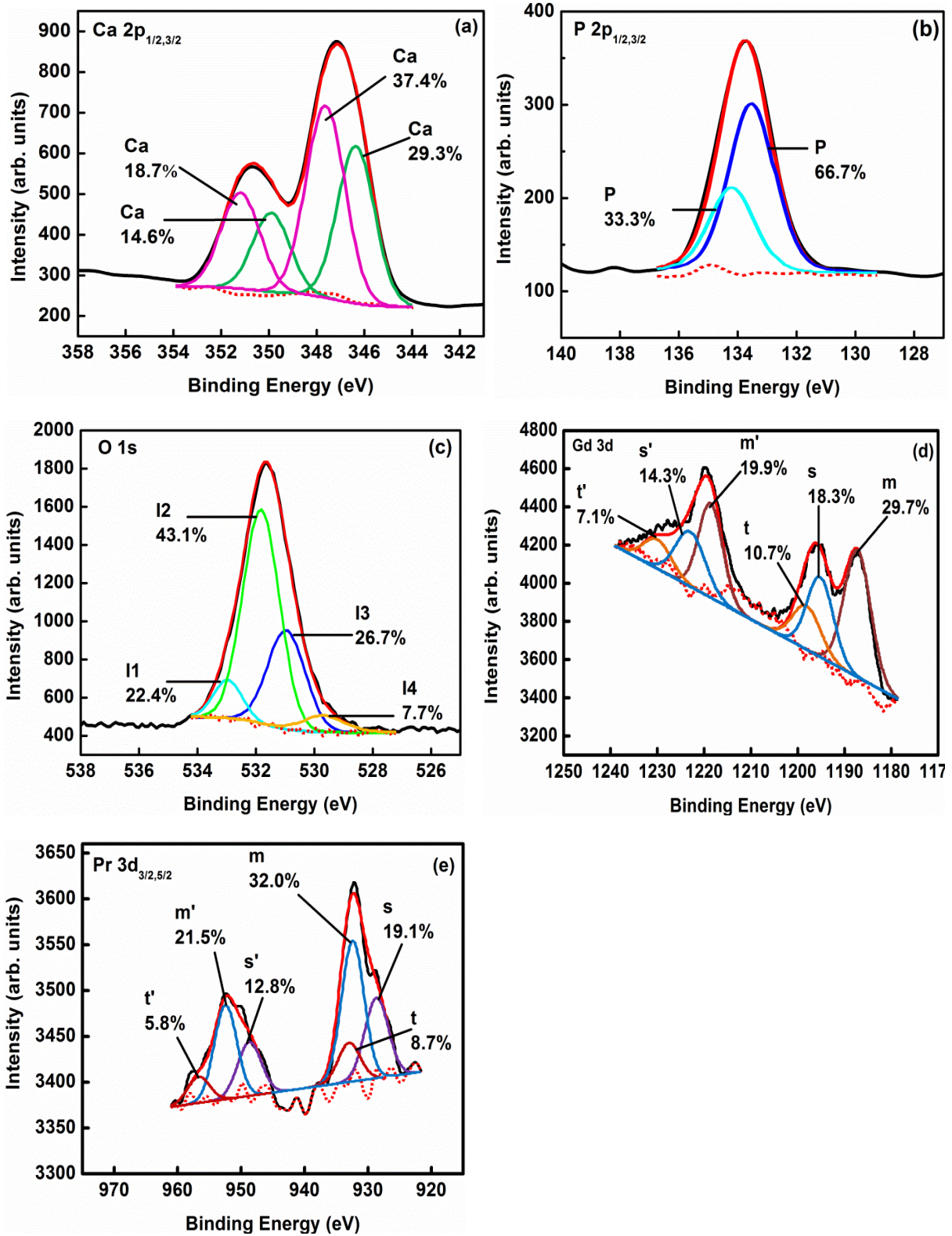


Figure 5.3 (a-e) Deconvoluted Ca (2p), P (2p), O (1s), Gd (3d) and Pr (3d) peaks of $\text{Ca}_5(\text{PO}_4)_3\text{OH}:\text{Gd}^{3+},\text{Pr}^{3+}$ powder phosphor annealed at 900 °C in air.

Figure 5.4 (a) shows the SEM image of $\text{Ca}_5(\text{PO}_4)_3\text{OH}:\text{Gd}^{3+},\text{Pr}^{3+}$ powder with Gd^{3+} and Pr^{3+} concentrations of 10 and 2 mol %, respectively. The image shows that the powder was composed of an agglomeration of spherical particles. All the elements present in the material were detected by EDS as shown in figure 5.4 (b). Figure 5.4 (c) shows the HRTEM image of $\text{Ca}_5(\text{PO}_4)_3\text{OH}:\text{Gd}^{3+},\text{Pr}^{3+}$ showing faceted edges, forming a hexagonal shape. The well defined lattice fringes with a d-spacing of 5.12 Å was estimated from selected area diffraction corresponding to the (101) plane are observed in figure 5.4 (d) confirms crystallinity of the $\text{Ca}_5(\text{PO}_4)_3\text{OH}:\text{Gd}^{3+},\text{Pr}^{3+}$ phosphor particle and this is in consistent with the XRD data. Figure 5.4 (e) shows the selected area electron diffraction (SAED) pattern of the HRTEM image $\text{Ca}_5(\text{PO}_4)_3\text{OH}:\text{Gd}^{3+},\text{Pr}^{3+}$ phosphor. The pattern confirm the hexagonal close-packed phase in the (101) plane on the direction of the beam.

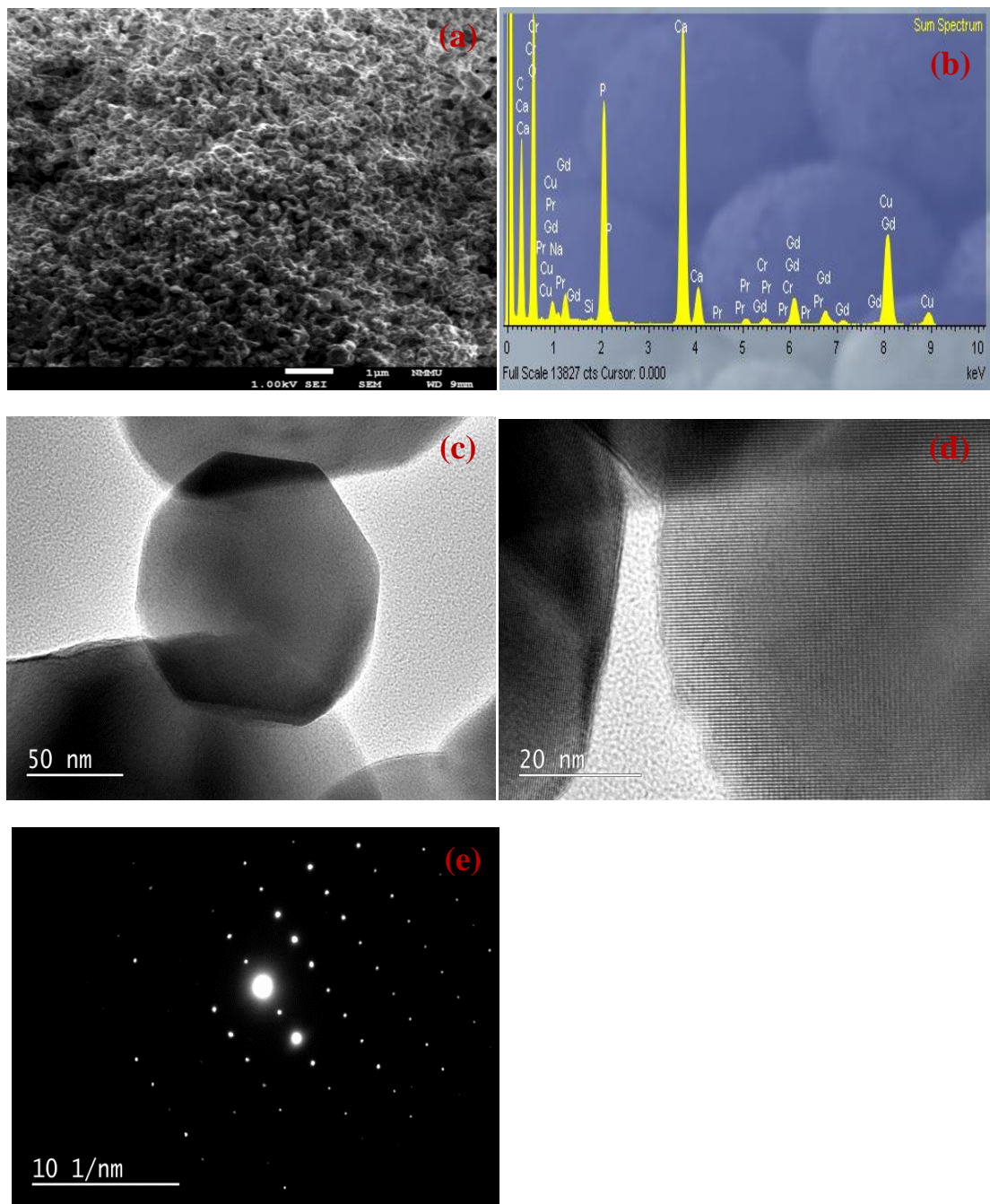


Figure 5.4 (a) SEM images, (b) EDS spectrum, (c) HRTEM images, (d) lattice fringes and (e) selected area electron diffraction pattern of the HRTEM image of $\text{Ca}_5(\text{PO}_4)_3\text{OH}:\text{Gd}^{3+}, \text{Pr}^{3+}$ phosphor powders.

In order to identify the presence of dopants and homogeneity of doping in the crystal lattice, TOF-SIMS analysis was conducted. Figure 5.5 shows the TOF-SIMS spectra of

$\text{Ca}_5(\text{PO}_4)_3\text{OH}:\text{Gd}^{3+},\text{Pr}^{3+}$ phosphor powder. Secondary electrons emitted from the sample surface were used to count the number of incident primary ions in the SIMS analysis. The spectra in the figure are plot of intensity versus secondary ion (SI) mass. Figures 5.5 (a-e) show respectively the positive and negative ion mass spectra of $\text{Ca}_5(\text{PO}_4)_3\text{OH}:\text{Gd}^{3+},\text{Pr}^{3+}$. For positive polarity mode, the peaks were detected at $m/z = 39.96$, 140.87 , and 156 corresponding to Ca^{2+} , Pr^{3+} , and Gd^{3+} respectively. For negative polarity mode, the peaks were detected at $m/z = 30.94$ and 16.00 and corresponding to P^{3-} and O^{2-} ions respectively.

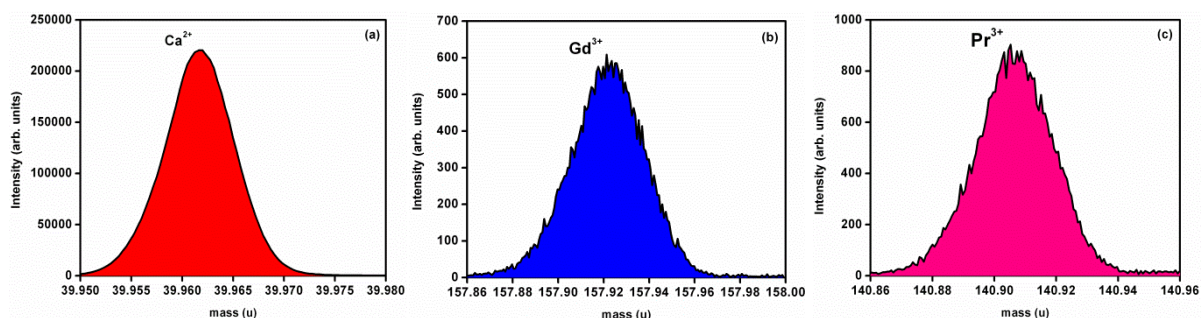


Figure 5.5 (a-c) Positive TOF-SIMS spectra of $\text{Ca}_5(\text{PO}_4)_3\text{OH}:\text{Gd}^{3+},\text{Pr}^{3+}$ showing Ca^{2+} , Gd^{3+} , and Pr^{3+} peaks.

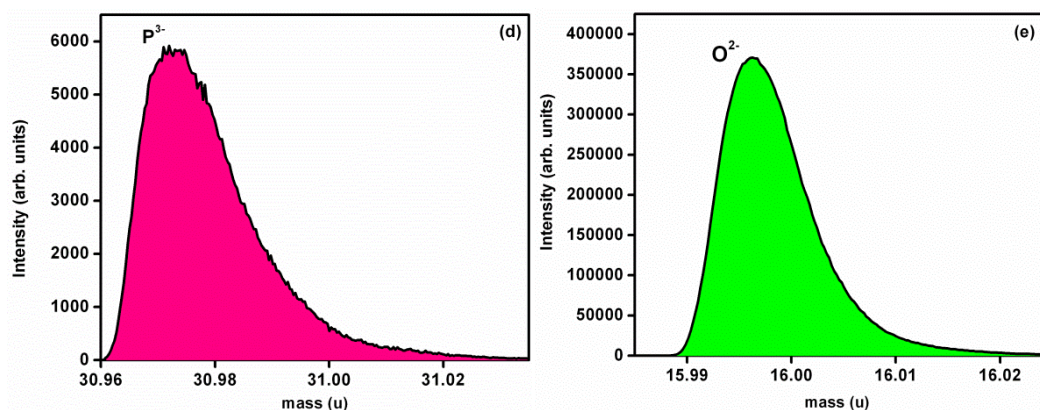


Figure 5.5 (d-e) Negative TOF-SIMS spectra of $\text{Ca}_5(\text{PO}_4)_3\text{OH}:\text{Gd}^{3+},\text{Pr}^{3+}$ showing P^{3-} and O^{2-} peaks.

Figure 5.6 presents the TOF-SIMS images showing the distribution of different ions the $\text{Ca}_5(\text{PO}_4)_3\text{OH}:\text{Gd}^{3+},\text{Pr}^{3+}$ powder phosphor. Images were collected in both positive and negative ion modes. All individual images are represented in a linear colour scale bar with the colours ranging from black – red - orange - yellow- white, where black corresponds to the zero counts and white to the maximum intensity. It can be seen that the peak intensities of the TOF-SIMS spectra (figure 5.4) correlate with the surface composition and distribution of each ion. For example, it can be inferred from figure 5.5 (e) that oxygen was by far most evenly distributed on the surface and it yielded the highest number of counts while both

dopants (Gd^{3+} and Pr^{3+}) gave the least number of counts and their distribution was not as even as those of other elements.

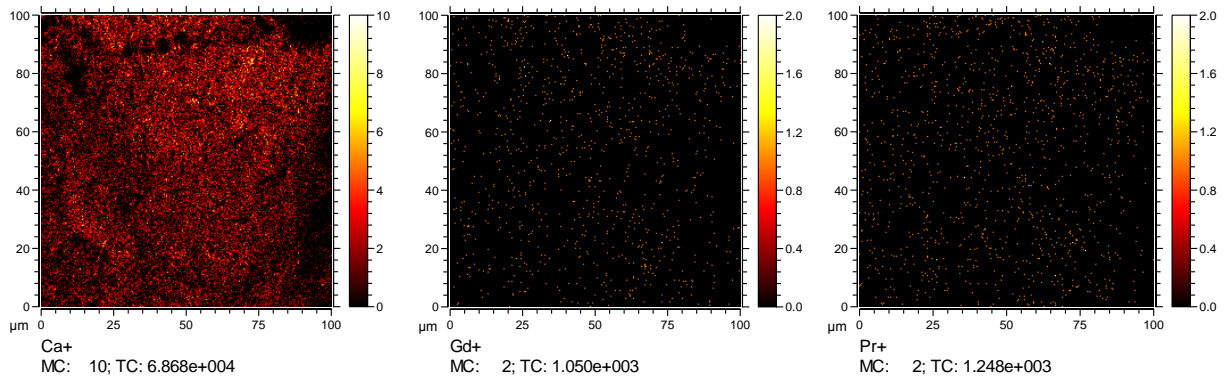


Figure 5.6 (a) TOF-SIMS chemical images of $Ca_5(PO_4)_3OH:Gd^{3+},Pr^{3+}$ phosphor powder for an area of 100 $\mu m \times 100 \mu m$ for positive ions.

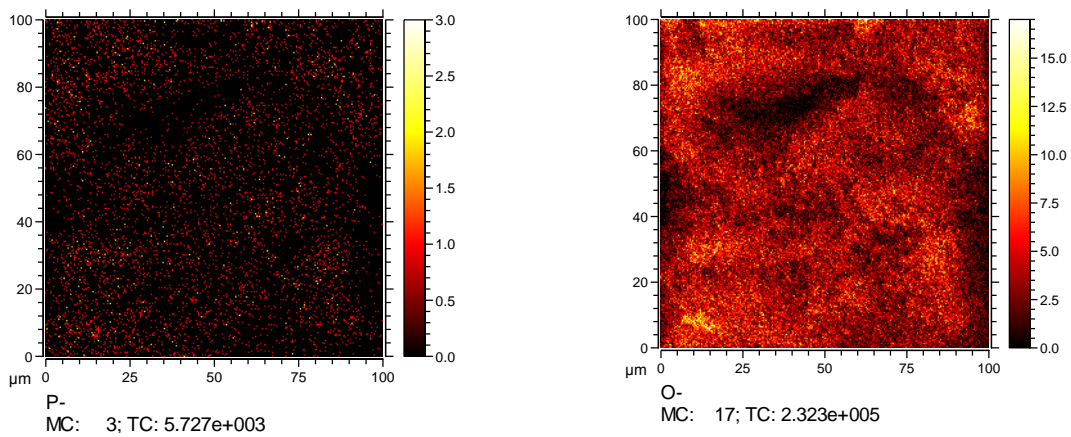


Figure 5.6 (b) TOF-SIMS chemical images of $Ca_5(PO_4)_3OH:Gd^{3+},Pr^{3+}$ phosphor powder for an area of 100 $\mu m \times 100 \mu m$ for negative ions.

Figure 5.7 (a) shows the optical absorption spectra of pure $\text{Ca}_5(\text{PO}_4)_3\text{OH}$ host, doped with gadolinium, praseodymium, and co-doped with both Gd^{3+} and Pr^{3+} . The host shows strong absorption peaks at 207 nm (5.99 eV) and 300 nm (4.13 eV) attributed to inter-band transition [11] and defects (e.g. vacancies or incidental impurities) respectively. The absorption spectrum of $\text{Ca}_5(\text{PO}_4)_3\text{OH}:\text{Gd}^{3+}$ resembles that there were no absorptions from Gd^{3+} . On the other hand the $\text{Ca}_5(\text{PO}_4)_3\text{OH}:\text{Pr}^{3+}$ and $\text{Ca}_5(\text{PO}_4)_3\text{OH}:\text{Gd}^{3+},\text{Pr}^{3+}$ systems have in addition to the host and defects absorptions, narrow line absorptions peaks at $\sim 450 - 600$ nm ascribed to the $f \rightarrow f$ transitions of Pr^{3+} ions. The absorption bands at $\sim 450 - 600$ nm are assigned to ${}^3\text{H}_4 \rightarrow {}^3\text{P}_{(j=0,1,2)}$ and ${}^3\text{H}_4 \rightarrow {}^1\text{D}_2$ transitions of Pr^{3+} ion. These compare well with the result reported previously [12, 13]. The optical direct band gap energy (E_g) of $\text{Ca}_5(\text{PO}_4)_3\text{OH}$ was determined from a plot of $(\alpha h\nu)^2$ versus photon energy ($h\nu$) shown in figure 5.7 (b). Here α is the absorption coefficient, h is Planck's constant and ν is the frequency of the radiation. The estimated E_g value was obtained by extrapolating the line to the axis where $(\alpha h\nu)^2 = 0$ and it was found to be 5.00 ± 0.05 eV. This value is similar to the value reported previously [14].

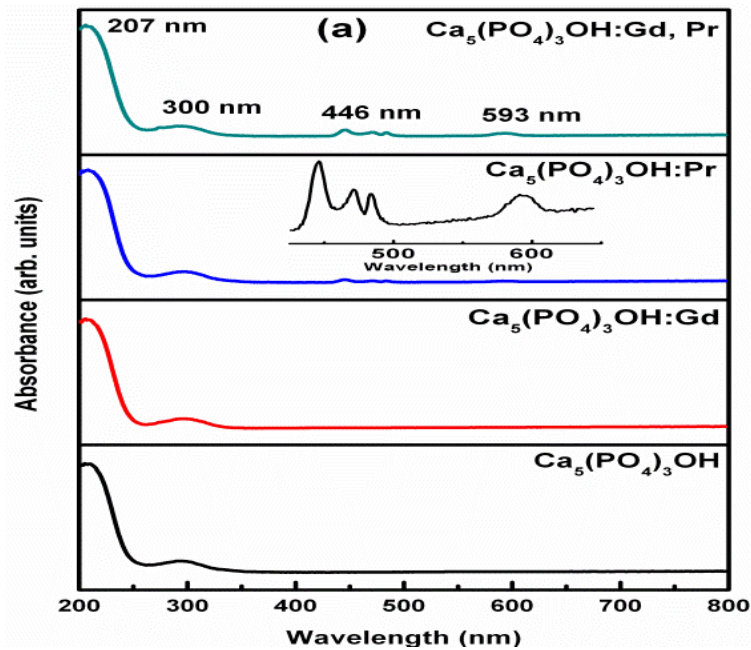


Figure 5.7 (a) Optical absorption spectra of $\text{Ca}_5(\text{PO}_4)_3\text{OH}:\text{Gd}^{3+},\text{Pr}^{3+}$ phosphor powders.

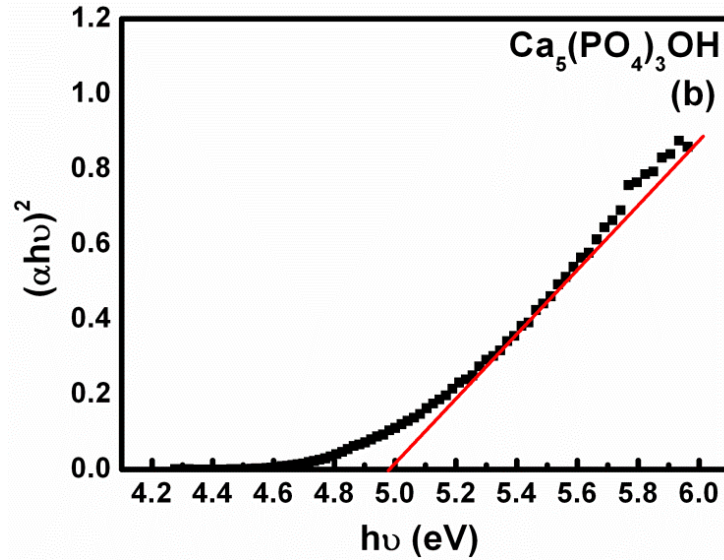


Figure 5.7 (b) $(\alpha h\nu)^2$ vs photon energy ($h\nu$) plot of $\text{Ca}_5(\text{PO}_4)_3\text{OH}:\text{Gd}^{3+},\text{Pr}^{3+}$ phosphor powders.

Figure 5.8 (a) shows the PL (i) excitation and (ii) emission spectra of $\text{Ca}_5(\text{PO}_4)_3\text{OH}:\text{Gd}^{3+}$ with different concentrations of Gd^{3+} ion. The spectra were recorded when monitoring the Gd^{3+} emission at 313 nm. The sharp peaks shown in the figure can be assigned to the $4f \rightarrow 4f$ intraconfiguration forbidden transitions of Gd^{3+} [15]. Figure 5.8 (a) (i) shows the minor excitation peaks at 245, 254 nm and the major one at 275 nm corresponding to $^8\text{S}_{7/2} \rightarrow ^6\text{D}_j$, $^8\text{S}_{7/2} \rightarrow ^6\text{I}_j$ and $^8\text{S}_{7/2} \rightarrow ^6\text{G}_j$ transitions of Gd^{3+} respectively [16, 17]. Figure 5.8 (a) (ii) shows sharp emission peak at 313 nm assigned to $^6\text{P}_{7/2} \rightarrow ^8\text{S}_{7/2}$ transition of Gd^{3+} ion. The intensity of these peaks was shown to increase with increasing concentration of Gd^{3+} from 1 – 11 mol %. For the maximum concentration of Gd^{3+} (i.e. 11 mol %), a broad excitation band with a maximum at ~207 nm (5.99 eV) was observed. This peak could be assigned to the interband excitation of the $\text{Ca}_5(\text{PO}_4)_3\text{OH}$ host. At lower concentrations of Gd^{3+} , the interband excitation peak was found to be relatively low and is probably overshadowed by the higher signal to noise ratio. In other words, for concentrations of Gd^{3+} lower than 11 mol% the interband excitation was suppressed.

Figure 5.8 (b) shows the PL (i) excitation and (ii) emission spectra of $\text{Ca}_5(\text{PO}_4)_3\text{OH}:\text{Pr}^{3+}$ with concentrations of Pr^{3+} varied from 0.5 – 5 mol%. The excitation spectra were recorded while monitoring emission at 603 nm. The excitation peaks at 447 nm and 483 nm are due to $^3\text{H}_4 \rightarrow ^3\text{P}_2$

and ${}^3\text{H}_4 \rightarrow {}^3\text{P}_0$ transitions of Pr^{3+} respectively. The PL emission ($\lambda_{\text{exc}} = 447 \text{ nm}$) consists of a narrow peak at 603 nm corresponding to ${}^3\text{P}_0 \rightarrow {}^3\text{H}_4$ transition of Pr^{3+} .

Figure 5.8 (c) shows the (i) PLE and (ii) PL spectra of $\text{Ca}_5(\text{PO}_4)_3\text{OH}:\text{Gd}^{3+},\text{Pr}^{3+}$ phosphor powder. The PLE spectra consist of narrow peaks from Gd^{3+} situated at the same positions (245, 254 nm and the major one at 275 nm) as those shown in Figure 5.8 (c) (i) and a broadband at 222 nm. Although the broad 222 nm peak is very close to the 207 nm peak assigned to the band-to-band absorption of the host in the UV-vis spectrum shown in figure 5.7, it cannot be assigned to the band-to-band excitation of the host because neither the undoped nor the Gd^{3+} single doped host could be excited by the monochromatized xenon lamp at the wavelength of 222 nm. It is therefore reasonable to assign this excitation band to the $4f \rightarrow 4f5d$ transition of Pr^{3+} . Our assignment of this peak is consistent with the predicted location of the $4f5d$ band of Pr^{3+} in different inorganic solid hosts [16]. It also important to mention that the Gd^{3+} excitation peaks of $\text{Ca}_5(\text{PO}_4)_3\text{OH}:\text{Gd}^{3+},\text{Pr}^{3+}$ system are less intense when compared to those in $\text{Ca}_5(\text{PO}_4)_3\text{OH}:\text{Gd}^{3+}$ system. The peak intensity of the Pr^{3+} excitation and UV emission at 313 nm improved considerably after incorporating Pr^{3+} . The maximum excitation was observed when the molar ratio of Gd^{3+} to Pr^{3+} was 10:2 and this was reduced at the ratio of 11:1. The $f-f$ excitation peaks from Pr^{3+} single doped $\text{Ca}_5(\text{PO}_4)_3\text{OH}$ observed in figure 5.8 (b) are suppressed completely. Figure 5.8 (c) (ii) shows the PL emission spectra of $\text{Ca}_5(\text{PO}_4)_3\text{OH}:\text{Gd}^{3+},\text{Pr}^{3+}$ after being excited at 222 nm. The spectra show only the emission peak at 313 nm corresponding to the ${}^8\text{S}_{7/2} \rightarrow {}^6\text{G}_j$ transitions of Gd^{3+} . The narrow line peak at 603 nm corresponding to ${}^3\text{P}_0 \rightarrow {}^3\text{H}_4$ transition of Pr^{3+} was also suppressed. These data suggest that Pr^{3+} acted to harvest the primary excitation energy and transfer it non-radiatively to Gd^{3+} . The fact the red emission from Pr^{3+} at 603 nm was suppressed implies that the rate of energy transfer from Pr^{3+} to Gd^{3+} was faster than the electron capture by the hole that could result in the radiative emission by Pr^{3+} .

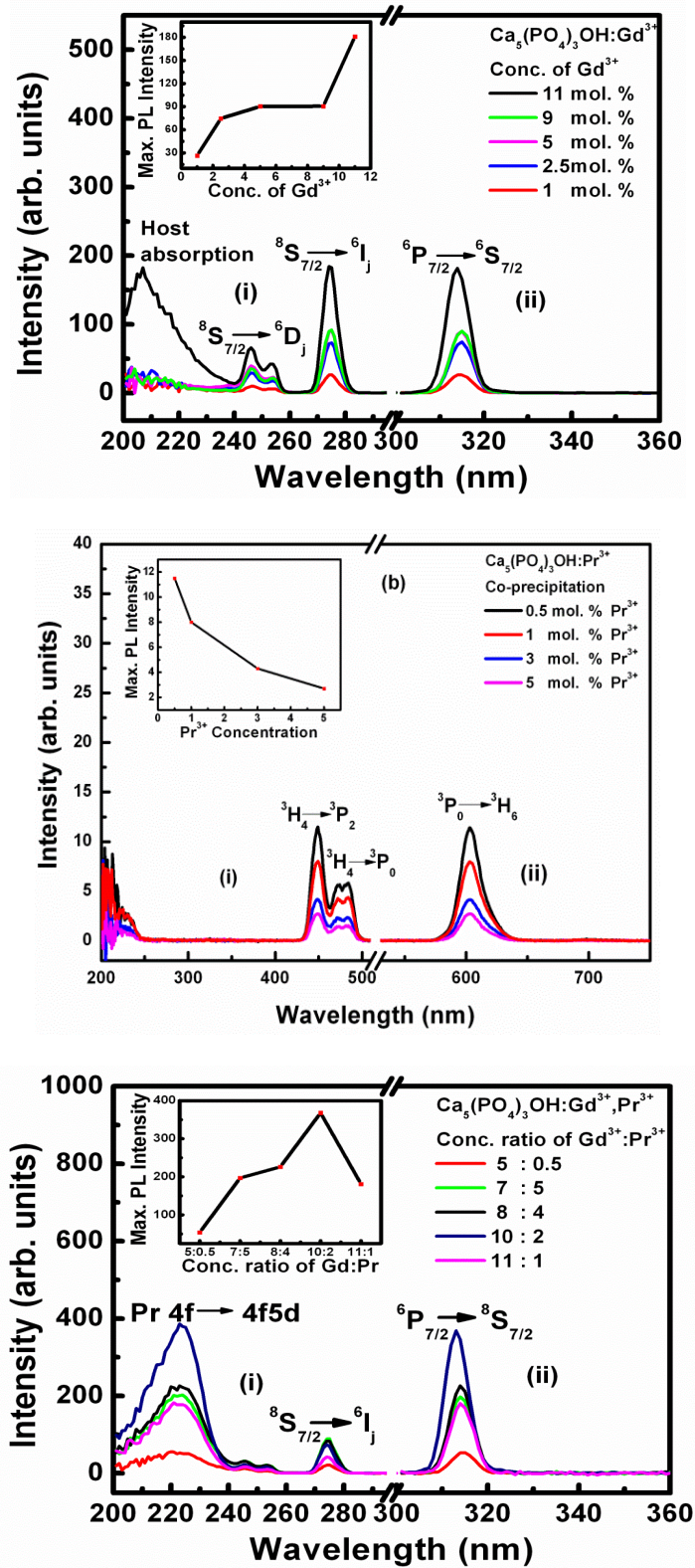


Figure 5.8 PL excitation and emission spectra of (a) $\text{Ca}_5(\text{PO}_4)_3\text{OH}:\text{Gd}^{3+}$, (b) $\text{Ca}_5(\text{PO}_4)_3\text{OH}:\text{Pr}^{3+}$, and (c) $\text{Ca}_5(\text{PO}_4)_3\text{OH}:\text{Gd}^{3+}, \text{Pr}^{3+}$ phosphor powders.

5.4 Conclusion

$\text{Ca}_5(\text{PO}_4)_3\text{OH}:\text{Gd}^{3+},\text{Pr}^{3+}$ phosphors were successfully synthesized via the co-precipitation method and confirmed by XRD analyses. The $\text{Ca}_5(\text{PO}_4)_3\text{OH}$ powder was crystallized in the hexagonal phase. Peak positions and surface images of each ion present in the material was observed by TOF-SIMS measurements. The SEM images show agglomeration of small spherical particles and all the elements present in the phosphors were confirmed by EDS. Gd^{3+} singly doped $\text{Ca}_5(\text{PO}_4)_3\text{OH}$ exhibited narrowband emission peaks at 313 nm. Pr^{3+} incorporation in the $\text{Ca}_5(\text{PO}_4)_3\text{OH}:\text{Gd}^{3+}$ system resulted, through energy transfer, in enhanced PL intensity of the Gd^{3+} , making it a superior phosphor for application in phototherapy lamps.

References

- [1] B. Pavan, D. Ceresoli, M.M.J. Tecklenburg, M. Fornari, *Solid State Nucl. Magn. Reson.*, 2012, **45-46**, 59-65
- [2] I.V. Berezovskaya, N.P. Efryushina, E.V. Zubar, V.P. Dotsenko, *Proc. NAP*. 2012, 1[1], 24-1-4
- [3] J.N. Hart, P.W. May, N.L. Allan, K.R. Hallam, F.Claeyssens, G.M. Fuge, M. Ruda, P.J. Heard, *J. Solid State Chem.*, 2013, **198**, 466-474
- [4] W. Zhang, X. Li, R. Yang, *Polym. Degrad. Stab.*, 2014, **99**, 289-303
- [5] G.D. Khattak, A. Mekki, L.E. Wenger, *J. Non-Cryst. Solids*, 2009, **355**, 2148-2155
- [6] M. Ahren, L. Selegard, F. Soderlind, M. Linares, J. Kauczor, P. Norman, P.V. Kall, K. Uvdal, *J. Nanopart. Res.* 2012, **14**, 10061-100617
- [7] J. Chung, J. Park, J-G Park, B-H Choi, S-J Oh, E-J Cho, H-D Kim, Y.S. Kwon, *J. Korean Phys. Soc.* 2001, **38**, 744-749
- [8] A. Mekki, A. Ziq Kh, D. Holland, C.F. McConville, *J. Magn. Magn. Mater.* 2003, **260**, 60-69
- [9] H. Ogasawara, A. Kotani, R. Potze, G.A. Sawatzky, B.T. Thole, *Phys. Rev. B*, 1991, **44**, 5465-9
- [10] S.W. Han, J.D. Lee, K.H Kim, H. Song, W.J. Kim, S.J Kwon, H.G Lee, C. Hwang, J.L. Jeong, J.S. Kang, *J. Korean Phys. Soc* 2002, **40**, 501-510
- [11] S. Okamoto, R. Uchino, K. Kobayashi, H. Yamamoto H, *J. Appl. Phys.*, 2009, **106**, 013522-5
- [12] L. Chen, S. Zhiguo, Q. Jianbei, Y. Zhengwen, Y. Xue, Z. Dacheng, Y. Zhaoyi, W. Rongfei, X. Yuanyuan, C. Yuechan, *J.Llumin*, 2012, **132**, 1807-1811
- [13] Yu-Chun Li, Yen-Hwei Chang, Yee-Shin Chang, Yi-Jing lin, Chih-Hao Laing, *J Phys. Chem. C*, 2007, **111**, 10682-10688
- [14] T. Mineharu, W. Masato, Y. Naoya, W. Toshiya, *J. Mol. Catal. A*, 2011, **338**, 18-23
- [15] B. Han, H. Liang, Q. Su, Y. Huang, Z. Gao, Y. Tao, *Applied Physics B*, 2010, **100**, 865-869

- [16] J. Zhong, H. Liang, Q. Su, J. Zhou, Y. Huang, Z. Gao, Y. Tao, J. Wang, *J. Appl. Phys. B*, 2010, **98**, 139-147
- [17] L. Yu-Chun, C. Yen-Hwei, L. Yu-Feng, C. Yee-Shin, L. Yi-Jing, *J. Phys. Chem.Solids*, 2007, **68**, 1940-1945

Chapter 6: Thermoluminescence properties of $\text{Ca}_5(\text{PO}_4)_3\text{OH}:\text{Gd}^{3+},\text{Pr}^{3+}$ phosphor prepared via co-precipitation method

6.1 Introduction

Thermoluminescence (TL) is the light emission from a solid material (insulator or semiconductor) when it is heated after being initially irradiated at low temperature by some other kind of radiation sources such as α - rays, β - rays, γ - rays, UV rays and X-ray [1]. When a material is exposed to ionizing radiation a certain percentage of the charge carriers (electron and holes) may be trapped at certain imperfections in the lattice, which are called traps [2]. The trapping states are associated with the vacancies, interstitials and impurities. During heating at controlled rate, the trapped electrons and holes are thermally released to the conduction band and then recombine with trapped charge carriers of the opposite sign. Radiative recombination gives rise to TL. The plot of intensity of emitted light versus the temperature is known as a TL glow curve. A glow curve may exhibit one or many peaks depending upon the number of electron traps with different trap depths, present in the lattice. These peaks may or may not be well separated. The position, shape and intensity of the glow peaks therefore are characteristic of the specific material and the impurities and defects presents. Therefore each TL glow curve corresponds to the release of an electron (or hole) from a particular trap level within the band gap of the material.

6.2 Kinetic Analysis

The TL glow curve is used for kinetic analysis, by establishing the physical parameters such as (E – Activation energy, S – Frequency factor, and b – order of kinetics) of the trap. There are

several methods which can be used for evaluating these parameters which are (i) Initial rise method, (ii) Peak shape method, (iii) Variable heating rate and (iv) T_m - T_{stop} . Initial rise part of TL curve is exponentially dependant on temperature

$$I(t) = n \times e^{-\frac{E}{kT_m}} \quad (6.1)$$

The critical temperature must not correspond to an intensity which is approximately 10-15 % of the maximum intensity [1]. In applying initial rise method, a graph of $\ln(I)$ versus $1/T$ is drawn and a straight line of slope $-E/k$ is obtained, from which the activation energy (E) can easily be found [3]. In peak shape method, three points from the glow curve are used. These are maximum temperature peak, low and high half-intensity temperatures at T_1 and T_2 . Kinetic parameters can be evaluated by using full width of the peak at half-height ($\omega = T_2 - T_1$), low-temperature half-width ($\tau = T_m - T_1$), or high-temperature half-width ($\delta = T_2 - T_m$), then E can be calculated by:

$$E = A_\gamma \left(\frac{kT_m^2}{\gamma} \right) - B_\gamma \quad 2kT_m \quad (6.2)$$

where γ is ω , τ or δ , and (A_γ and B_γ) are the constants [1]. Heating rate method relies on the shift of the peak position with heating rate. The assumption is that the pre-exponential factor (s) is constant; the only cause of the change in peak maximum is the heating rate (β), when

$$\beta = \left(\frac{sk}{E} \right) T_m^2 \times e^{\left(-\frac{E}{kT_m} \right)} \quad (6.3)$$

It follows that

$$\ln \left(\frac{T_m^2}{b} \right) = \left(\frac{E}{k} \right) \left(\frac{1}{T_m} \right) + \ln \left(\frac{E}{sk} \right) \quad (6.4)$$

from which a plot of $\ln(T_m^2/b)$ versus $1/T_m$ should give a straight line with slope E/k , giving a means to evaluate the activation energy. β has a powerful influence on peak position. T_m - T_{stop} is

a method where a sample is heated to T_{stop} on the low temperature at the tail of the glow curve. Then it is cooled back and heated up to first maximum. The procedure is repeated on the irradiated sample using slightly higher T_{stop} , it is heated at the same linear rate (increasing in small steps of 2-5 deg.) for all remaining glow curve.

6.3 Experimental

The preparation method of $\text{Ca}_5(\text{PO}_4)_3\text{OH}:\text{Gd}^{3+},\text{Pr}^{3+}$ powder phosphor is the same as the one discussed in chapter 5. Thermoluminescence measurements were done using a Riso TL/OSL reader (model TL/OSL-DA-20), and a photomultiplier tube in the system was used for photon counting. Samples were irradiated to different doses using a ^{90}Sr beta source at a dose rate of 0.1028 Gy/s. The glow curves were recorded using narrow band interference filters with peak transmissions located in the range of 340 – 380 nm. The background signal was subtracted from the TL glow curves. All TL glow curves were recorded with linear heating rates under nitrogen flow.

6.4 Results and Discussion

Figure 6.1 shows a TL glow curve of $\text{Ca}_5(\text{PO}_4)_3\text{OH}:\text{Gd}^{3+},\text{Pr}^{3+}$ phosphor measured at heating rate of $5\text{ }^{\circ}\text{C}.\text{s}^{-1}$ from 270 to 770 K after being irradiated with a beta radiation of 12 Gy. The glow curve consists of a single peak at 347 K, which is attributed to the maximum temperature at which the electrons were detrapped from traps to conduction band. The background signal is shown for comparison.

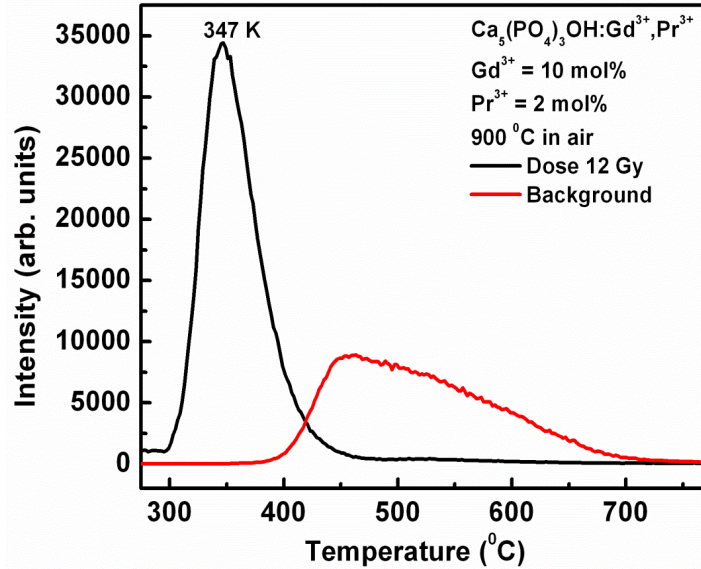


Figure 6.1 Thermoluminescence glow curve of $\text{Ca}_5(\text{PO}_4)_3\text{OH}:\text{Gd}^{3+},\text{Pr}^{3+}$ and background signal.

Figure 6.2 shows the thermoluminescence (TL) glow curve of $\text{Ca}_5(\text{PO}_4)_3\text{OH}:\text{Gd}^{3+},\text{Pr}^{3+}$ phosphor measured at the heating rate of $5\text{ }^\circ\text{C}\cdot\text{s}^{-1}$ after the phosphor was irradiated with beta irradiation in the range of 6 – 186 γGy by a $^{90}\text{Sr}/^{90}\text{Y}$ beta source. The TL glow curve has a single glow band in the range of 300 to 750 K, with a maximum temperature at 362 K. The peak position shifted towards higher temperature with an increase in dose. The peak shifting to high temperature by exposing material to different doses implies that the system follow neither first or second order kinetics, but general order [4]. The single peak suggests that there is only one type of electron trap in the forbidden band of the material, and the trap may be due to the calcium or oxygen defects in the material. For 6 γG excitation, the peak maximum is located at 343 K, while for 186 γG excitation it has shifted to 362 K. The inset shows that the intensity increases with an increasing excitation duration range. This might be the indication that the mechanism of the underlying luminescence process is more complex and cannot be described by first order kinetics [5]. The interpretation of thermoluminescence in terms of mechanisms involved in the emission of the luminescence is aided for kinetic analysis from the glow curve.

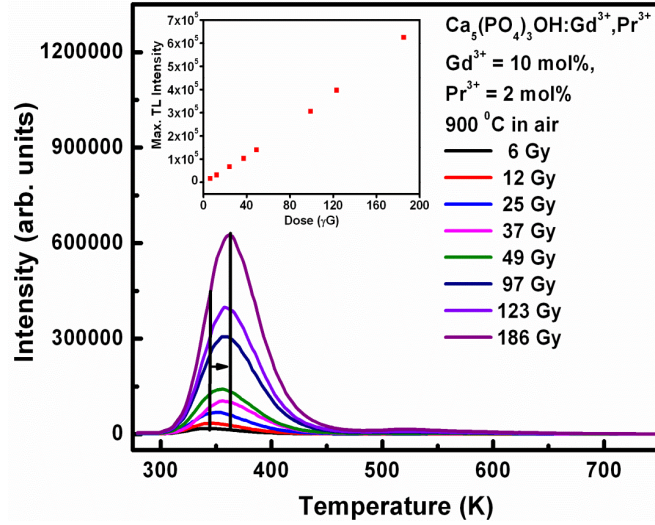


Figure 6.2 Thermoluminescence glow-curve of $\text{Ca}_5(\text{PO}_4)_3\text{OH}:\text{Gd}^{3+},\text{Pr}^{3+}$ phosphor at different beta irradiation from 6 – 186 Gy.

Figure 6.3 shows the deconvoluted glow curve of beta irradiated by 12 Gy $\text{Ca}_5(\text{PO}_4)_3\text{OH}:\text{Gd}^{3+},\text{Pr}^{3+}$ phosphor. There are two deconvoluted peaks at 339 K and 361 K. This shows that at both lower and higher temperature, the glow curve consist of a single peak. The TL glow curve corresponding to irradiation dose as shown in the figure is analyzed using the glow curve deconvolution method on the basis of general order kinetics.

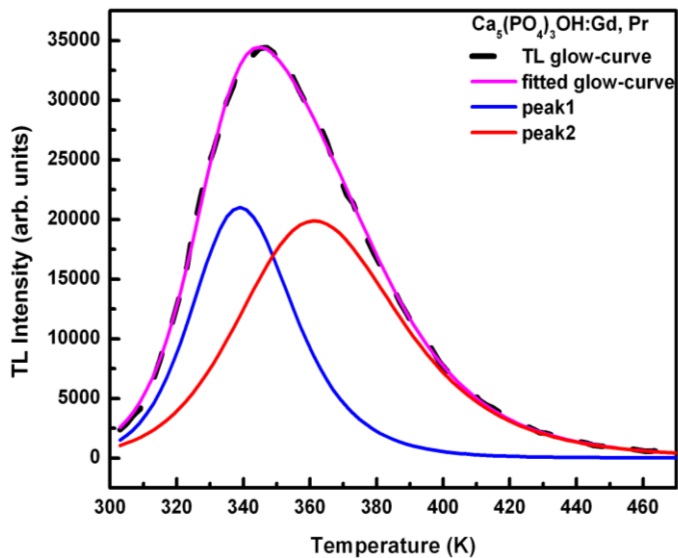


Figure 6.3 Deconvolution TL glow-curve showing the experimental data (black broken line) and the fitted (pink line) glow curve of $\text{Ca}_5(\text{PO}_4)_3\text{OH}:\text{Gd}^{3+},\text{Pr}^{3+}$ phosphor.

6.4.1 Initial rise method

Figure 6.4 (c) shows the plots of the activation energy versus dose. The activation energy (E_A) is extracted directly from the slope of $\ln(I)$ versus $1/T$ when using eq. (1). The slope obtained using polynomial fit through the plot is multiplied with Boltzmann constant ($k = 8.617 \times 10^{-5} \text{ eV K}^{-1}$) to obtain the value of E_A . The calculated average value for E_A at different doses was found to be 0.91 eV.

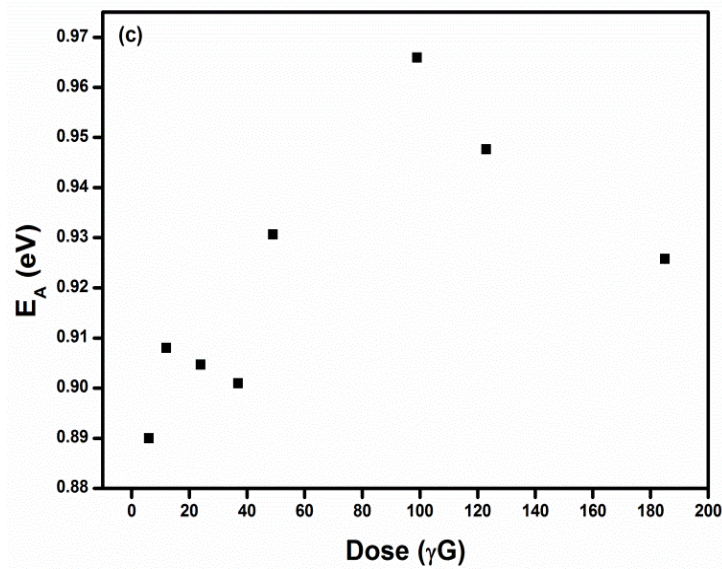


Figure 6.4 Activation energy versus dose spectrum of $\text{Ca}_5(\text{PO}_4)_3\text{OH}:\text{Gd}^{3+},\text{Pr}^{3+}$ phosphor.

6.4.2 Peak shape method

In peak shape method, three points from the glow curve are used. These are maximum temperature peak, low and high half-intensity temperatures at T_1 and T_2 . Kinetic parameters can be evaluated by using full width of the peak at half-height ($\omega = T_2 - T_1$), low-temperature half-width ($\tau = T_m - T_1$), or high-temperature half-width ($\delta = T_2 - T_m$) [6], then E can be calculated by using eq. (6.2), where γ is any ω , τ or δ , and (A_γ and B_γ) are constants. Values for constants A_γ and B_γ were calculated using expressions given by Chen [7] and are as follows:

$$c_\tau = 1.51 + 3(\mu_g - 0.42) \quad (6.5)$$

$$c_{\delta} = 0.976 + 7.3(\mu_g - 0.42) \quad (6.6)$$

$$c_{\omega} = 2.52 + 10.2(\mu_g - 0.42) \quad (6.7)$$

$$b_{\tau} = 1.58 + 4.2(\mu_g - 0.42) \quad (6.8)$$

$$b_{\omega} = 1 \quad (6.9)$$

$$b_{\delta} = 0 \quad (6.10)$$

$$\mu_g = - \quad (6.11)$$

Figure 6.5 shows the plots of the activation energy against dose by peak shape methods. The activation energies for ω , τ and δ , were calculated by using eq. (4) and average activation energies for each were 0.75, 1.03, and 0.42 eV respectively. The values of the activation energy calculated by analyzing the geometrical shape of a TL glow peak are susceptible to error due to various reasons including subjectivity in accurately determining the temperatures corresponding to the intensity at half-height [7].

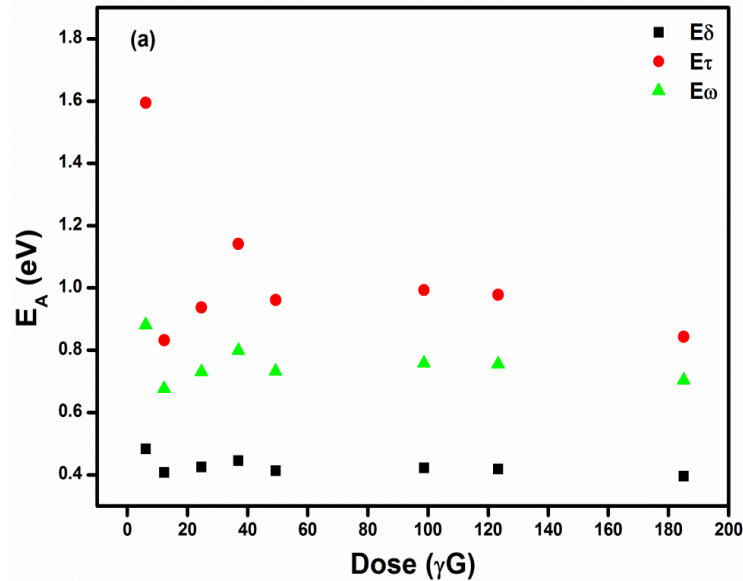


Figure 6.5 Plot of the Peak shape method used for calculation of activation energy.

6.4.3 Heating rate method

Heating rate method relies on the shift of the peak position with heating rate. The assumption is that the pre-exponential factor (s) is constant; the only cause of the change in peak maximum is the heating rate (β), when

$$\beta = \left(\frac{sk}{E} \right) T_m^2 \times e^{\left(-\frac{E}{kT_m} \right)} \quad (6.3)$$

It follows that

$$\ln \left(\frac{T_m^2}{b} \right) = \left(\frac{E}{k} \right) \left(\frac{1}{T_m} \right) + \ln \left(\frac{E}{sk} \right) \quad (6.4)$$

from which the plot of $\ln (T_m^2/b)$ versus $1/T_m$ should give a straight line with the slope E/k , giving a means to evaluate the activation energy [2]. β has a powerful influence on peak position. The variable heating rate was used to determine the activation energy associated with the glow peak of the sample. Figure 6.6 shows the influence of variable heating rate on the main glow peak. The graphs show the peaks shifting to higher temperature with an increase in heating rate and it is attributed to electron-phonon interaction. The inset (a) in figure 6.6 shows a plot of maximum temperature versus heating rate. Inset (b) in figure 6.6 shows the plot of luminescence intensity against heating rate. The luminescence increases with increasing heating rate from 0.6 to 2.0 $^{\circ}\text{C}.\text{s}^{-1}$ and start to decrease from 3.0 to 5.0 $^{\circ}\text{C}.\text{s}^{-1}$, and the decrease may be due to thermal quenching as the glow peak shift to higher temperature.

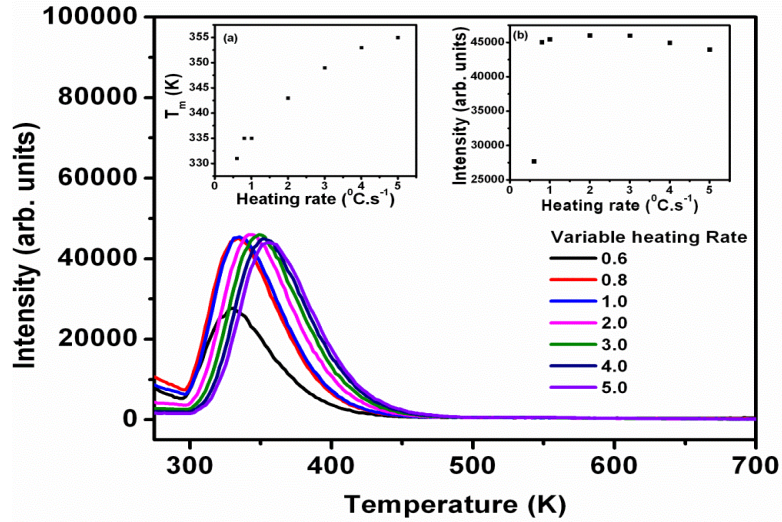


Figure 6.6 Thermoluminescence glow curve of $\text{Ca}_5(\text{PO}_4)_3\text{OH}:\text{Gd}^{3+},\text{Pr}^{3+}$ phosphor using variable heating rate method.

Fig. 6.7 shows a plot of $\ln(T_m^2/\beta)$ versus $1/T_m$, the solid line through data points is the best fit of eq. (4). This figure is used to calculate the parameter activation energy by multiplying the slope with Boltzmann constant ($8.617 \times 10^{-5} \text{ eV k}^{-1}$), and E_A was found to be 0.83 eV. The calculated energy is comparable to the energy found when using initial rise and peak shape method for E_0 . The spectra show a straight line, suggesting that the value of E_A remains unchanged.

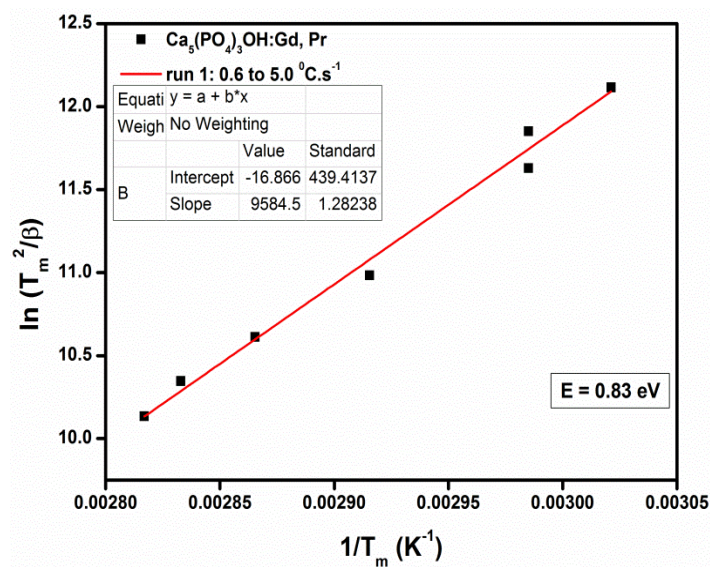


Figure 6.7 Shows a plot of $\ln(T_m^2/\beta)$ versus $1/T_m$

6.4.4 $T_m - T_{stop}$ method

Figure 6.8 shows the results of applying the $T_m - T_{stop}$ method on TL peaks in the glow curve. $T_m - T_{stop}$ is method where a sample is heated to T_{stop} at low temperature at the tail of the glow curve. Then it is cooled back and heated up to first maximum. The procedure is repeated on the irradiated sample using slightly higher T_{stop} , and it is heated at the same linear rate (increasing in small steps of 2-5 deg.) for all remaining glow curve. The spectrum shows straight line, this kind of spectrum is often observed when the glow curve consists of closely overlapping TL peaks and from this kind of spectrum it is neither first nor second order.

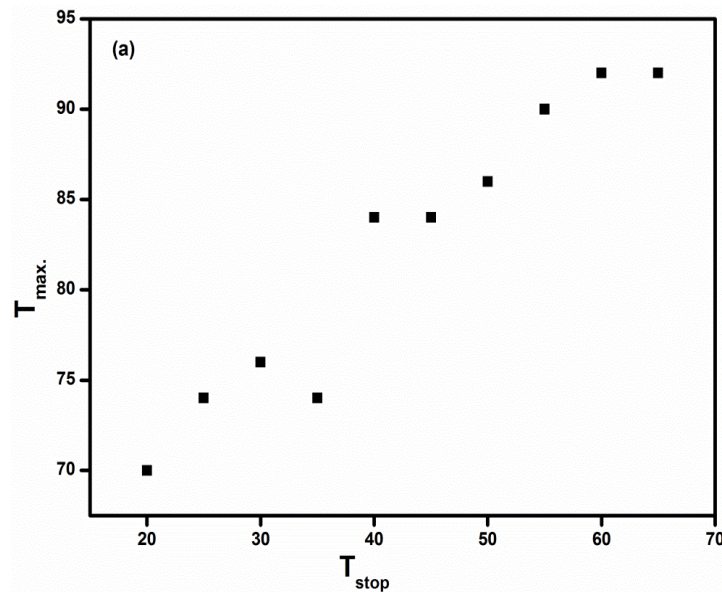


Figure 6.8 $T_m - T_{stop}$ plot of $Ca_5(PO_4)_3OH:Gd^{3+},Pr^{3+}$ phosphor.

Table 1 shows the results of the activation energy for initial rise method. Activation energy is the vertical separation between the trap and conduction band. The average calculated activation energy with initial rise method was found to be 0.91 eV.

Table 2 shows the results for the activation energies for peak shape method. The E_A was evaluated using three parameters such as ω , τ and δ . The calculated E_A for all the parameters were found to be 0.75, 1.03 and 0.42 eV. The energies are comparable to the activation energy found using initial rise method.

Table 3 shows the calculated activation energy using variable heating rate method. The activation energy calculated was 0.60 eV which is also comparable to the energies calculated on the initial rise and peak shape methods.

Table 1.

Initial Rise method

Dose (Gy)	T_{max} (K)	I_{max}	Slope	E_A (eV)
6	66	17615	-10395	0.89
12	80	32470	-10538	0.90
24	78	68172	-10498	0.90
36	76	103756	-10463	0.90
49	82	141299	-10800	0.93
98	84	307074	-11216	0.96
123	86	397875	-10998	0.94
185	90	625478	-10745	0.92
Average E_A (eV)				0.91 eV

Table 2.**Peak Shape method**

Dose (Gy)	T ₁ (K)	T ₂ (K)	T _{max} (K)	ω	τ	δ	E _{ω} (eV)	E _{τ} (eV)	E _{δ} (eV)
6	49.27	107.28	66	58.01	16.37	41.28	0.88	1.59	0.48
12	51.21	107.65	76	56.44	24.79	31.65	0.68	0.83	0.41
24	54.57	110.99	78	56.42	23.43	32.99	0.73	0.93	0.42
36	55.81	113.5	77	57.69	21.19	36.5	0.80	1.14	0.45
49	58.11	117.06	82	58.95	23.89	35.01	0.73	0.96	0.41
98	60.62	118.31	84	57.69	23.38	34.31	0.75	0.99	0.42
123	62.29	119.98	86	57.69	23.71	33.98	0.76	0.98	0.41
185	64.38	120.82	90	56.44	25.62	30.82	0.70	0.84	0.39
Average E _A (eV)							0.75	1.03	0.42

Table 3.**Heating rate method**

Heating rate ($^{\circ}\text{C}.\text{s}^{-1}$)	T_{max} (K)	I_{max} (arb. Units)	Slope	E_{A} (eV)
0.6	58	27707	-6889	0.59
0.8	62	45066	-7562	0.65
1	62	45463	-7999	0.69
2	70	46014	-8747	0.75
3	76	45996	-8463	0.73
4	80	44929	-7824	0.67
5	82	43988	-7680	0.66
Average E_{A} (eV)				0.60

6.5 Conclusion

Thermoluminescence glow curve of $\text{Ca}_5(\text{PO}_4)_3\text{OH}:\text{Gd}^{3+},\text{Pr}^{3+}$ phosphor shows the single TL peak due to only one type of trap formed in the material. The background signal is not comparable to TL glow curve. TL glow curve shows an increase in intensity as dose increases and the shifting (to the right) of the peaks may be due to change in particle size. The activation energies were evaluated using different methods such as initial rise, peak shape, heating rate and $T_{\text{m}} - T_{\text{stop}}$. The activation energies were almost comparable on all methods applied.

References

- [1] S.W.S. McKeever, *Thermoluminescence of solids*, Cambridge University Press (ISBN: 0-521-36811 1) 1985
- [2] B.J.R.S. Swamy, B. Sanyal, R. Vijay, P.R. babu, D.K. Rao, N. Veeraiah, *Ceram. Int.*, 2014, **40**, 3707-3713
- [3] V. Correcher, J.M. Gomez-Ros, J. Garcia-Guinea, M. Lis, L. Sanchez-Munoz, *Radiat. Meas.*, 2008, **43**, 269-272
- [4] L.L. Noto, M.L. Chithambo, O.M. Ntwaeaborwa, H.C. Swart, *J. Alloys Comp.*, 2014, **589**, 88-93
- [5] A. Timar-Gabor, C. Ivascu, S. Vasiliniuc, L. Daraban, I Ardelean, C. Cosma, O. Cozar, *Appl. Radiat. Isot.*, 2011, **69**, 780-784
- [6] B.J.R.S. Swamy, B. Sanyal, Y. Gandhi, R.M. kadam, V.N. Rajan, P.R. Rao, N. Veeraiah, *J. Non-Cryst. Solids*, 2013, **368**, 40-44
- [7] R. Chen, S.W.S McKeever, *Thermoluminescence and Related Phenomena*, (Singapore: World Scientific) 1997

Chapter 7: TOF SIMS analysis and enhanced UVB photoluminescence by energy transfer from Pr³⁺ to Gd³⁺ in Ca₃(PO₄)₂:Gd³⁺,Pr³⁺ phosphor prepared by urea assisted combustion method

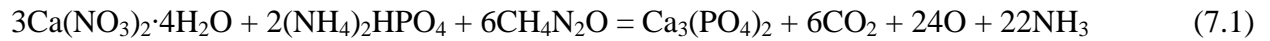
7.1 Introduction

Tri-Calcium phosphate (TCP) is one of the most important materials used in the biomedical fields because of its biocompatibility and osteoconductivity (ability to form a chemical bond with living tissues). Phosphate materials containing calcium oxide are intensively studied because they have bioactive potential [1]. The phosphate tetrahedron shares one or more oxygen atoms with adjacent tetrahedrons to form chains, rings or complex three-dimensional networks [2]. Recently, it has been used as a host for rare-earth elements to prepare light emitting materials or phosphors that can be used in light emitting devices including television, computer screens and phototherapy lamps. For a possible application in phototherapy lamps, Ca₃(PO₄)₂ is doped with trivalent gadolinium (Gd³⁺) to produce a phosphor that gives a narrow line emission at ~313 nm corresponding to ⁶P_{7/2}→⁸S_{7/2} transitions. The Gd³⁺ ion has seven electron spins on the 4f orbital (spin angular momentum S = 7/2, orbital angular momentum L= 0, total angular momentum J = 7/2) and the ground state of the Gd³⁺ ion is referred to ⁸S_{7/2} [3]. This emission is classified as UVB radiation and it is investigated for possible use in phototherapy lamps to treat skin diseases like psoriasis, vitiligo, atopic dermatitis (eczema) and other photoresponsive skin disorders. There are many synthesis methods that can be used to prepare this phosphor including (wet precipitation, high temperature solid state route and sol-gel combustion method) [4-7]. In this study, urea assisted combustion method was used to prepare Gd³⁺-Pr³⁺ co-activated phosphors. When compared to others, this method is cost-effective and quick; and it has an

added advantage of ease of incorporation of dopants. Our data demonstrated the influence of urea on the crystallinity of the phosphors and the effect of Pr^{3+} co-doping on the photoluminescence (PL) intensity of the UVB narrow line emission at ~ 313 nm due to $f-f$ transitions of Gd^{3+} .

7.2 Experimental

Gd^{3+} and Pr^{3+} co-doped $\text{Ca}_3(\text{PO}_4)_2$ samples were synthesized by combustion with urea as a fuel. The mass of urea was varied from 0.5 – 10g. $\text{Ca}(\text{NO}_3)_2 \cdot 4\text{H}_2\text{O}$, $(\text{NH}_4)_2\text{HPO}_4$, $\text{Gd}(\text{NO}_3)_3 \cdot 5\text{H}_2\text{O}$, $\text{Pr}(\text{NO}_3)_3 \cdot 6\text{H}_2\text{O}$ and $\text{CO}(\text{NH}_4)_2$ were used as precursors. When a complete reaction is assumed, the theoretical equation for the formation of $\text{Ca}_3(\text{PO}_4)_2$ is given by:



All reagents, in stoichiometric amounts, were dissolved in distilled water and the mixture was stirred vigorously until a thick pasty solution was formed. The solution was kept in a furnace maintained at 550 °C. The solution boiled, underwent dehydration and decomposed while generating combustible gases such as CO_2 , NH_3 and H_2O . The combustion ashes were cooled to room temperature and were grounded gently using a pestle and mortar resulting in a fine powder. The materials synthesized were $\text{Ca}_3(\text{PO}_4)_2$, $\text{Ca}_3(\text{PO}_4)_2:\text{Gd}^{3+}$, $\text{Ca}_3(\text{PO}_4)_2:\text{Pr}^{3+}$ and $\text{Ca}_3(\text{PO}_4)_2:\text{Gd}^{3+},\text{Pr}^{3+}$ with different concentrations of Gd^{3+} (in range of 0.5 – 10 mol %), Pr^{3+} (0.5 mol %), and $\text{Gd}^{3+}:\text{Pr}^{3+}$ (5:10 mol %). All the powders were annealed at 1000 °C in air. In the Gd^{3+} single doped $\text{Ca}_3(\text{PO}_4)_2$, the concentration of Gd^{3+} was varied from 0.5 – 10 mol% while the concentration of Pr^{3+} in both the Pr^{3+} single doped and $\text{Gd}^{3+}-\text{Pr}^{3+}$ co-doped $\text{Ca}_3(\text{PO}_4)_2$ was fixed at 0.5 mol%.

The XRD analysis was carried out using a Bruker AXS D8ADVANCE X-ray diffractometer, with a $\text{Cu}_{k\alpha 1}$ (1.5406 Å), the spectra were measured in the 2θ range of $25^\circ - 40^\circ$. Particle morphology analyses were carried out using a Shimadzu Superscan SSX-550 SEM system. A reflection-based high resolution TOF-SIMS instrument equipped with a primary Bi^{6+} ion source and a low-energy pulsed electron source (20 eV) for charge compensation was used to analyse the chemical composition and the distribution of dopants in the host lattice. The absorption and bandgap energy were evaluated using Perkin Elmer Lambda 950 UV-VIS spectrometer. PL data

were recorded using a Varian Cary Eclipse fluorescence spectrophotometer and a monochromatized 150 W xenon lamp was used as an excitation source.

7.3 Results and Discussion

Figure 7.1 (a) shows the XRD patterns of the $\text{Ca}_3(\text{PO}_4)_2:\text{Gd}^{3+},\text{Pr}^{3+}$ prepared using different amounts of urea after annealing in air at 1000°C . The patterns are consistent with the standard rhombohedral phase of $\text{Ca}_3(\text{PO}_4)_2$ referenced in JCPDS Card No. 70-2065. Nagpure et al obtained $\beta\text{-Ca}_3(\text{PO}_4)_2:\text{Tb}$ phosphor with a rhombohedral structure at a much lower synthesized temperature by using the sol-gel combustion method [8]. A complete transformation to pure $\beta\text{-Ca}_3(\text{PO}_4)_2$ occurs when the calcining temperature reaches 900°C or above [9]. There are two peaks at low masses of urea (0.5 and 1 g) observed at $2\theta = \sim 27$ and 29° marked with asterisks (*) and these are indicative of the presence of secondary phases most probably from unreacted $\text{Ca}(\text{NO}_3)_2$ precursor forming CaO or $\text{Ca}(\text{OH})_2$. This clearly shows that the amount of fuel plays an important role in the formation of pure $\text{Ca}_3(\text{PO}_4)_2$. The crystal structure was not affected when the amount of urea was increased from 4 to 10 g, the crystallinity and the width of the diffraction peaks were influenced by the increase in the amount of urea. The average crystallite size calculated using the Scherrer equation at different urea masses was in the range of $\sim 60\text{-}120$ nm. As shown in Figure 7.1 (b) the full width at half maximum (FWHM) reflection is decreasing with an increasing amount of urea, suggesting that the phosphor powder became more crystalline with an increasing amount of urea. Figure 7.2 shows the schematic arrangements of Ca, P and O crystal structure that was drawn using the diamond crystal software by using the data from Ref. [10]. There are two distinct sites for Ca^{2+} in the unit cell designated as Ca (1) and Ca (2). The Ca^{2+} is surrounded by O^{2-} in the hexagonal arrangement and the P^{5+} is surrounded by O^{2-} ions in the tetrahedral arrangements [11].

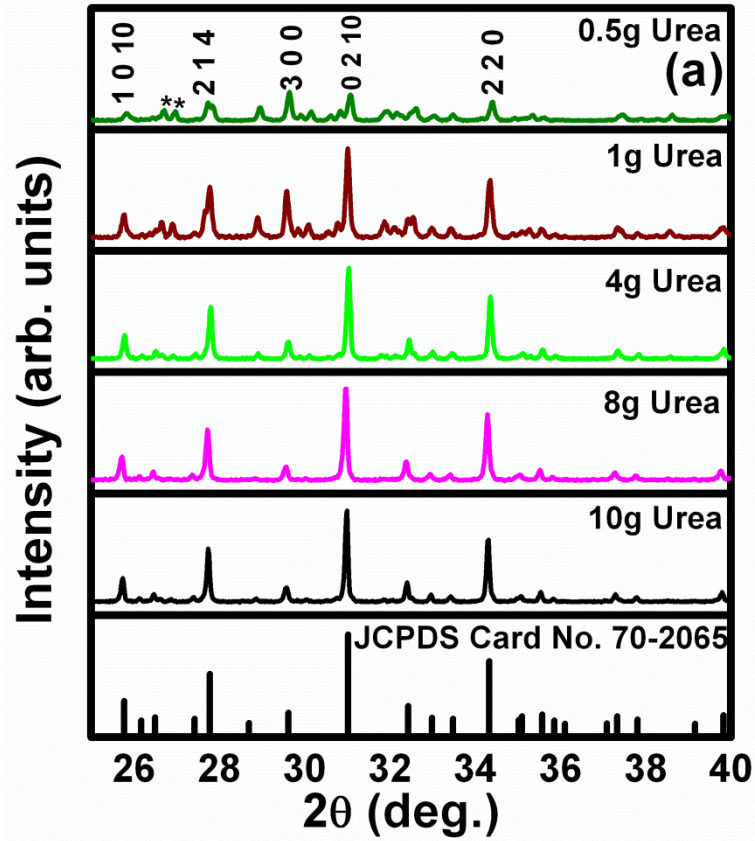


Figure 7.1 (a) XRD patterns $\text{Ca}_3(\text{PO}_4)_2:\text{Gd}^{3+},\text{Pr}^{3+}$ annealed at 1000 °C using various urea masses ranging from 0.5 – 10g.

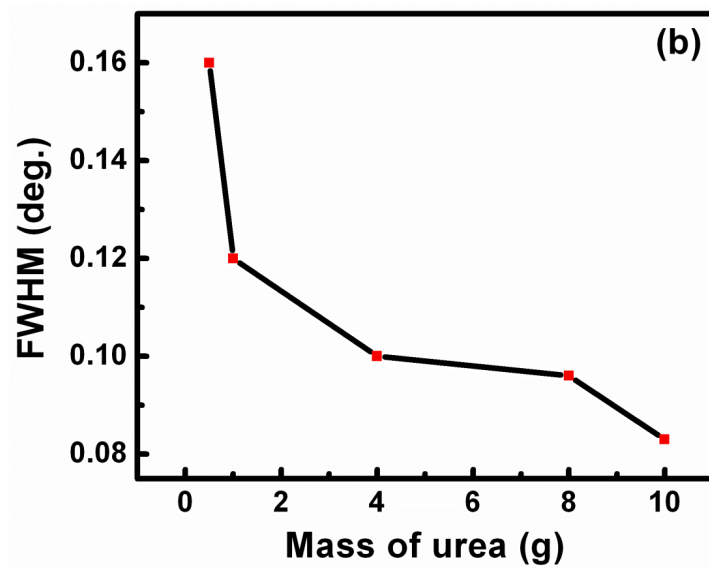


Figure 7.1 (b) Line broadening of $\text{Ca}_3(\text{PO}_4)_2:\text{Gd}^{3+},\text{Pr}^{3+}$ at various urea masses.

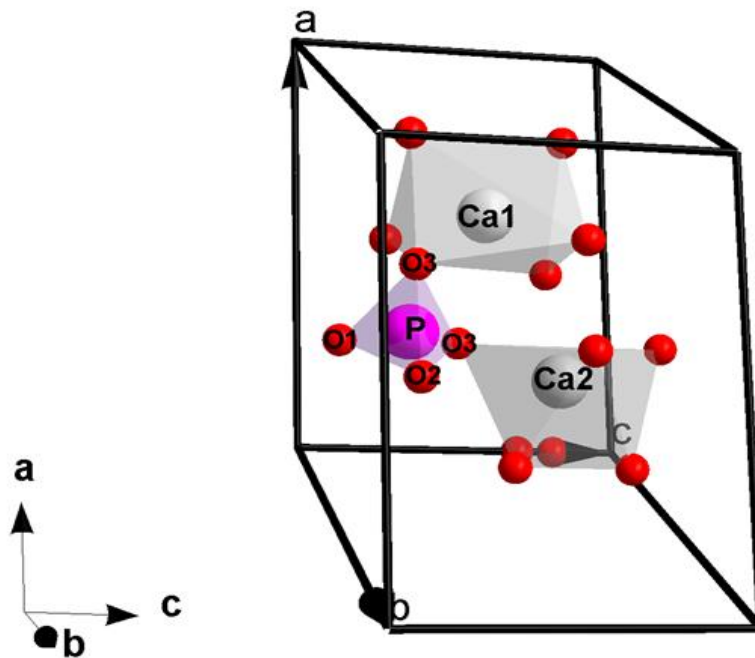


Figure 7.2 The $\text{Ca}_3(\text{PO}_4)_2$ unit cell described with a polyhedral (ICSD-99358)

Figure 7.3 shows the SEM images of (a) $\text{Ca}_3(\text{PO}_4)_2$, (b) $\text{Ca}_3(\text{PO}_4)_2:\text{Gd}^{3+}$ and $\text{Ca}_3(\text{PO}_4)_2:\text{Gd}^{3+},\text{Pr}^{3+}$ powder phosphor all prepared by 0.5g of urea. The particle morphology was certainly influenced by doping. The undoped $\text{Ca}_3(\text{PO}_4)_2$ powder composed of agglomerated nanoparticles. The shape changed from nanospheres to nanorods upon Gd^{3+} doping as shown in Figure 7.3 (b). A further change in particle morphology was observed upon Pr^{3+} co-doping as shown in figure 7.3 (c). Here the particles appear as slurry of non-uniform sheet with voids formed as a result of gases that escaped during the combustion process. The sheet is covered with multiple nanospheres, which are not evenly distributed on the surface.

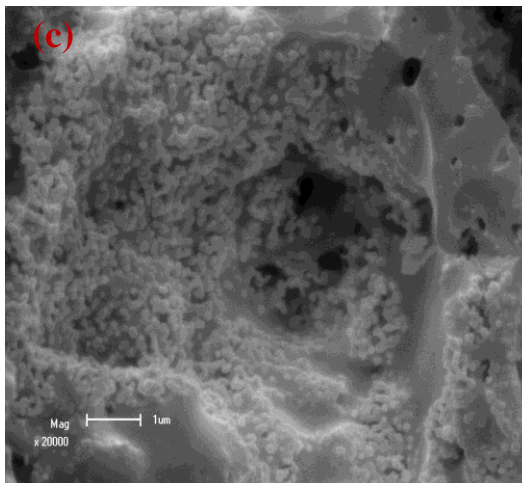
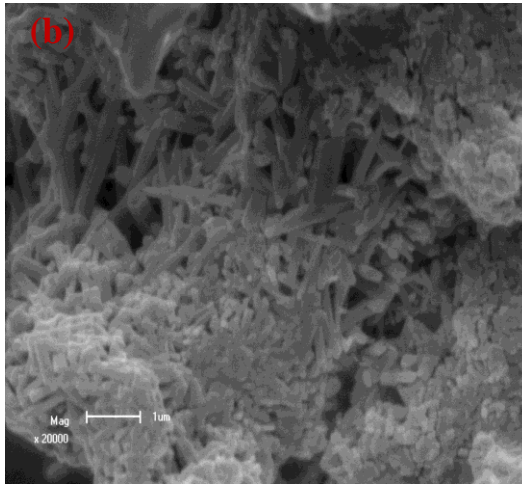
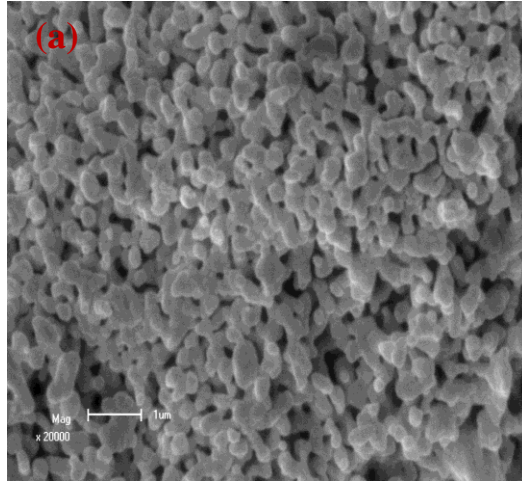


Figure 7.3 SEM images of (a) $\text{Ca}_3(\text{PO}_4)_2$, (b) $\text{Ca}_3(\text{PO}_4)_2:\text{Gd}^{3+}$ and (c) $\text{Ca}_3(\text{PO}_4)_2:\text{Gd}^{3+},\text{Pr}^{3+}$ phosphor powder obtained after annealing at 1000 °C in air.

Figure 7.4 shows the compositional identification of $\text{Ca}_3(\text{PO}_4)_2:\text{Gd}^{3+},\text{Pr}^{3+}$ for both negative and positive ions using TOF-SIMS. The material ($\text{Ca}_3(\text{PO}_4)_2:\text{Gd}^{3+},\text{Pr}^{3+}$) was investigated to identify the presence of dopants and homogeneity of doping in the crystal lattice using TOF-SIMS. Secondary electrons emitted from the sample surface were used to count the number of incident primary ions in the SIMS analysis. Figures 7.4 (a) and (b) show the positive and negative ion mass spectra of $\text{Ca}_3(\text{PO}_4)_2:\text{Gd}^{3+},\text{Pr}^{3+}$. For positive polarity mode, the peaks were detected at $m/z = 39.96, 55.95, 56.94, 140.87, 156, 157.87, 173$ and 174.67 corresponding to $\text{Ca}^+, \text{CaO}^+, \text{CaOH}^+, \text{Pr}^+, \text{PrO}^+, \text{Gd}^+, \text{GdO}^+$ and GdOH^+ respectively. The $\text{CaO}^+, \text{PrO}^+$ and GdO^+ were probably formed as a result of oxidation of the $\text{Ca}^{2+}, \text{Pr}^{3+}$ and Gd^{3+} when the samples were annealed in air, while the CaOH^+ and GdOH^+ were probably formed as a result of the reaction between Ca^{2+} and Gd^{3+} with H_2O from the surrounding atmosphere. For negative polarity mode, the peaks were detected at $m/z = 12.00, 16.00, 17.00$ and 30.94 corresponding to $\text{C}^-, \text{O}^-, \text{OH}^-$ and P^- ions respectively. The OH^- and C^- are probably due to atmospheric moisture and hydrocarbons respectively. The high count rates of Ca^{2+} and O^- were recorded in the positive and negative polarity modes respectively, while the count rates of Pr^+, Gd^+ and P^- were comparatively low.

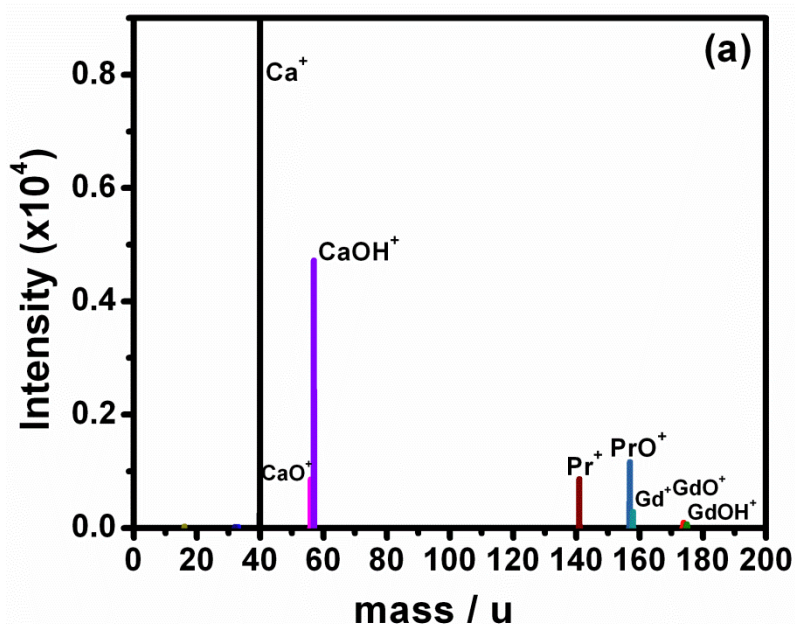


Figure 7.4 (a) Positive TOF-SIMS spectra of $\text{Ca}_3(\text{PO}_4)_2:\text{Gd}^{3+},\text{Pr}^{3+}$ phosphor powder.

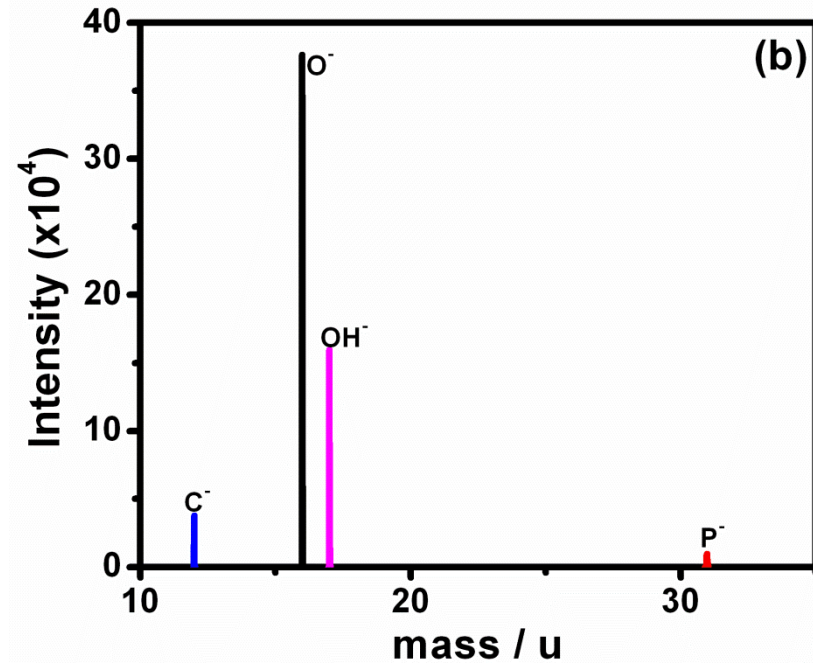


Figure 7.4 (b) negative TOF-SIMS spectra of $\text{Ca}_3(\text{PO}_4)_2:\text{Gd}^{3+},\text{Pr}^{3+}$ phosphor powder.

Figure 7.5 (a) and (b) shows the images of the $\text{Ca}_3(\text{PO}_4)_2:\text{Gd}^{3+},\text{Pr}^{3+}$ phosphor powder. Images were collected in both positive and negative ion modes. Images were not collected on the same position on the sample. The images show specific elemental topography of each ion distributed across the surface. All individual images are represented in a linear colour scale bar with the colours ranging from black – red - orange - yellow- white, where black corresponds to the zero counts and white to the maximum intensity (e.g. 14 counts for Ca^{2+}). The number underneath each image is the integrated intensity of the entire field of view (e.g. 4.73×10^4 counts for Ca^{2+}).

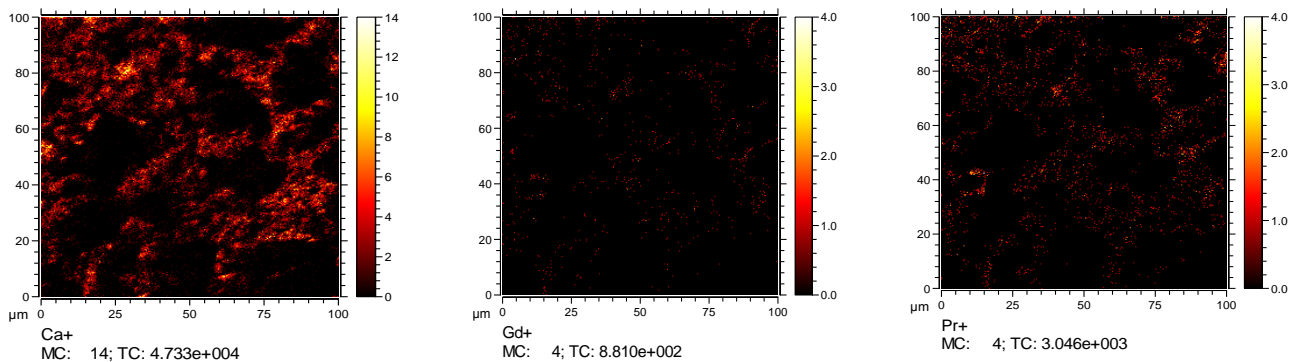


Figure 7.5 (a) TOF-SIMS chemical images of $\text{Ca}_3(\text{PO}_4)_2:\text{Gd}^{3+},\text{Pr}^{3+}$ phosphor powder for positive ion mode.

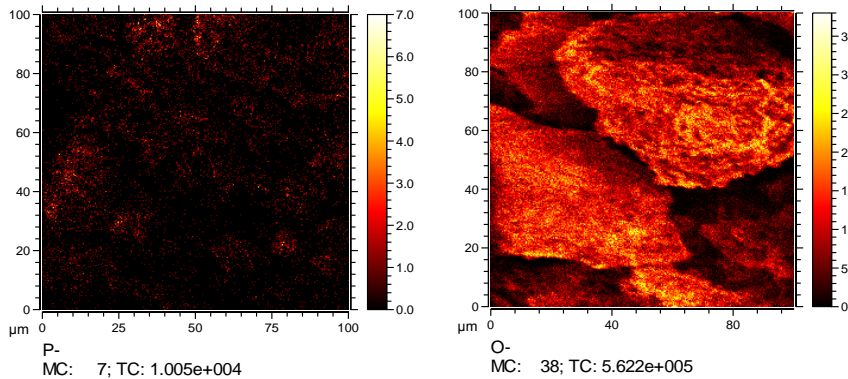


Figure 7.5 (b) TOF-SIMS chemical images of $\text{Ca}_3(\text{PO}_4)_2:\text{Gd}^{3+},\text{Pr}^{3+}$ phosphor powder for negative ion mode.

Figure 7.6 (a) shows the optical absorption spectra of pure $\text{Ca}_3(\text{PO}_4)_2$, single doped with Gd^{3+} and Pr^{3+} , co-doped with both Gd^{3+} and Pr^{3+} powder. The two major peaks at 230 and 285 nm are assigned to band to band absorptions and structural defects (e.g vacancies) in the host respectively [12]. The minor peaks 443 – 485 nm and 593 nm are assigned to ${}^3\text{H}_4 \rightarrow {}^3\text{P}_{(j=0,1,2)}$ and ${}^3\text{H}_4 \rightarrow {}^1\text{D}_2$ transition states of Pr^{3+} respectively. The bandgap of $\text{Ca}_3(\text{PO}_4)_2$ was estimated from the plot of $(\alpha h\nu)^2$ versus $h\nu$ shown in Figure 7.6 (b). For crystalline materials with a direct band gap the dependence of the absorption coefficient (α) on the frequency ν can be approximated by:

$$\alpha h\nu = A(h\nu - E_g)^{\frac{1}{2}} \quad (7.2)$$

where A is a proportional constant, h is Planck's constant and E_g is the bandgap energy. The band gap energy was estimated by extrapolating to zero a linear fit to the plot of $(\alpha h\nu)^2$ versus $h\nu$. The estimated E_g value was found to be 4.92 eV and it is similar to previously reported data with the energy gap of 4.5-5.4 eV [13, 14].

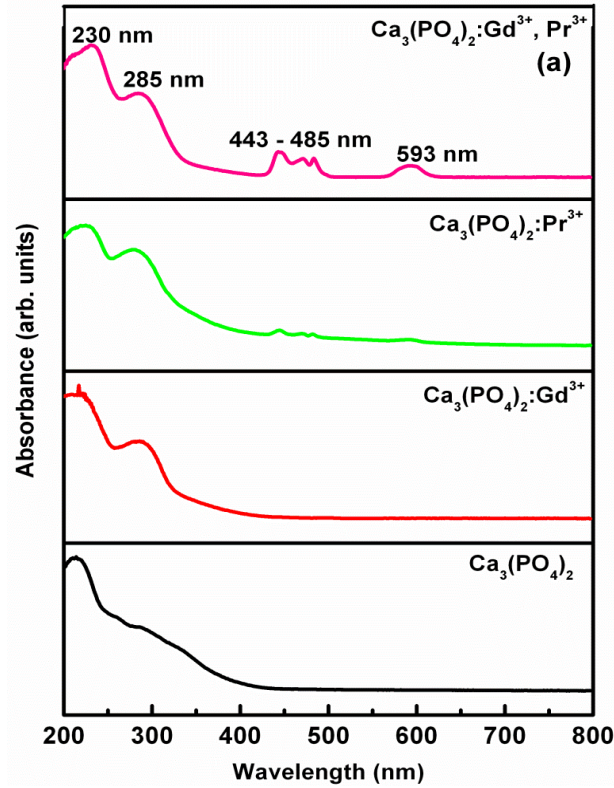


Figure 7.6 (a) Optical absorption spectra of $\text{Ca}_3(\text{PO}_4)_2:\text{Gd}^{3+}, \text{Pr}^{3+}$.

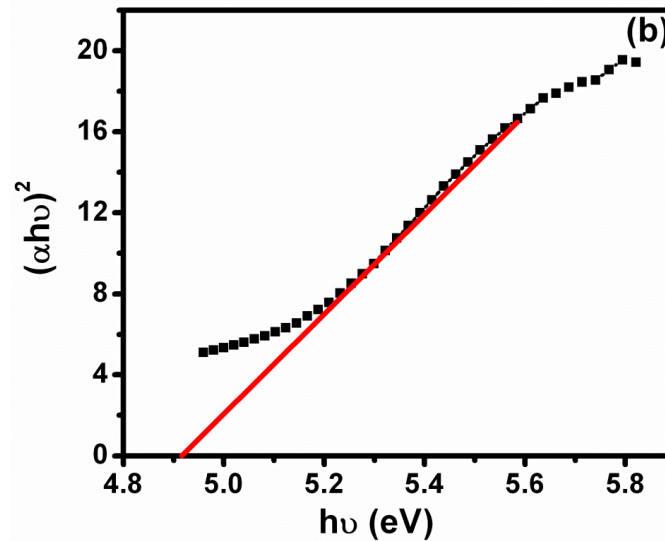


Figure 7.6 (b) $(\alpha h\nu)^2$ vs photon energy ($h\nu$) plot of $\text{Ca}_3(\text{PO}_4)_2:\text{Gd}^{3+}, \text{Pr}^{3+}$.

Figure 7.7 shows the PL (i) excitation and (ii) emission spectra of $\text{Ca}_3(\text{PO}_4)_2:\text{Gd}^{3+}$ with different concentrations of Gd^{3+} . The excitation peaks are assigned to $4f \rightarrow 4f$ intraconfiguration forbidden transitions of Gd^{3+} [15]. The relative excitation peaks were observed at 245 and 274 nm and

they are respectively assigned to the $^8S_{7/2} \rightarrow ^6D_j$ and $^8S_{7/2} \rightarrow ^6I_j$ intra $4f^7$ transitions of Gd^{3+} [16, 17]. The narrow line emission peak of Gd^{3+} at 313 nm was measured when the sample was excited at a wavelength of 274 nm and it is assigned to the $^6P_{7/2} \rightarrow ^8S_{7/2}$ transition of Gd^{3+} . The inset shows that the maximum intensity of the 313 nm was increasing with increasing concentration of Gd^{3+} from 0.1 to 10 mol%. The increase is non-linear and this can be attributed to, among other things, the coarseness and compactness of the powder in the sample holder and subsequently the penetration depth of the primary excitation source, and inhomogeneous distribution of the rare-earth dopant ions.

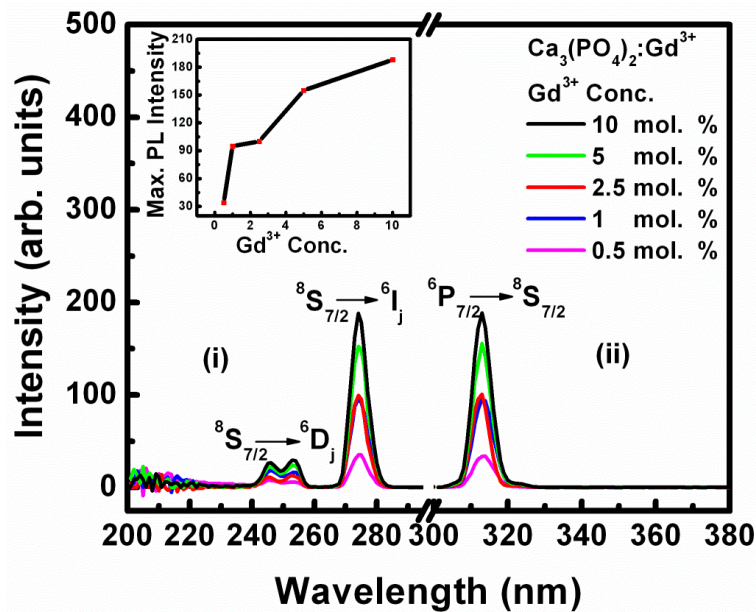


Figure 7.7 PL spectra of $Ca_3(PO_4)_2:Gd^{3+}$ (a) excitation ($\lambda_{emi} = 313$ nm) and (b) emission ($\lambda_{exc} = 274$ nm).

Figure 7.8 shows the PL (i) excitation and (ii) emission spectra of $Ca_3(PO_4)_2:Pr^{3+}$ calcined at $1000^\circ C$. The excitation spectrum was measured when monitoring the red emission from Pr^{3+} at 603 nm and it consists of narrow line excitation peaks in the visible and a broadband excitation peak in the ultraviolet (UV) region at 300 nm (4.13 eV). The narrow line excitation peaks are assigned to Laporte forbidden $4f \rightarrow 4f$ (i.e. $^3H_4 \rightarrow ^3P_{0,1,2}$) transitions of Pr^{3+} while the UV excitation band could be due to band-to-band transition of the host lattice or $4f \rightarrow 4f5d$ transitions of Pr^{3+} or charge transfer states (CTS) [18]. To be able to assign this excitation it is important to locate the lowest excitation state of the $4f5d$ band of Pr^{3+} relative to the bandgap energy of the $Ca_3(PO_4)_2$

host. In the free Pr^{3+} ion, the lowest energy state of the $4f5d$ band is located around 7.4 eV ($60\,000\text{ cm}^{-1}$) [19], but this energy can be downshifted to energies lower than $40\,000\text{ cm}^{-1}$ by the nephelauxetic effect and the crystal field splitting in the solid state crystals where the bond covalency and the crystal field strength are very effective [18]. The UV excitation band at 4.13 eV (33333 cm^{-1}) is too low to be assigned to $\text{Ca}_3(\text{PO}_4)_2$ band-to-band transition with the bandgap energy of 4.92 eV or to direct $4f \rightarrow 4f5d$ transition with the lowest excitation energy state located at 7.4 eV. Therefore we propose to assign the UV band excitation in figure 7.8 to the $\text{O}^{2-} \rightarrow \text{Pr}^{3+}$ in the intervalence charge transfer (IVCT) states. This kind of transition involves a spatial change in the electron charge density that can be interpreted as the energy required promoting an electron from the valence band (composed mainly of the ligand orbitals) of the host to the trivalent rare-earth ion (Pr^{3+}) [20].

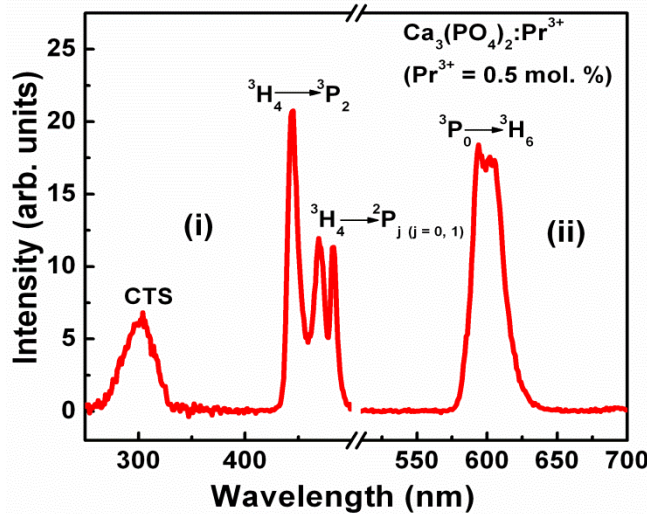


Figure 7.8 PL spectra of $\text{Ca}_3(\text{PO}_4)_2:\text{Pr}^{3+}$ (a) excitation ($\lambda_{\text{emi}} = 603\text{ nm}$) and (b) emission ($\lambda_{\text{exc}} = 444\text{ nm}$).

Figure 7.9 (a) shows PL excitation and emission of $\text{Ca}_3(\text{PO}_4)_2:\text{Gd}^{3+},\text{Pr}^{3+}$ powder phosphor prepared at different concentrations annealed at $1000\text{ }^\circ\text{C}$. The PL excitation spectra consist of narrow peak from Gd^{3+} situated at 275 nm and a broadband at 222 nm assigned to Pr^{3+} . The intensity at maximum intensity of the 313 nm peak was increasing with increasing concentration of Pr^{3+} . Figure 7.9 (a) (ii) shows the PL emission spectra of $\text{Ca}_3(\text{PO}_4)_2:\text{Gd}^{3+},\text{Pr}^{3+}$ when excited with the wavelength of 222 nm. The spectra show only the emission peak at 313 nm corresponding to the ${}^8\text{S}_{7/2} \rightarrow {}^6\text{G}_j$ transitions of Gd^{3+} . The excitation spectrum of Gd^{3+} consists

only of f-f transition of Gd^{3+} as shown earlier (Figure 7.7). Upon Pr^{3+} co-doping a new broad and intense excitation peak developed at the wavelength of 227 nm (5.46 eV or 44052 cm^{-1}). This peak is blue shifted by 73 nm from $Pr^{3+} \rightarrow O^{2-}$ CTS peak observed in figure 7.8 and it is also more intense than the CTS peak. Although this peak is very close to the 230 nm peak assigned to the band-to-band absorption of the host in the UV-vis spectrum shown in figure 7.6, it cannot be assigned to the band-to-band excitation of the host because neither the undoped nor the Gd^{3+} single doped host could be excited by the monochromatized xenon lamp. It is therefore reasonable to assign this excitation band to the $4f \rightarrow 4f5d$ transition of Pr^{3+} . Although our observed location of the $4f5d$ band is 15948 cm^{-1} less than the predicted lowest energy (60000 cm^{-1}) of the excited level of the $4f5d$ band in pure Pr^{3+} ion, it is consistent with the predicted location of the $4f5d$ band of Pr^{3+} in different inorganic solid hosts [21].

Figure 7.9 (b) compares the PL excitation and emission spectra of Gd^{3+} single doped and Gd^{3+} - Pr^{3+} co-doped $Ca_3(PO_4)_2$ powder phosphors both annealed at $1000\text{ }^\circ\text{C}$. The PL emission spectra ($\lambda_{exc} = 227\text{ nm}$) of $Ca_3(PO_4)_2:Gd^{3+},Pr^{3+}$ show a single intense narrow line peak at 313 nm. This peak is $4\times$ more intense than the same peak observed from the Gd^{3+} single doped $Ca_3(PO_4)_2$. This result shows that Pr^{3+} is a good sensitizer of the 313 nm UVB emission of Gd^{3+} . In other words, Pr^{3+} acts to harvest excitation energy and transfer it non-radiatively to Gd^{3+} . Possible mechanism of energy transfer from the excited $4f5d$ states of Pr^{3+} to Gd^{3+} in the $Ca_3(PO_4)_2$ host is shown in figure 7.9 (c). According to this mechanism, the excitation of electrons from the 3H_4 ground state to the excited $4f5d$ energy states of Pr^{3+} is followed by non-radiative energy transfer to Gd^{3+} . The fact that the red emission from Pr^{3+} at 603 nm was quenched in the Gd^{3+} - Pr^{3+} co-doped $Ca_3(PO_4)_2$ suggests that the rate of energy transfer from the $4f5d$ energy states of Pr^{3+} to Gd^{3+} was faster than the radiative transition to the 3H_4 ground state.

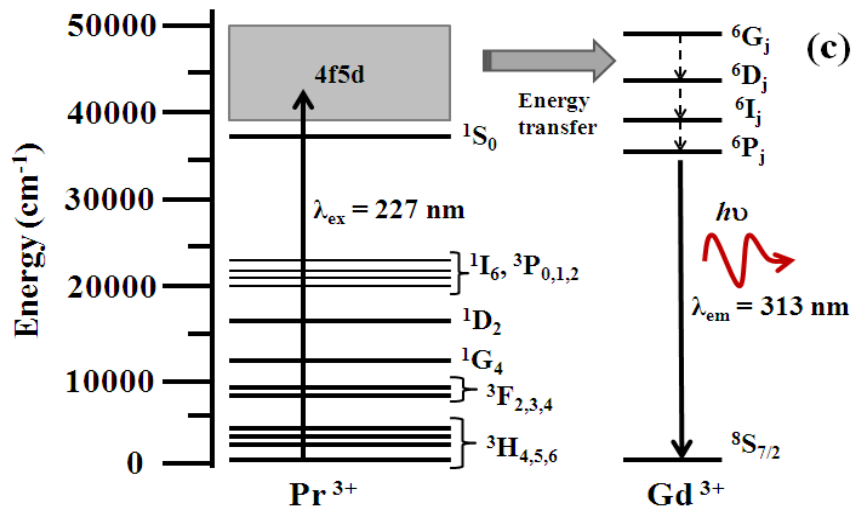
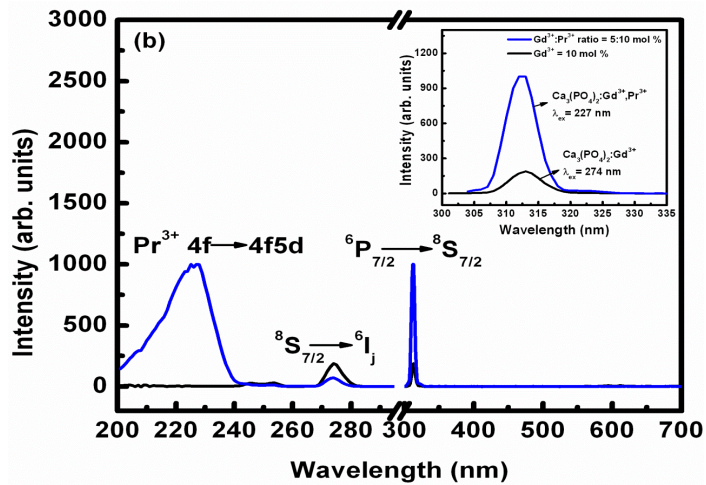
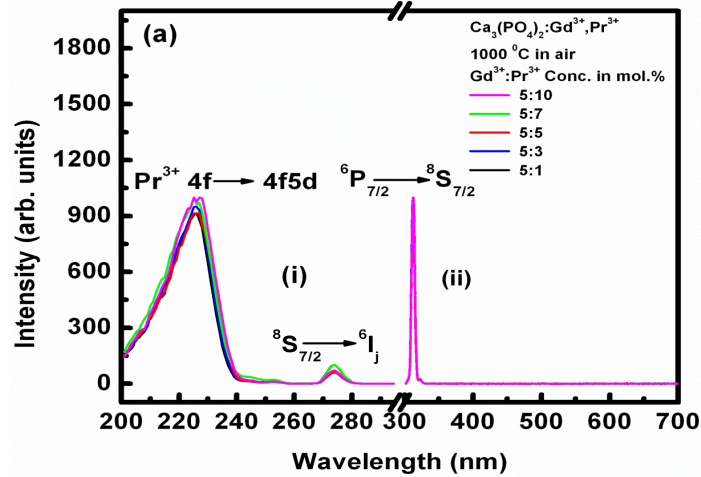


Figure 7.9 PL(a) excitation and emission spectra of $\text{Ca}_3(\text{PO}_4)_2:\text{Gd}^{3+},\text{Pr}^{3+}$ powder phosphor, (b) comparison between PL excitation and emission spectra of Gd^{3+} single doped and $\text{Gd}^{3+}\text{-Pr}^{3+}$ co-doped $\text{Ca}_3(\text{PO}_4)_2$ powder phosphors (c) simplified energy transfer mechanism for Pr^{3+} - Gd^{3+} system.

7.4 Conclusion

$\text{Ca}_3(\text{PO}_4)_2:\text{Gd}^{3+},\text{Pr}^{3+}$ phosphor powders were successfully synthesized by a combustion method with urea as a fuel. The average crystallite size calculated using the Scherrer equation at different urea masses was in the range of ~60-120 nm. The surface morphologies of the powders were studied by SEM. The powders showed up spherical, rod-like and clustered small spherical particles for $\text{Ca}_3(\text{PO}_4)_2$, $\text{Ca}_3(\text{PO}_4)_2:\text{Gd}^{3+}$ and $\text{Ca}_3(\text{PO}_4)_2:\text{Gd}^{3+},\text{Pr}^{3+}$ powders respectively. Luminescent properties of $\text{Ca}_3(\text{PO}_4)_2:\text{Gd}^{3+},\text{Pr}^{3+}$ under UV excitation have been investigated. $\text{Ca}_3(\text{PO}_4)_2:\text{Gd}^{3+},\text{Pr}^{3+}$ emits at 313 nm and the intensity is enhanced than in the $\text{Ca}_3(\text{PO}_4)_2:\text{Gd}^{3+}$ system. The UV emission makes $\text{Ca}_3(\text{PO}_4)_2:\text{Gd}^{3+},\text{Pr}^{3+}$ phosphor a good candidate for applications in phototherapy lamps.

References

- [1] N. S. Vedeanu, D. A. Magdas, *J. Alloys Comp.*, 2012, **534**, 93-96
- [2] X. Yin, M. Stott, *Phys. Rev. B*, 2003, **68**, 2052051-2052058
- [3] K. Nakashima, J. Yamauchi, *J. Alloys Comp.*, 2006, **408-412**, 761-765
- [4] B. Mirhadi, B. Mehdikhani, N. Askari, *Process. Appl. Ceram.*, 2011, **5**, 193-198
- [5] K. Lin, J. Chang, J. Lu, W. Wu, Y. Zeng, *Ceram. Int.*, 2007, **33**, 979-985
- [6] K. Madhukumar, H. K. Varma, M. Komath, T. S. Elias, V. Padmanabhan, C. M. K. Nair, *Bull. Mater. Sci.*, 2007, **30**, 527-534
- [7] J. Zhang, J. Guo, S. Li, B. Song, K. Yao, *Front. Chem. China*, 2008, **3**[4], 451-453
- [8] I.M. Nagpure, S.S. Pitale, E. Coetsee, O.M. Ntwaeaborwa, J.J. Terblans, H.C. Swart, *Opt. Mater.*, 2012, **34**, 1398-1405
- [9] C. Zou, K. Cheng, W. Weng, C. Song, P. Du, G. Shen, G. Han, *J. Alloys Comp.*, 2011, **509**, 6852-6858
- [10] M. Marezio, J. P. Remeika, P. D. Dernier, *Acta Crystallographica*, 1968, **24**, 1670 (ICSD-29248)
- [11] X. Yin, M.J. Stott, *Phy. Rev. B*, 2003, **68**, 205205-8
- [12] Y.C. Li, Y.H. Chang, Y.S. Chang, Y.J. Lin, C.H. Laing, *J. Phys. Chem. C*, 2007, **111**, 10682-10688
- [13] A. Mitsionis, T. Vaimakis, C. Trapalis, N. Todorova, D. Bahnemann, R Dillert, *Appl. Catal. B*, 2011, **106**, 398-404.
- [14] T. Mineharu, W. Masato, Y. Naoya, W. Toshiya, *J. Mol. Catal. A*, 2011, **338**, 18-23
- [15] A. Richter, E. Heumann, G. Huber, *Opt. Express*, 2007, **15**, 5172-5178
- [16] F. Du, R. Zhu, Y. Huang, Y. Tao, H. Jin Seo, *Dalton Trans.*, 2011, **40**, 11433-11440
- [17] J. Zhong, H. Liang, Q. Su, J. Zhou, Y. Huang, Z. Gao, Y. Tao, J. Wang, *Appl. Phys. B*, 2010, **98**, 139-147
- [18] K. Le Bris, C. Reber, *J. Alloys and Comp.*, 2006, **424**, 237-242
- [19] P. Boutinaud, M. Bettinelli, F. Diaz, *Opt. Mater.*, 2010, **32**, 1659-1663

- [20] S.S. Pitale, S.K. Sharma, R.N. Dubey, M.S. Quresh, M. M. Malik, *Opt. Mater.*, 2009, **31**, 923-932
- [21] Q.Y. Zhang, X.Y. Huang, *Prog. Mater. Sci.*, 2010, **55**, 353-427

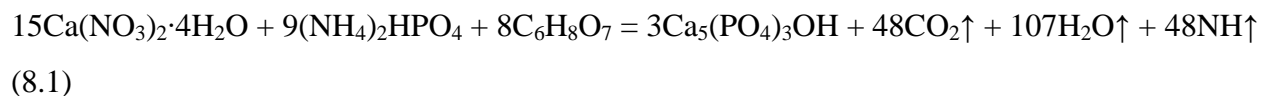
Chapter 8: Luminescent properties of $\text{Ca}_5(\text{PO}_4)_3\text{OH}:\text{Gd}^{3+},\text{Pr}^{3+}$ phosphor powder prepared by citrate-gel combustion method

8.1 Introduction

The citric acid method is one kind of non-alkoxide sol-gel method which is an efficient method to prepare nanocrystalline materials. It is a complex process, which cannot be described by only one chemical reaction. The whole process may consist of several reactions, which occur either between the citrate and the reactant nitrates or between the decomposition products arising from both citrate and nitrate [1]. The attractive features of this method are its ability to produce materials with high purity, better homogeneity, and high surface area in a single step and lower synthesis temperature. Nitrate-citrate gel combustion exhibits self-propagating combustion behaviour. After combustion, the gel directly transform into single phase crystal. This process is less complicated, inexpensive, and highly reactive when compared to other synthesis technique [2]. The synthesis procedure involves the heating of amorphous citrate precursor containing cations and anions to get rid of compounds having peculiar morphology and sintering characteristics. The product derived by this technique consists of a large number of pores resulting from the evolution of gases produced during the decomposition of the amorphous precursor materials [3]. In this investigation, the citric acid sol-gel combustion method was adapted to synthesize nanocrystalline hydroxyapatite ($\text{Ca}_5(\text{PO}_4)_3\text{OH}$ or HA) co-doped with gadolinium and praseodymium resulting in a phosphor that emits UVB radiation at 311 nm that is suitable for application in phototherapy lamps.

8.2 Experimental

The starting materials used were $\text{Ca}(\text{NO}_3)_2 \cdot 4\text{H}_2\text{O}$, $(\text{NH}_4)_2\text{HPO}_4$, $\text{Gd}(\text{NO}_3)_3 \cdot 5\text{H}_2\text{O}$, $\text{Pr}(\text{NO}_3)_3 \cdot 6\text{H}_2\text{O}$ and $\text{C}_6\text{H}_8\text{O}_7 \cdot 4\text{H}_2\text{O}$. The gel was prepared according to the following reaction equation:



The reactants in stoichiometric amount according to Eq (5.1) were dissolved together in 2 ml of distilled water resulting in a white solution. The solution was heated under continuous stirring at 80 °C for 3 hours. Slowly the solution solidified to form a gel as water evaporated and gases evolved. The gel was subsequently dried at 100 °C for 6 hours to yield a xerogel. The xerogel was calcined at 850 °C for 2 hours in a furnace. The produced materials were $\text{Ca}_5(\text{PO}_4)_3\text{OH}$, $\text{Ca}_5(\text{PO}_4)_3\text{OH}:\text{Gd}^{3+}$, $\text{Ca}_5(\text{PO}_4)_3\text{OH}:\text{Pr}^{3+}$ and $\text{Ca}_5(\text{PO}_4)_3\text{OH}:\text{Gd}^{3+},\text{Pr}^{3+}$ phosphor powders with different concentrations of Gd^{3+} and Pr^{3+} .

The structure and crystallinity of the phosphors were analyzed using an XRD. Particle morphology were examined using Jeol JSM-7800F thermal field emission SEM coupled with Oxford Aztec 350 X-Max80 EDS, that was used to analyse the chemical composition of the phosphors. PL data were recorded using Cary Eclipse spectrophotometer at room temperature using a Varian Cary Eclipse fluorescence spectrophotometer coupled with a monochromatized xenon lamp with an output power of (60-75W).

8.3 Results and Discussion

Figure 8.1 shows the XRD patterns of the gel-combustion $\text{Ca}_5(\text{PO}_4)_3\text{OH}:\text{Gd}^{3+},\text{Pr}^{3+}$ annealed at 850 °C in air. The patterns are consisted with the standard hexagonal phase of $\text{Ca}_5(\text{PO}_4)_3\text{OH}$ referenced in JCPDS Card No. 73-0293. The estimated average crystallite size calculated by Scherrer equation was ~ 45 nm. The sharp peaks suggested that the powder was crystalline.

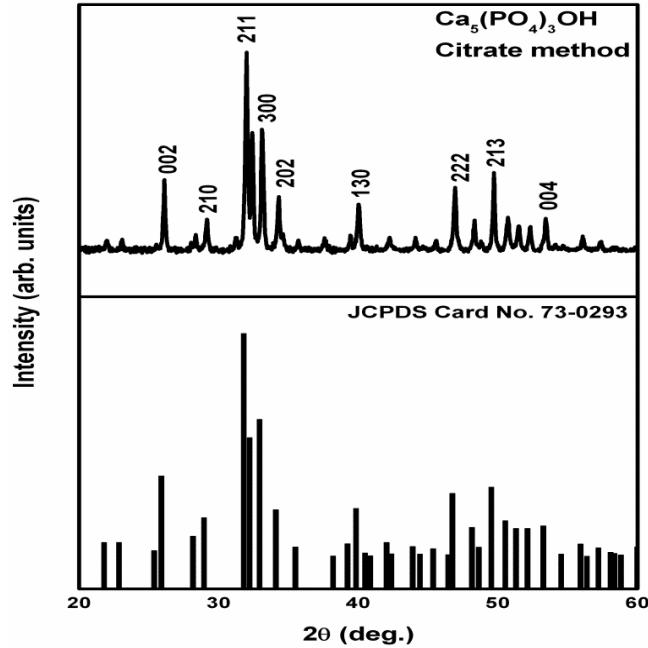


Figure 8.1 XRD patterns of $\text{Ca}_5(\text{PO}_4)_3\text{OH}$ annealed at 850 °C in air furnace.

Figure 8.2 (a – c) shows the high resolution SEM images of $\text{Ca}_5(\text{PO}_4)_3\text{OH}:\text{Gd}^{3+}, \text{Pr}^{3+}$ powder calcined at 850 °C for 2 hours. The powder consisted of smaller and bigger particles. The smaller particles were spherical but faceted and were inhomogeneously distributed on the surface of dark bigger particles which were agglomerated together and did not have any regular shapes. There are some micropores which were probably due to gases that evolved during the chemical reaction. The EDS spectra taken at two different positions (marked 4 and 5) in figure 8.2 (b) are plotted in figure 8.2 (c) and they confirm the presence of all elements in our materials.

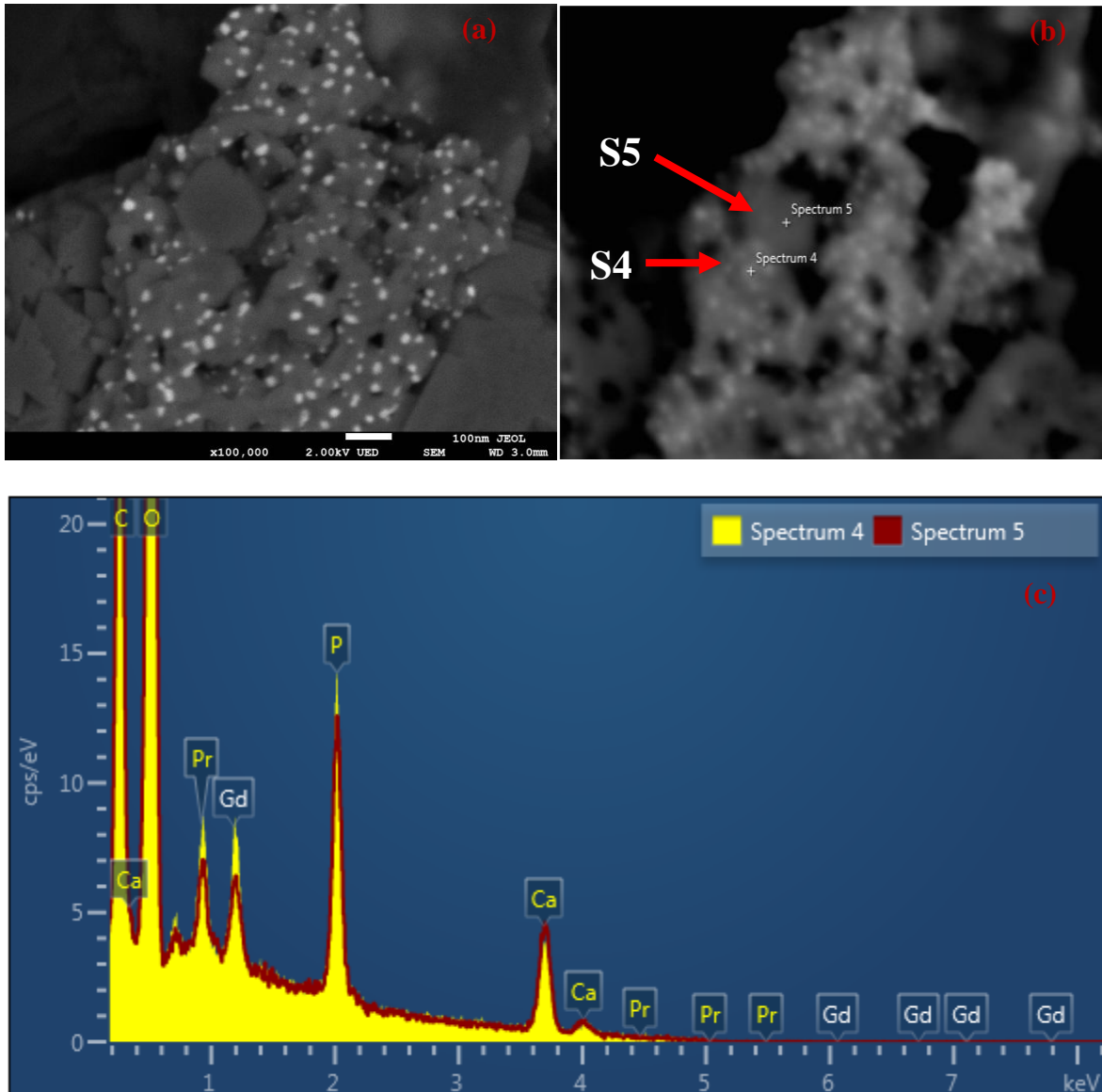


Figure 8.2 (a-b) SEM images and (c) EDS spectrum of $\text{Ca}_5(\text{PO}_4)_3\text{OH}:\text{Gd}^{3+},\text{Pr}^{3+}$ phosphor powder calcined at $850\text{ }^\circ\text{C}$ for 2 hours.

Figure 8.3 shows the PL (i) excitation and (ii) emission spectra of $\text{Ca}_5(\text{PO}_4)_3(\text{OH}):\text{Gd}^{3+}$ prepared at different concentrations of Gd^{3+} . The two excitation peaks are observed at 245 and 275 nm assigned to the transitions from $^8\text{S}_{7/2}$ to excited state $^6\text{D}_j$ and $^6\text{I}_j$ intra $4f^7$ transition of Gd^{3+} ion, respectively [4]. The strong and narrow emission peak is observed at 313 nm which is assigned to $^6\text{P}_{7/2} \rightarrow ^8\text{S}_{7/2}$ electronic transition of Gd^{3+} ion [5]. The peaks are assigned to $4f \rightarrow 4f$ intraconfiguration forbidden transitions of Gd^{3+} ion [6]. The inset shows that the intensity of the peaks increases with concentration of Gd^{3+} from 0.5 – 10 mol %. No wavelength shift or peak for a new site was observed at high Gd^{3+} concentrations.

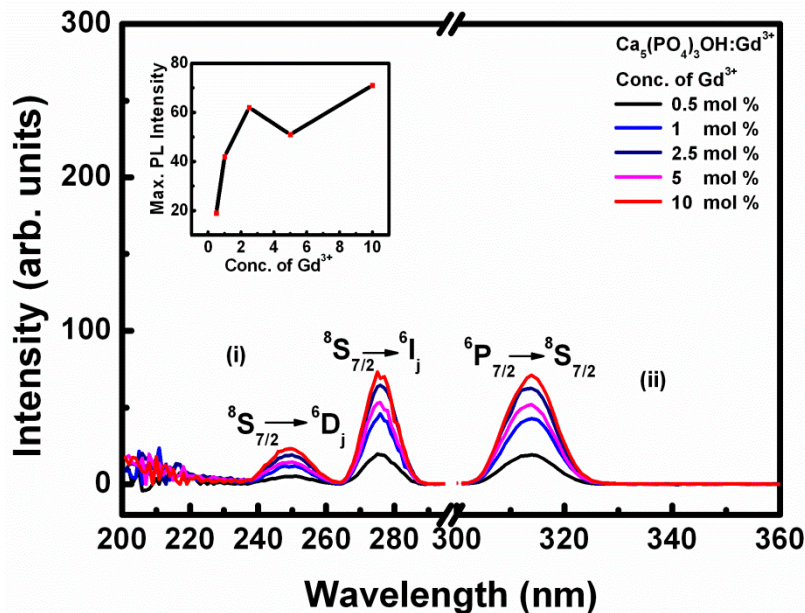


Figure 8.3 PL spectra of $\text{Ca}_5(\text{PO}_4)_3\text{OH}:\text{Gd}^{3+}$ phosphor annealed at 850 °C in air.

Figure 8.4 presents (i) excitation and (ii) emission spectra of $\text{Ca}_5(\text{PO}_4)_3\text{OH}:\text{Gd}^{3+},\text{Pr}^{3+}$ phosphor powders calcined at 850 °C. Figure 8.4 (i) shows weak excitation peak at 274 nm is attributed to ${}^8\text{S}_{7/2} \rightarrow {}^6\text{I}_j$ transition of Gd^{3+} ion. Upon co-doping with Pr^{3+} , the broad excitation peak is observed at 222 nm assigned to $4f \rightarrow 4f5d$ transition of Pr^{3+} ion. The mechanism behind the Pr^{3+} transitions absorbing at 222 nm is explained in chapter 5. The PL emission spectra observed in figure 8.4 (ii) shows a single intense narrow line peak at 313 nm assigned to the ${}^6\text{P}_{7/2} \rightarrow {}^8\text{S}_{7/2}$ transition of Gd^{3+} . This peak is more intense than the same peak observed from the Gd^{3+} single doped $\text{Ca}_3(\text{PO}_4)_2$. The absorbed energy by Pr^{3+} at 222 nm is transferred to Gd^{3+} which results in an enhanced Gd^{3+} emission at 313 nm in the UV region. The energy transfer mechanism is explained in chapter 6. The inset shows that the maximum intensity of the 313 nm attained at mole ratio concentration of 5:1 mol. %. The intensity is decreasing with increase in Pr^{3+} concentration suggesting that this emission is sensitive to concentration quenching effects.

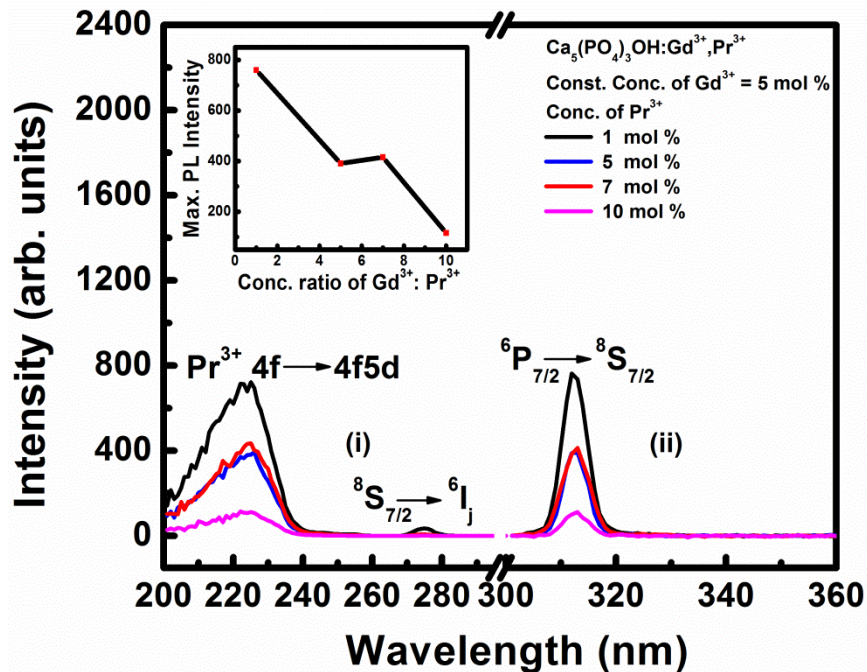


Figure 8.4 PL spectra of Ca₅(PO₄)₃OH:Gd³⁺,Pr³⁺ phosphor powders annealed at 850 °C in air.

8.4 Conclusion

Ca₅(PO₄)₃OH:Gd³⁺,Pr³⁺ phosphor was successfully synthesized via citrate-gel combustion method which was confirmed by XRD analyses. Luminescent properties of Ca₅(PO₄)₃OH:Gd³⁺,Pr³⁺ under UV excitation have been investigated. Ca₅(PO₄)₃OH:Gd³⁺,Pr³⁺ emits at 313 nm and the intensity is more intense than UVB phosphor in Ca₅(PO₄)₃OH:Gd³⁺ system. The UVB emission makes it good candidate phosphors for application in phototherapy lamps.

References

- [1] S.S. Pitale, G. Mukut, I.M. Nagpure, O.M. Ntwaeaborwa, B.C.B. Bezuidenhoudt, H.C. Swart, *Physica B*, 2012, **407**, 1458-1488
- [2] Z. Yue, J. Zhou, L. Li, H. Zhang, Z.J. Gui, *Magn. Magn. Mater.*, 2000, **208**, 55-60
- [3] H.K. Varma, S.B. Suresh, *Ceram. Int.*, 2005, **31**, 109-114
- [4] J. Zhong, H. Liang, Q. Su, J. Zhou, Y. Huang, Z. Gao, Y. Tao, J. Wang, *Applied Physics B*, 2010, **98**, 139-147
- [5] K. Srinivasulu, I. Omkaram, H. Obeid, S.A Kumar, J.L. Ra, *J. Mol. Struct.*, 2013, **1036**, 63-70
- [6] M. Sreenivasulu, A.S. Rao, *J. Mater. Sci. Lett*, 2001, **20**, 737-740

Chapter 9: Luminescent properties, particle morphology and chemical composition of $\text{Ca}_3(\text{PO}_4)_2:\text{Gd}^{3+},\text{Pr}^{3+}$ powder phosphor prepared by microwave assisted synthesis method

9.1 Introduction

Microwave-assisted method synthesis has been well known since 1986 [1]. It has shown the broad applications as an efficient way to many organic reactions, producing high yields. Recently, it has been used as a tool in order to diminish reaction time with an improvement in the yield and quality of the product, avoids side products, and simplifies the course of reactions for combinatorial chemistry [2]. Microwave synthesis uses the electromagnetic waves ranging from 0.01 to 1m and wave length of certain frequency to generate heat in the material. Microwave synthesis provide great advantages such as rapid uniformity of heating, low operating cost, selective dielectric heating, high reaction rate, and low energy consumption [4]. However, overheating can lead to product substrate and reagent decomposition [3]. In this study, ultrasound–assisted microwave method was used to synthesize $\text{Ca}_3(\text{PO}_4)_2$ co-doped with Gd^{3+} and Pr^{3+} powder phosphors.

9.2 Experimental

Gd^{3+} and Pr^{3+} co-doped $\text{Ca}_3(\text{PO}_4)_2$ samples were synthesized by microwave assisted method. $\text{Ca}(\text{NO}_3)_2 \cdot 4\text{H}_2\text{O}$, $(\text{NH}_4)_2\text{HPO}_4$, $\text{Gd}(\text{NO}_3)_3 \cdot 5\text{H}_2\text{O}$, $\text{Pr}(\text{NO}_3)_3 \cdot 6\text{H}_2\text{O}$ were used as precursors. The materials were mixed stoichiometrically according to the following reaction equation:



In a typical experiment, 1.05M of $\text{Ca}(\text{NO}_3)_2 \cdot 4\text{H}_2\text{O}$ was dissolved in deionized water (12 mL), then an aqueous solution (10 mL) containing 0.85M $(\text{NH}_4)_2\text{HPO}_4$ was added dropwise to the above solution under magnetic stirring at room temperature, and the pH value was maintained at 8.5 by slow addition of a solution of 1M NaOH. The resulting solution was loaded into a 40 mL glass reactor, sealed and transferred to a microwave oven (CEM microwave, Model: discover-sp w/activent, USA) at 150 °C and 300 watt and was maintained at this condition for 1 hour, and then cooled down to room temperature naturally. The materials synthesized were $\text{Ca}_3(\text{PO}_4)_2$, $\text{Ca}_3(\text{PO}_4)_2:\text{Gd}^{3+}$ and $\text{Ca}_3(\text{PO}_4)_2:\text{Gd}^{3+},\text{Pr}^{3+}$ with different concentrations of Gd^{3+} and Pr^{3+} .

9.3 Results and Discussion

The XRD pattern of the $\text{Ca}_3(\text{PO}_4)_2$ powder calcined at 1000 °C in air is shown in figure 9.1. The pattern exhibits sharp diffraction peaks indicating high crystallinity. The pattern show well resolved peaks of $\text{Ca}_3(\text{PO}_4)_2$ indexed according to standard data (JCPDS Card No. 70-2065) and it consistent with standard rhombohedral phase of $\text{Ca}_3(\text{PO}_4)_2$ [5]. The small extra peaks observed in between the indexed peaks may be due to unreacted precursors during the measurements forming the second phase. The average crystallite size was calculated by means of X-ray line broadening method using the Scherrer equation. The strongest peaks used to calculate sizes were $2\theta = 25.97^\circ$, 28.00° , 31.19° and 34.49° . The estimated average crystallite size of the phosphor was found to be ~76 nm.

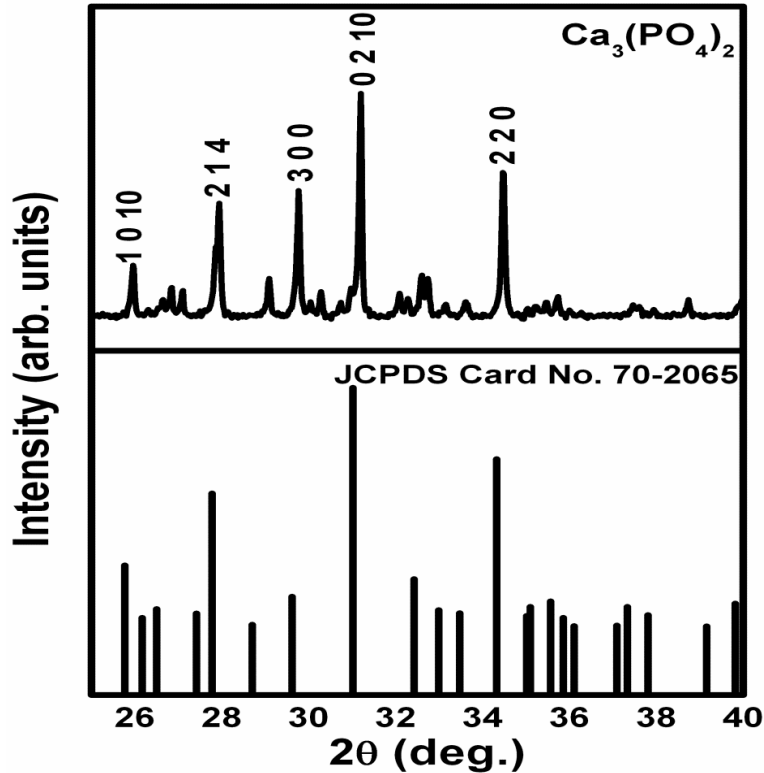


Figure 9.1 XRD patterns of $\text{Ca}_3(\text{PO}_4)_2$ annealed at 1000°C in air.

Figure 9.2 (a-b) show High Resolution SEM images of $\text{Ca}_3(\text{PO}_4)_2:\text{Gd}^{3+},\text{Pr}^{3+}$ powder phosphor. The powder consisted of small and big particles. The small particles are presented in white and big particles are much darker, and agglomerated together with faceted particles.

Figure 9.2 (c-d) show SEM images of the $\text{Ca}_3(\text{PO}_4)_2:\text{Gd}^{3+},\text{Pr}^{3+}$ captured using extremely low landing energies achieved by a deceleration of highly unstigmated electron leaving the objective lens called gentle beam [6]. This procedure is also called specimen bias or retarding field. Landing energy is defined as the difference between the accelerating (column) voltage and stage-bias voltage. The gentle beam imaging is suitable for non-conductive specimens or insulators which experience a lot of surface charging. By using extremely low landing energies charging can be eliminated thereby enhancing the image quality without having to coat the surface. Therefore figure 9.2 (c) – (d) confirm that the powder was made of faceted hexagonal particles which were highly agglomerated together.

Figure 9.2 (e)-(f) show the EDS spectra of $\text{Ca}_3(\text{PO}_4)_2:\text{Gd}^{3+},\text{Pr}^{3+}$ powder phosphor confirming the presence of all the elements in the material. The spectrum in Figure 9.2 (e) and (f) show the

elements detected at position S1 and S2, and S2 and S3, respectively, as shown by the SEM images on the insets. The bar graphs on the top right corner compare the amount of elements by weight at different positions marked by S1, S2 and S3. It can be concluded that the white particles were dominated by Pr^{3+} ions while the dark particles were dominated by Ca^{2+} .

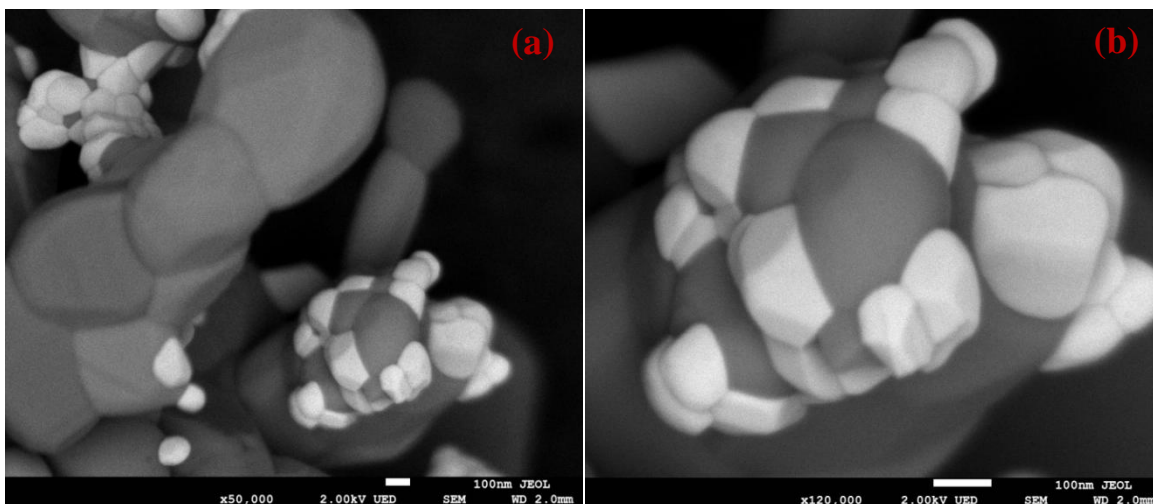


Figure 9.2 (a-b) High Resolution SEM images of $\text{Ca}_3(\text{PO}_4)_2:\text{Gd}^{3+}, \text{Pr}^{3+}$ powder phosphor.

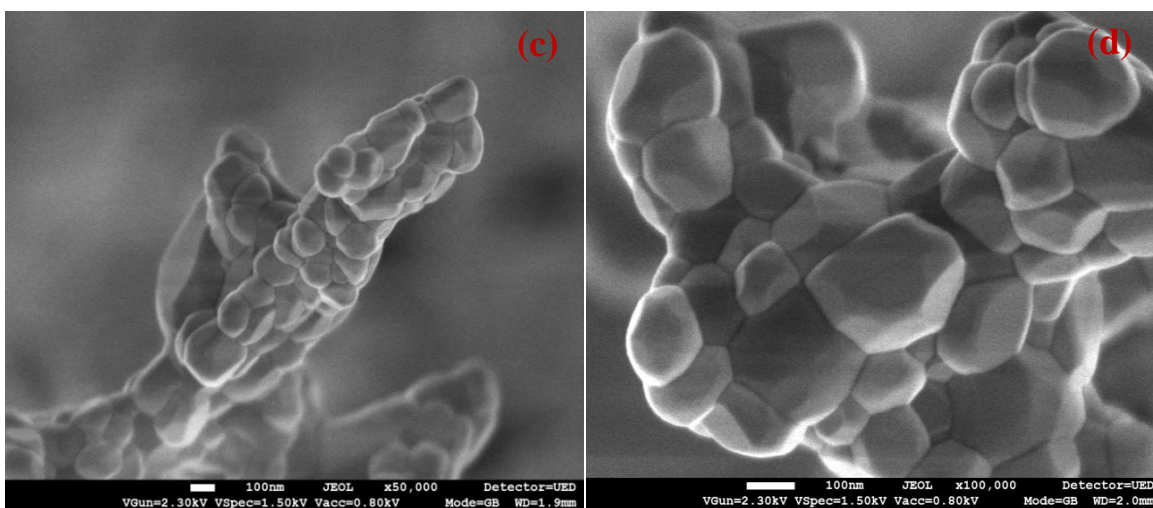


Figure 9.2 (c-d) shows the morphology of $\text{Ca}_3(\text{PO}_4)_2:\text{Gd}^{3+}, \text{Pr}^{3+}$ powder measured by using objective lens called gentle beam.

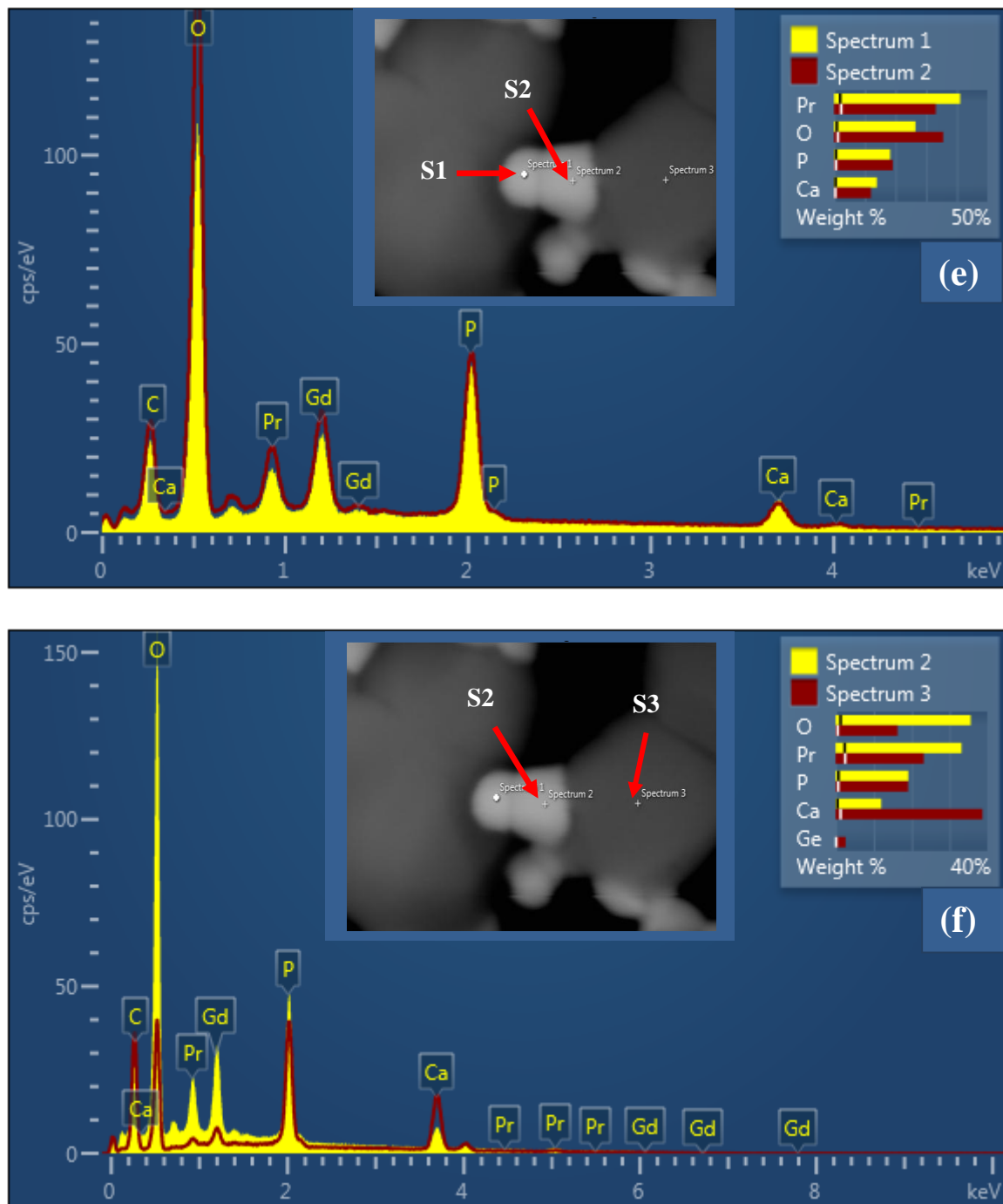


Figure 9.2 (e-f) EDS spectra of $\text{Ca}_3(\text{PO}_4)_2:\text{Gd}^{3+},\text{Pr}^{3+}$ powder phosphors.

Figure 9.3 shows the PL (i) excitation and (ii) emission spectra of $\text{Ca}_3(\text{PO}_4)_2:\text{Gd}^{3+}$ prepared at different concentrations of Gd^{3+} . The relative excitation peaks were observed at 245 and 274 nm and they are respectively assigned to the $^8\text{S}_{7/2} \rightarrow ^6\text{D}_j$ and $^8\text{S}_{7/2} \rightarrow ^6\text{I}_j$ intra $4f^7$ transitions of Gd^{3+} [7, 8]. The excitation peaks are assigned to $4f \rightarrow 4f$ intraconfigurational forbidden transitions of Gd^{3+}

[9]. The narrow line emission peak of Gd^{3+} at 313 nm assigned to the ${}^6P_{7/2} \rightarrow {}^8S_{7/2}$ transition of Gd^{3+} was observed when the sample was excited at a wavelength of 274 nm. The inset shows that the intensity of the 313 nm emission increased with Gd^{3+} concentration from 1 – 5 mol% and was reduced when the concentration was increased to 10 mol %. The decrease in the PL intensity at higher concentration of Gd^{3+} can be attributed to concentration quenching effects.

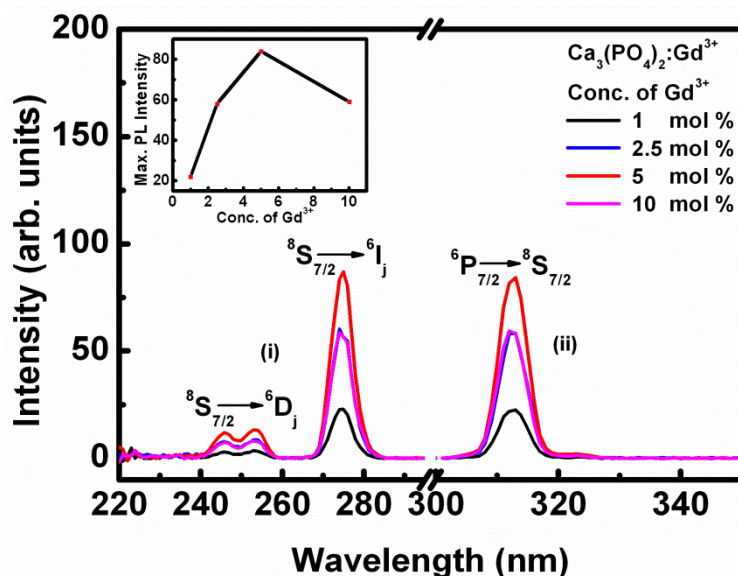


Figure 9.3 PL spectra (i) excitation ($\lambda_{\text{exc}} = 313$ nm) and (ii) emission ($\lambda_{\text{em}} = 274$ nm) of $Ca_3(PO_4)_2:Gd^{3+}$ powder phosphor.

Figure 9.4 (a) shows the PL (i) excitation and (ii) emission spectra of $Ca_5(PO_4)_3OH:Gd^{3+},Pr^{3+}$ powder phosphor. The PL excitation spectra consist of a narrow peak at 274 nm and broadband at 222 nm assigned to ${}^8S_{7/2} \rightarrow {}^6I_j$ transitions of Gd^{3+} and $4f \rightarrow 4f5d$ transitions of Pr^{3+} respectively. PL emission band attributed to Pr^{3+} ions become weaker when co-doped with Gd^{3+} [10, 11]. The excitation energy is preferentially transferred from 5d levels of Pr^{3+} to Gd^{3+} ions. The peak intensity of the Pr^{3+} excitation and UV emission at 313 nm improved considerably when incorporating Pr^{3+} . The maximum excitation was observed when the molar ratio of Gd^{3+} to Pr^{3+} was 5:5 and this was reduced at the ratio of 5:10. Figure 9.4 (a) (ii) shows the PL emission spectra of $Ca_5(PO_4)_3OH:Gd^{3+},Pr^{3+}$ when excited with the wavelength of 222 nm. The spectra show only the emission peak at 313 nm corresponding to the ${}^8S_{7/2} \rightarrow {}^6G_j$ transitions of Gd^{3+} . This peak is 5× more intense than the same peak observed from the Gd^{3+} single doped $Ca_3(PO_4)_2$ as shown in figure 9.4 (b). This result shows that Pr^{3+} is a good sensitizer of the 313 nm UVB

emission of Gd^{3+} . In other words, Pr^{3+} absorbs excitation energy and transfers it non-radiatively to Gd^{3+} .

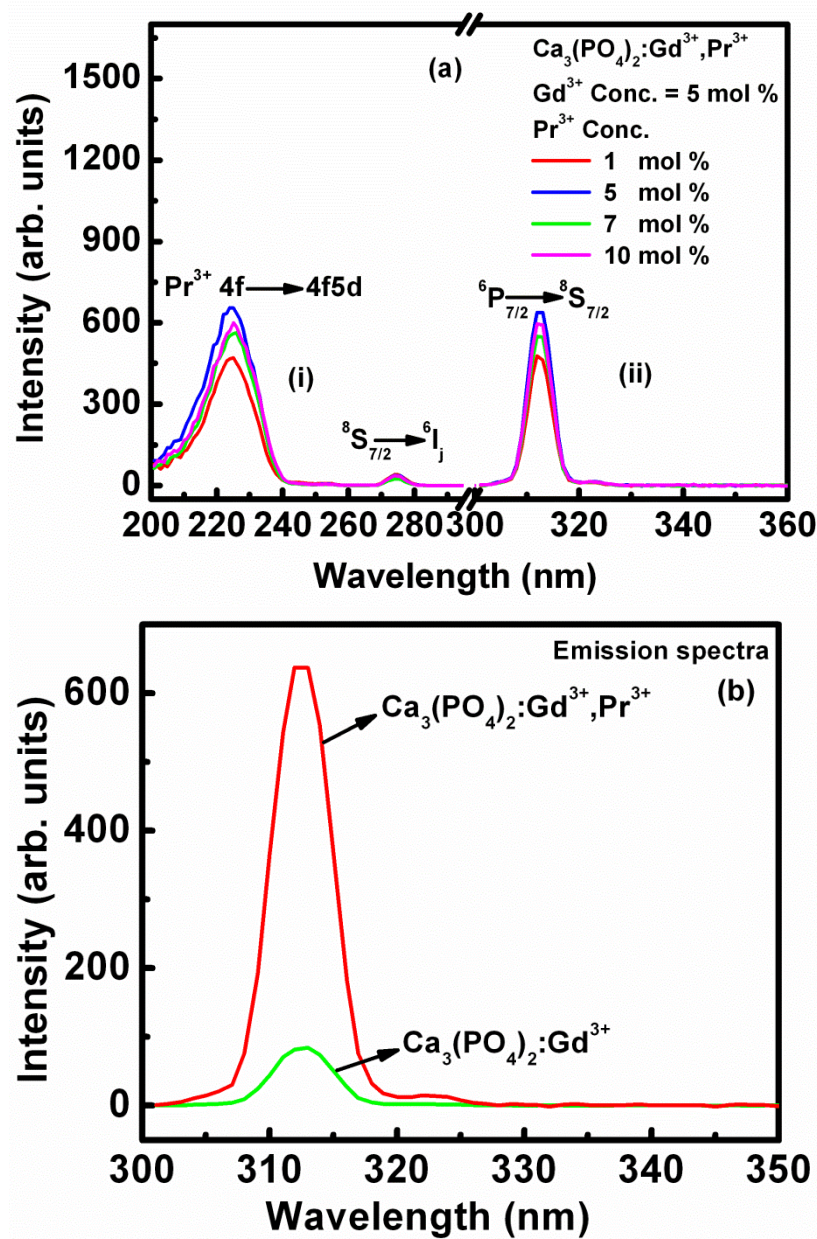


Figure 9.4 PL (a) (i) excitation and (ii) emission spectra of $Ca_3(PO_4)_2:Gd^{3+},Pr^{3+}$ powder phosphor (b) Comparison between emission intensity of $Ca_3(PO_4)_2:Gd^{3+}$ and $Ca_3(PO_4)_2:Gd^{3+},Pr^{3+}$ system.

9.4 Conclusion

$\text{Ca}_3(\text{PO}_4)_2:\text{Gd}^{3+},\text{Pr}^{3+}$ phosphor powders were successfully synthesized by microwave irradiation assisted method. The average crystallite size calculated using the Scherrer equation at different urea masses was in the range of ~ 76 nm. The surface morphologies of the powders were studied by JEOL SEM. The nanocrystals reveal formation and agglomeration of spherical-like-faceted particles in nanometric scale and presence of elements were detected by EDS. Luminescent properties of $\text{Ca}_3(\text{PO}_4)_2:\text{Gd}^{3+},\text{Pr}^{3+}$ under UV excitation have been investigated. $\text{Ca}_3(\text{PO}_4)_2:\text{Gd}^{3+},\text{Pr}^{3+}$ emits at 313 nm and the intensity is enhanced than in the $\text{Ca}_3(\text{PO}_4)_2:\text{Gd}^{3+}$ system. The UV emission makes $\text{Ca}_3(\text{PO}_4)_2:\text{Gd}^{3+},\text{Pr}^{3+}$ phosphor a good candidate for applications in phototherapy lamps.

References

- [1] M.A. Surati, S. Jauhari, K.R. Desai, *Arch. Appl. Sci. Res.*, 2012, **4**, 645-661
- [2] R. M. Palou, *J. Mex. Chem. Soc.*, 2007, **51**, 252-264
- [3] P. Lidstrom, J. Tierney, B. Wathey, J. Westman, *Tetrahedron*, 2001, **57**, 9225-9283
- [4] T. Liang, J. Qian, Y. Yuan, C. Liu, *J. Mater. Sci.*, 2013, **48**, 5334-5341
- [5] S. Jalota, C. Tas, S.B. Bhaduri, *J. Mater. Res.*, 2004, **19**, 1876-1881
- [6] S.M. Stevens, K. Jansson, C. Xiao, S. Asahina, M. Klingstedt, D. Gruner, Y. Sakamoto, K. Miyasaka, P. Cubillas, R. Brent, L. Han, S. Che, R. Ryoo, D. Zhao, M. Anderson, F. Schuth, O. Terasaki, An Appraisal of High Resolution Scanning Electron Microscopy Applied To Porous Materials, **44**, 17-22
- [7] F. Du, R. Zhu, Y. Huang, Y. Tao, H. Jin Seo, *Dalton Trans.*, 2011, **40**, 11433-11440
- [8] J. Zhong, H. Liang, Q. Su, J. Zhou, Y. Huang, Z. Gao, Y. Tao, J. Wang, *Appl. Phys. B*, 2010, **98**, 139-147
- [9] A. Richter, E. Heumann, G. Huber, *Opt. express*, 2007, **15**, 5172-5178
- [10] Z. Tian, H. Liang, B. Han, Q. Su, Y. Tao, G. Zhang, Y. Fu, *J. Phys. Chem. C*, 2008, **112**, 12524-12529
- [11] T.J. Lee, L.Y. Luo, B.M. Cheng, W.G. Diao, T.M. Chen, *Appl. Phys. Lett.*, 2008, **92**, 08110600-3

Chapter 10: Summary and Conclusion

This chapter presents the summary and conclusion, and possible future work that can be done to improve the properties of phosphate phosphors.

$\text{Ca}_5(\text{PO}_4)_3\text{OH}:\text{Gd}^{3+},\text{Pr}^{3+}$ phosphor powders were prepared by co-precipitation method and annealed at different temperatures from 600 – 1000 °C in air for 2 hours. The hexagonal phase was observed. The crystallite size estimated using Scherrer equation was found to be in the range of ~22 – 65 nm from 600 – 1000 °C. The hexagonal phase of $\text{Ca}_5(\text{PO}_4)_3\text{OH}$ powder shows the existence of two sites of Ca^{2+} ion in the host. The P^{5+} ion is surrounded by O^{2-} ions in the tetrahedral arrangements. Each tetrahedron contains oxygen atoms designated as O1, O2, and O3 and hydrogen atom bonding to one oxygen atom. SEM images revealed agglomeration of no regular shape of $\text{Ca}_5(\text{PO}_4)_3\text{OH}$ powder with HRTEM showing faceted edges, forming a hexagonal shape. The lattice fringes were used to calculate the d-spacing. The d-spacing was found to be 5.12 Å corresponding to the (101) plane. Peak positions and surface images of each ion present in the phosphor powder was observed by TOF-SIMS measurements. $\text{Ca}_5(\text{PO}_4)_3\text{OH}$ and $\text{Ca}_5(\text{PO}_4)_3\text{OH}:\text{Gd}^{3+}$ powders exhibited two absorption peaks at 207 and 300 nm assigned to interband transition and defects within the material. $\text{Ca}_5(\text{PO}_4)_3\text{OH}:\text{Pr}^{3+}$ and $\text{Ca}_5(\text{PO}_4)_3\text{OH}:\text{Gd}^{3+},\text{Pr}^{3+}$ further exhibit peaks at a range of 446 – 593 nm assigned to $^3\text{H}_4 \rightarrow ^3\text{P}_{(j=0, 1, 2)}$ and $^3\text{H}_4 \rightarrow ^1\text{D}_2$ transitions of Pr^{3+} ion. The bandgap was estimated using Tauc's relation and was found to be 5.00 ± 0.05 eV. Gd^{3+} singly doped $\text{Ca}_5(\text{PO}_4)_3\text{OH}$ exhibited narrowband emission peak at 313 nm assigned to $^6\text{P}_{7/2} \rightarrow ^8\text{S}_{7/2}$ transition of Gd^{3+} ion. Pr^{3+} incorporation in the $\text{Ca}_5(\text{PO}_4)_3\text{OH}:\text{Gd}^{3+}$ system resulted, through energy transfer, in enhanced PL intensity of the Gd^{3+} , making it a superior phosphor for application in phototherapy lamps.

TL measurements showed a single glow curve which was attributed to one type of a trap in the material, and the trap may be due to the defects such as vacancies or impurities. The trap can be forbidden by increasing the annealing time or temperature. The glow curve show an increase in intensity as dose increases and the shifting (to the right) of the peaks may be due to change in particle size. From the glow curve data, the activation energies were evaluated using different methods such as initial rise, peak shape, heating rate and $T_m - T_{stop}$. The activation energies were almost comparable on all methods applied.

$\text{Ca}_3(\text{PO}_4)_2:\text{Gd}^{3+},\text{Pr}^{3+}$ phosphor powders with different concentrations of Gd^{3+} and Pr^{3+} were successfully prepared by an urea combustion process using metal nitrates as precursors and urea as fuel, and were annealed at 1000 °C in air for 2 hours. The rhombohedral phase of $\text{Ca}_3(\text{PO}_4)_2$ was confirmed by XRD. The crystallite size for different masses of urea used was in the range of ~60 – 120 nm. $\text{Ca}_3(\text{PO}_4)_2$, $\text{Ca}_3(\text{PO}_4)_2:\text{Gd}^{3+}$ and $\text{Ca}_3(\text{PO}_4)_2:\text{Gd}^{3+},\text{Pr}^{3+}$ phosphor powders show different morphologies due to influence of doping in each system. The morphology changed from nanospheres to nanorods upon Gd^{3+} ion and Pr^{3+} ion doping. $\text{Ca}_3(\text{PO}_4)_2$ and $\text{Ca}_3(\text{PO}_4)_2:\text{Gd}^{3+}$ powder exhibited absorption peaks at 230 and 285 nm attributed to band-to-band transition and defects within the material. The PL spectra show that the emission increases considerably when incorporating Pr^{3+} ion. Possible energy transfer mechanism was discussed.

$\text{Ca}_5(\text{PO}_4)_3\text{OH}:\text{Gd}^{3+},\text{Pr}^{3+}$ phosphor powders were prepared by citrate-gel combustion method and annealed at 850 °C for 2 hours in air. The hexagonal structure was observed and the estimated crystal size of $\text{Ca}_5(\text{PO}_4)_3(\text{OH}):\text{Gd}^{3+},\text{Pr}^{3+}$ was found to be ~ 45 nm. The powder consisted of small and bigger particles with spherical but faceted shapes. The EDS confirmed the presence of all elements in the material. The two PL excitation peaks were observed at 245 and 275 nm assigned to $^8\text{S}_{7/2} \rightarrow ^6\text{D}_j$ and $^8\text{S}_{7/2} \rightarrow ^6\text{I}_j$ transitions of Gd^{3+} ion respectively. $\text{Ca}_5(\text{PO}_4)_3\text{OH}:\text{Gd}^{3+}$ exhibited a narrow emission peak at 313 nm assigned to $^6\text{P}_{7/2} \rightarrow ^8\text{S}_{7/2}$ transitions of Gd^{3+} ion. The inset shows that luminescence intensity increases with an increase in concentration of Gd^{3+} . $\text{Ca}_5(\text{PO}_4)_3\text{OH}:\text{Gd}^{3+},\text{Pr}^{3+}$ system shows that upon co-doping with Pr^{3+} the broad excitation peak at 222 nm is observed assigned to $4f \rightarrow 4f5d$ transition of Pr^{3+} ion. The luminescence intensity increased considerably, suggesting an energy transfer from Pr^{3+} to Gd^{3+} ion.

$\text{Ca}_5(\text{PO}_4)_3\text{OH}:\text{Gd}^{3+},\text{Pr}^{3+}$ phosphor powders were prepared by microwave assisted method and annealed at 850 °C in air. The XRD patterns were consisted with the standard hexagonal phase of $\text{Ca}_5(\text{PO}_4)_3\text{OH}$ with the estimated average crystallite size of ~ 76 nm. The powder consisted of small and bigger particles. The smaller particles were spherical but faceted and inhomogeneously distributed on the surface of dark bigger particles which were agglomerated together and did not have any regular shapes. Gd^{3+} singly doped $\text{Ca}_5(\text{PO}_4)_3\text{OH}$ exhibited narrowband emission peak at 313 nm assigned to ${}^6\text{P}_{7/2}\rightarrow{}^8\text{S}_{7/2}$ transition of Gd^{3+} . The absorbed energy by Pr^{3+} at 222 nm was transferred to Gd^{3+} which resulted in an enhanced Gd^{3+} emission at 313 nm.

In this study the luminescent and structural properties of calcium phosphate phosphor co-doped with gadolinium and praseodymium were successfully prepared by co-precipitation, urea combustion, citrate-gel combustion and microwave assisted methods. The co-precipitation and microwave assisted methods requires longer time for preparation. The combustion method is more efficient compared to other methods because phosphors were obtained in a very short period of time at low temperatures.

Future Work

Further research that will be done is to test the phosphors developed in this study in phototherapy lamps. In addition this study can be extended to the development of biocompatible UV emitting nanocrystalline phosphors that can be used in photodynamic therapy or PDT. Photodynamic therapy is a form of phototherapy in which cancerous cells and tissues are destroyed by combination of light from nanophosphors with appropriate wavelengths. More focus will be on the development of phosphate or fluorides host doped with rare earth ions nanophosphors that can be used as a source of UV radiation for PDT. The overriding objective will be to improve the luminescent intensity and chemical stability of the phosphor in order to prolong the life span and the general performance of PDT devices.